

LASER BRAZING OF REACTION-BONDED SILICON CARBIDE WITH A  
SILICON-ALUMINUM-TITANIUM FILLER ALLOY

by

Brian Rodgers

A thesis submitted to the Faculty and the Board of Trustees of the Colorado School of Mines in partial fulfillment of the requirements for the degree of Master of Science (Metallurgical and Materials Engineering).

Golden, Colorado

Date \_\_\_\_\_

Signed: \_\_\_\_\_

Brian Rodgers

Signed: \_\_\_\_\_

Dr. Stephen Liu

Thesis Advisor

Signed: \_\_\_\_\_

Dr. Juan Carlos Madeni

Thesis Advisor

Golden, Colorado

Date \_\_\_\_\_

Signed: \_\_\_\_\_

Dr. Angus Rockett

Professor and Head

George S. Ansell Department of Metallurgical and Materials Engineering

## ABSTRACT

This work focuses on the feasibility of joining reaction-bonded silicon carbide (RB-SiC) with a laser heat source. A ternary Si-Al-Ti alloy was used as filler metal. Research consisted of four phases: laser metrology, damage free preheating, wettability testing, and lap joint testing. Results indicate joining is feasible but can be further optimized.

Laser metrology consisted of measuring beam diameter by ablating holes in a polyimide film. Knowing exact beam parameters was required to determine the threshold for heating the substrate without damaging it. Cracking is not the only damage mechanism; surface porosity is created due to thermal exposure. Rastering the beam allows for better control of temperatures and mitigates surface damage. Thus, most testing in this work was done with a rastered beam.

Heating for the sessile drop wettability testing involved a preheat raster of the RB-SiC coupon, pause time for a controlled and uniform preheat temperature in the RB-SiC coupon, and a localized secondary raster around the filler metal location. The atmosphere was controlled to a maximum of 15 ppm oxygen, balanced argon. All contact angles were greater than or equal to ninety degrees. Oxidation of the liquid filler metal surface preventing spreading is the cause of high contact angles. Cross-sectioning the brazed joints revealed good wetting between the filler metal and substrate. Significant diffusion of alloying elements also occurred during testing.

Lap joint brazing followed the same preheat, pause, localized heating pattern as in wettability testing with a limit on oxygen concentration. Joint strength was calculated by shearing the joints to failure and dividing the load at failure by the nominal joint area. Lap joints failed either inside the joint, through the joint and substrate, or only within the substrate. Strength was greatest in substrate failures and least for in joint failures, but never exceeded 20 MPa. Low strength is attributed to incomplete gap filling and surface damage. Since the filler metal was delivered as a foil preform covering the entire joint area, incomplete gap filling was a result of the loss of material. Material loss from the joint occurred through a combination of elemental diffusion and overflowing the gap and solidifying on the outside surfaces. Oxidation of the filler metal prevented overflowing most of the time, but the oxide layer also locally ruptured. Joint strength was mostly affected by factors influencing how much filler metal leaves the gap.

## TABLE OF CONTENTS

|  |     |
|--|-----|
| ABSTRACT.....                                      | iii |
| LIST OF FIGURES.....                               | vii |
| LIST OF TABLES.....                                | xi  |
| ACKNOWLEDGEMENTS.....                              | xii |
| CHAPTER 1 INTRODUCTION.....                        | 1   |
| CHAPTER 2 BACKGROUND.....                          | 4   |
| 2.1 Reaction-bonded Silicon Carbide.....           | 4   |
| 2.2 Joining Techniques for Silicon Carbide.....    | 6   |
| 2.1.1 Conventional Methods.....                    | 6   |
| 2.2.2 Brazing.....                                 | 7   |
| 2.2.3 Oxidation Effects.....                       | 18  |
| 2.2.4 Other Non-fusion Joining Techniques.....     | 21  |
| 2.3 Laser Processing Experimental Techniques.....  | 23  |
| CHAPTER 3 EXPERIMENTAL PROCEDURES.....             | 26  |
| 3.1 Beam Diameter Measurement.....                 | 27  |
| 3.2 Substrate Damage Threshold and Preheating..... | 28  |
| 3.3 Filler Metal Synthesis.....                    | 30  |
| 3.4 Wettability Testing.....                       | 32  |
| 3.5 Lap Joint Testing.....                         | 35  |
| CHAPTER 4 RESULTS & DISCUSSION.....                | 42  |

|  |   |     |
|--|---|-----|
| 4.1                                    | Beam Diameter Calibration.....                  | 42  |
| 4.2                                    | Preheating.....                                 | 44  |
| 4.2.1                                  | Heat Transfer in Wettability Testing.....       | 47  |
| 4.2.2                                  | Heat Transfer in Lap Joints.....                | 50  |
| 4.3                                    | Laser and Thermal Effects on the Substrate..... | 52  |
| 4.3.1                                  | Surface Texturing.....                          | 54  |
| 4.3.2                                  | Surface Damage Mechanisms.....                  | 55  |
| 4.4                                    | Wettability Testing.....                        | 61  |
| 4.4.1                                  | Melting and Solidification Behavior.....        | 62  |
| 4.4.2                                  | Oxidation in Wettability Testing.....           | 69  |
| 4.4.3                                  | Contact Angles.....                             | 72  |
| 4.4.4                                  | Sessile Drop Microstructure.....                | 74  |
| 4.4.5                                  | Wettability Testing Summary.....                | 82  |
| 4.5                                    | Lap Joint Testing.....                          | 83  |
| 4.5.1                                  | Lap Joint Microstructure.....                   | 84  |
| 4.5.2                                  | The Diffusion Affected Zone (DAZ).....          | 88  |
| 4.5.3                                  | Overflows.....                                  | 92  |
| 4.5.4                                  | Oxidation in Lap Joints.....                    | 98  |
| 4.5.5                                  | Fractography.....                               | 100 |
| 4.5.6                                  | Shear Strength.....                             | 104 |
| 4.6                                    | Summary of Results.....                         | 108 |
| CHAPTER 5 SUMMARY AND CONCLUSIONS..... |   | 109 |
| CHAPTER 6 FUTURE WORK.....             |   | 111 |

REFERENCES CITED..... 114

## LIST OF FIGURES

|            |   |    |
|------------|---|----|
| Figure 2.1 | Logarithmic radar chart comparing physical properties of RB-SiC to other synthesis methods [1].....5  | 5  |
| Figure 2.2 | Behavior of wetting and non-wetting in plates immersed in a liquid, taken from [18].....8   | 8  |
| Figure 2.3 | Wetting and non-wetting molten droplets on a substrate.....10   | 10 |
| Figure 2.4 | Misfit between TiC and diamond on different planes, with ellipsoids and small circles representing free C bonds, light circles as C-terminated TiC surface, and $\eta$ means misfit [30].....14 | 14 |
| Figure 2.5 | Electron backscattered electron image and EPMA scans of 316 stainless steel joined to SiC with Ag-Cu-Ti filler, taken from [31].....15  | 15 |
| Figure 2.6 | Ellingham type diagram for the formation of carbides and silicides with SiC at 0 K as the reference energy, as taken from [35] .....18  | 18 |
| Figure 2.7 | Intensity profiles for transverse electromagnetic modes in laser beams [51] .....24   | 24 |
| Figure 3.1 | Laser chamber used for experiments, including sealed chamber and O <sub>2</sub> sensor for atmospheric control and non-contact pyrometer for temperature measurement .....26                    | 26 |
| Figure 3.2 | Kapton™ films after laser radiation to create holes and beam diameter dependency on focal distance .....28  | 28 |
| Figure 3.3 | To-scale image of raster pattern used for preheating calibration, with the white box showing the raster pattern and gray box showing the RB-SiC surface .....30                                 | 30 |
| Figure 3.4 | Arc melter used to synthesize filler metal .....31  | 31 |
| Figure 3.5 | Extra growths created during later portion of solidification by Si content, grayscale .....32   | 32 |
| Figure 3.6 | To-scale diagram showing beam diameter, size of ideal filler metal cuboid, and raster pattern for secondary rastering in wettability testing .....34  | 34 |
| Figure 3.7 | Silica shells used to hold RB-SiC coupons and filler metal during joining .....36   | 36 |
| Figure 3.8 | Top down view of the thermal calibration test geometry for lap joints, with dark gray as the overlapped region, red the beam path, and white the pyrometer measurement point .....37            | 37 |
| Figure 3.9 | To-scale image of the path taken by the secondary raster in orange .....39  | 39 |

|             |   |    |
|-------------|---|----|
| Figure 3.10 | Mechanical testing fixture with example samples .....   | 40 |
| Figure 4.1  | Hole diameter in Kapton™ film versus focal distance .....   | 43 |
| Figure 4.2  | Hole diameter used to measure beam width as a function of distance from the focal plane, with the orange line showing the linear regression extrapolated values.....                    | 44 |
| Figure 4.3  | Comparison between data collected with 100 to 700 and 750 to 2500 °C pyrometers with beam and pyrometer measurement point overlapping .....   | 45 |
| Figure 4.4  | Changes in absorptivity with temperature at 1064 nm for silicon carbide [3] .....   | 47 |
| Figure 4.5  | Temperature recorded by pyrometer for different times after beam shut-off when rastering over single coupon atop firebrick, only one reading per point due to consistent behavior ..... | 48 |
| Figure 4.6  | Cooling curves after the laser beam is shut off for different powers.....   | 49 |
| Figure 4.7  | Plot used to find Equation 4.3 .....  | 50 |
| Figure 4.8  | Comparison of thermal behavior between different silica fixture slots to ensure consistent behavior.....  | 51 |
| Figure 4.9  | The results of a focused beam impinging on a RB-SiC coupon.....   | 52 |
| Figure 4.10 | Results of laser ablation on RB-SiC surface in grid with varying power; distortion in grid (700 to 1100 W) from CNC issues.....   | 54 |
| Figure 4.11 | Results of oxidation experiment with transparent overlay illustrating beam position and diameter .....  | 56 |
| Figure 4.12 | RB-SiC sample exposed to rastered beam instead of static beam .....   | 57 |
| Figure 4.13 | EDS scans of bead developed during wettability testing .....  | 58 |
| Figure 4.14 | Different levels of Si loss and surface damage seen in RB-SiC with zone labels .....  | 59 |
| Figure 4.15 | Light optical stereoscope image of wettability sample given only preheat raster.....  | 62 |
| Figure 4.16 | Simulation of melting in filler metal with phase descriptions added.....  | 63 |
| Figure 4.17 | Low temperature pyrometer data from wettability tests with only a secondary raster.....   | 64 |
| Figure 4.18 | Surface interaction zone on wettability sample given only 30 s secondary raster.....  | 65 |

|             |  |    |
|-------------|--|----|
| Figure 4.19 | Sample given 455 °C preheat and three second secondary raster, the lowest parameters providing adhesion .....  | 67 |
| Figure 4.20 | Scheil solidification simulation of the filler metal with phase labels .....   | 68 |
| Figure 4.21 | An Ellingham diagram with the elements in the filler metal highlighted [61].....   | 70 |
| Figure 4.22 | EDS maps of oxidized filler metal surface after wettability test .....   | 71 |
| Figure 4.23 | Contact angles as a function of preheat temperature and secondary raster time ...  | 73 |
| Figure 4.24 | Electron backscattered electron image of sample given 455 °C preheat and three seconds of secondary raster time, with emphasis on the filler-RB-SiC interface .....      | 75 |
| Figure 4.25 | Electron backscattered electron image of sample given 650 °C preheat and 30 seconds of secondary raster time, with emphasis on the filler-RB-SiC interface .             | 76 |
| Figure 4.26 | Inconsistent wetting behavior of sample given 1050 °C preheat and 300 second secondary raster, image in grayscale .....  | 77 |
| Figure 4.27 | Filler metal diffusion through the thickness of the sample and free Si loss during wettability testing with a 1050 °C preheat and 300 second secondary raster.....       | 78 |
| Figure 4.28 | Top down view of sample given 1050 °C preheat and 300 s secondary raster .....   | 79 |
| Figure 4.29 | Higher magnification image of protrusion developed during solidification .....   | 80 |
| Figure 4.30 | Backscattered electron image of sample given 1050 °C preheat and 300 seconds secondary raster .....  | 81 |
| Figure 4.31 | Labelled EDS maps of foil before brazing with backscattered electron image in bottom right corner.....   | 85 |
| Figure 4.32 | Comparison of overlaid EDS maps with electron backscattered electron image, with Si yellow, Al blue, and Ti magenta in the EDS maps.....                                 | 86 |
| Figure 4.33 | Filler metal foil analyzed by SEM and EDS after brazing .....  | 87 |
| Figure 4.34 | Scheil solidification simulation for Ti and Al lean alloy after diffusional losses .   | 88 |
| Figure 4.35 | Backscattered map (middle) with Al (blue) and Ti (magenta) EDS maps of diffusion .....   | 89 |
| Figure 4.36 | Light optical stereoscope image of through diffusion of filler metal on surface and backscattered electron image of transverse section through the external feature..... | 91 |

|             |  |     |
|-------------|--|-----|
| Figure 4.37 | Overflow feature which unintentionally brazed the silica fixture, 400 W, 120 s secondary raster, and 200 to 250 $\mu\text{m}$ foil ..... | 92  |
| Figure 4.38 | Overflow behavior in sample with filler introduced as cuboid instead of foil .....   | 94  |
| Figure 4.39 | Electron backscattered electron image of overflow with EDS map showing conjoining of overflows only where iron is present.....           | 95  |
| Figure 4.40 | Thermal response of sample given 400 W during five second pause between rasters .....  | 96  |
| Figure 4.41 | Filler metal that expanded during solidification and occupied the area where a fillet would be without forming a true fillet .....       | 97  |
| Figure 4.42 | Fillet formation prevented by oxidation.....   | 98  |
| Figure 4.43 | Fillet developed in sample made exclusively with Ar-H gas .....  | 99  |
| Figure 4.44 | Fracture surface with filler metal coverage gap in the middle of the foil preform.....   | 100 |
| Figure 4.45 | EDS maps and backscattered electron image of holes left behind by filler metal diffusion .....   | 101 |
| Figure 4.46 | All three states of oxidation found within fractures surface, labelled .....   | 102 |
| Figure 4.47 | Cantilever curl in fractured samples .....   | 104 |
| Figure 4.48 | Strength as a function of foil preform thickness.....  | 105 |
| Figure 4.49 | Strength as a function of beam power.....  | 106 |
| Figure 4.50 | Strength as a function of secondary raster time .....  | 107 |

## LIST OF TABLES

|           |  |       |
|-----------|--|-------|
| Table 2.1 | Contact angles of selected filler metals in an argon atmosphere heated by induction.....         | 17    |
| Table 3.1 | Parameters in Wettability Testing.....   | 34    |
| Table 3.2 | Lap Joint Testing Parameters.....  | 38-39 |
| Table 4.1 | Intensity and exposure time results used to evaluate the intensity needed to avoid fracture..... | 53    |
| Table 4.2 | Contact Angle Responses for Samples with Unique Processing Conditions.....                       | 73    |
| Table 4.3 | Shear strength and standard deviation for all the failure modes.....                             | 103   |

## ACKNOWLEDGEMENTS

The author wishes to thank the Rolls-Royce Corporation Indianapolis site for funding this research. Special thanks are extended to Mr. Scott Nelson and Dr. Ray Xu for their assistance and advice throughout the research. Their thoughts and experience were crucial in figuring out certain issues encountered.

The author also wishes to thank those that personally supported and encouraged them throughout this project, most notably Savannah.

## Chapter 1

### CHAPTER 1: INTRODUCTION

Silicon carbide is widely known as an abrasive but has applications in several other areas including: armor, spaceborne telescope mirrors, high temperature semiconductors, nuclear reactor cores, and structural components. This work focuses on structural applications. For instance, gas power turbines require high temperature structural components, especially in and near the combustion zone. Turbines operate more efficiently at increased temperature, but metallic components are limited in their maximum operating temperatures. Ceramic materials endure these more extreme operating conditions due to their superior strength and corrosion resistance at temperatures over 1400 °C, which is enough to melt superalloys [1,2]. Silicon carbide is the ceramic of choice due to its combination of high thermal diffusivity, oxidation resistance, and mechanical properties.

Joining remains a challenge for the application of silicon carbide in assemblies - silicon carbide does not melt, rather it sublimates at a temperature slightly lower than the melting temperature of 2730 °C, making fusion processing impossible. Alternative joining methods exist and research is ongoing to determine which techniques are optimal for varied applications. Brazing is a viable non-fusion option and has been successfully implemented in other ceramic systems. Conventional filler materials tend to not wet ceramic materials, so “active” brazes containing elements which form a reaction layer with the substrate act as a replacement. Laser brazing has advantages over furnace brazing including faster processing times, greater process flexibility, and reduced energy usage. A laser heat source is particularly attractive for silicon carbide due to the high coupling efficiency in common laser wavelengths [3]. Additionally, heating only near the joint prevents thermal damage to the rest of the material, making it easier to incorporate said joints in the design.

Alternative methods for creating bulk silicon carbide pieces exist, but this study focuses on reaction-bonded silicon carbide (RB-SiC), which has the lowest service temperature of the common synthesis methods for SiC [1]. RB-SiC is made by pouring molten silicon into a porous structure of graphite and allowing the Si and C to react and form SiC. Free silicon remains after the reaction, with the amount varying based on the initial relative amounts of Si and C.

Impurities are also absorbed into the liquid Si front and concentrate towards the last free silicon to solidify, creating an impurity gradient. These impurities may exude outwards and appear on the surface when RB-SiC is subjected to temperatures above the melting point of the free Si.

This study employs an active filler metal in the Si-Al-Ti system and a 1070 nm ytterbium fiber laser from IPG as a heat source on RB-SiC coupons for both wettability testing and single lap joints.

Experimental work involved five main steps:

1. Calibrate laser system to enable controlled defocusing of the beam.
2. Determine safe parameters that do not compromise the integrity of the substrate.
3. Establish rastering methods to create desired temperatures on the substrate.
4. Evaluate wettability with sessile drop testing technique.
5. Create single lap joints and identify the conditions for optimal strength.

Data obtained from ablating holes in 50  $\mu\text{m}$  thick Kapton<sup>TM</sup> film was analyzed to determine a correlation between beam diameter and focal distance. The maximum allowable intensity of the laser that did not introduce any damage to the RB-SiC coupons was investigated by impinging the beam for increasing times in a static spot with different beam widths and power. Fracture or cracking was not observed below 260  $\text{W}/\text{mm}^2$  intensities. A non-contact pyrometer in conjunction with different time and power combinations under constant laser intensity resulted in a thermal calibration methodology to establish suitable rastering schemes. The design of sessile drop wettability experiments required knowing the exact beam parameters. In wettability tests, the filler metal was placed in the middle of the rastered region to minimize exposure to the beam in an Ar atmosphere with <15 ppm  $\text{O}_2$ . Melting of the filler metal resulted from the heating of the substrate and not directly impinging the laser beam on the filler. A silica fixture held lap joints in place with filler metal pre-placed between the overlapping RB-SiC pieces, under similar atmospheric conditions as the wettability tests. The joints were tested to failure in a custom machined fixture at a crosshead speed of 0.5 mm/min; strain rate varied based on gap size due to the nature of the shear testing geometry.

Raster patterns for wettability testing and lap joints follow a primary raster, pause time, and secondary raster pattern. Control variables for wettability and lap joint testing include beam

power and the duration of each raster. Foil preform thickness served as an added independent variable in the lap joints. Light optical microscopy and selective scanning electron microscopy examined wetting angles and microstructure before and after fracture.

Chapter 2  
CHAPTER 2: BACKGROUND

This section contains background information on the substrate material, joining and brazing processing, wetting and wettability testing, and experimental techniques followed in this work. This information will help the understanding of Chapters 3 to 6.

## 2.1 Reaction-bonded Silicon Carbide (RB-SiC)

Silicon carbide (SiC) is a technical ceramic first found in nature – specifically in a meteorite in 1905. The existence of the compound was first assumed in 1824 by Jons Jacob Berzelius, who also discovered silicon [5]. Silicon carbide was used as an abrasive, known for exhibiting a hardness close to diamond, but economically preferable due to its lower cost. Silicon carbide also has applications in semiconductors for products requiring high voltage and/or high temperature [6]. Recently, applications of silicon carbide in areas outside those two fields has increased its popularity. Silicon carbide is a critical component in armor due to its high hardness and low specific gravity [7]. Another appealing application of this material is in nuclear reactor cores because of the high thermal conductivity, operating temperature, chemical stability, and neutron transparency of SiC under heat and neutron flux [8]. Spaceborne telescope mirrors are also made of SiC because of its high hardness and low density [9]. The most important application of SiC within the context of this work is as a high temperature structural component. Silicon carbide performs well under conditions where creep is the primary failure mechanism and has an extensive steady-state creep regime covering most of the life of the material [10]. Total lifetimes are comparable to those of Ni-base superalloys even at temperatures hundreds of degrees higher. Coupled with high chemical stability and oxidation resistance at high temperature, SiC is an excellent candidate for applications in turbines and rocket engines [2].

Multiple synthesis methods for SiC exist with varying properties and application spaces [1]. The focus of this discussion will be on reaction-bonded silicon carbide (RB-SiC). Reaction-bonded silicon carbide is formed by pouring molten silicon into a porous graphite sponge which may have pre-existing SiC grains included to facilitate the process. The technique works with a variety of graphite sponge synthesis methods, with activated carbon being the least expensive. This method is less expensive than sintering-based techniques and better suited for creating

complex shapes. A continuous network of free SiC and free Si is left after the reaction goes to completion. Silicon carbide forms from the reaction between molten Si and solid C, with C dissolution by diffusion into the Si being a rate-limiting step. Silicon carbide formation begins by nucleation on the existing graphite surface and, rarely, homogeneously with C dissolved into the Si. If pre-made SiC is introduced to the system, most of the remaining SiC to be formed is nucleated off existing SiC particles. While this process is ongoing, impurities will be concentrated in the molten Si and eventually freeze in the last regions to solidify [4]. Exposing RB-SiC to enough heat to melt the free Si can cause impurities to exude to the surface along with some of the free Si. The free Si may be removed through chemical etching, extended thermal exposure in vacuum to volatilize the Si, or any means that do not attack the SiC network to expose the SiC structure near the surface.

The physical properties of RB-SiC are comparable to those produced using other synthesis techniques. Figure 2.1 presents data taken from CoorsTek on the physical properties of different synthesis methods in a logarithmic radar chart [1]. Black lines represent the minimum and maximum properties of SiC variants with data provided, and the orange line represents the properties of RB-SiC.

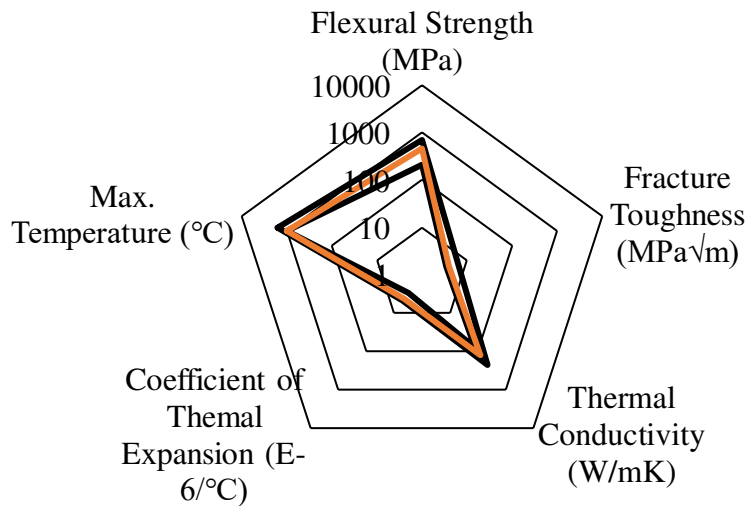


Figure 2.1 Logarithmic radar chart comparing physical properties of RB-SiC to other synthesis methods [1]

Maximum usage temperature of RB-SiC is lower due to the existence of free Si. Electrical properties were omitted due to the extreme differences making other comparisons nearly indistinguishable.

Reaction-bonded silicon carbide also has excellent creep performance at extreme temperatures. Creep studies of nickel-based superalloy examined temperatures near or below 1500 K, while similar studies for RB-SiC at temperatures up to around 1900 K showed similar lifetimes as the superalloys [11,12]. Creep in RB-SiC results in cavity formation in tension and dislocation movement in compression [13,14]. Cavities may exist beforehand or form at the Si-SiC interface. In either scenario, cavities will grow over time in creep. The number of cavities is higher near the surface and the total area fraction of cavities increases with depth before saturating 3-4 mm inwards from the surface.

Under sufficiently oxidizing conditions SiC will form SiO<sub>2</sub> on the surface. This boundary layer helps protect against further oxidation but is compromised by any sintering aids added in the case of sintered SiC [2]. However, oxidation of RB-SiC does not appear to seriously degrade flexural strength after 100 hours of exposure [16]. More oxidizing environments combined with longer exposure times may further degrade RB-SiC by increasing the thickness of the SiO<sub>2</sub> layer into the bulk. Either way, any metallic filler metal joining RB-SiC will likely experience loss of integrity from oxidation before the substrate itself sees fatal issues. In comparison, sintered SiC still has superior oxidation resistance to RB-SiC despite boundary layer weakening by sintering aids [15].

## **2.2 Joining Techniques for Silicon Carbide**

Using SiC or RB-SiC in engineering applications poses a challenge despite its excellent performance at high temperature. Manufacturing ceramics in complex shapes is a costly and difficult process. Creating individual components and assembling them is generally more desirable, but requires joining SiC to itself and other materials.

### **2.2.1 Conventional Methods**

Despite possessing enough electrical conductivity to sustain an arc, sintered SiC does not experience melting under easily achievable pressures [17]. As such, it is practically impossible to join SiC with fusion processes. Reaction-bonded silicon carbide can melt because of the free Si,

but joining using free Si liquation as a working principle could leave voids near the joint due to local Si depletion. While it is possible to simply use bolts and the like for joining, there are ways to create much stronger assemblies. Furthermore, bolting requires a through hole in the material. There are few options for creating holes in an ultrahard material: laser drilling, drilling with tooling made of an even harder material, or waterjet cutting being some examples. Holes in a RB-SiC part would also give rise to concerns about stress concentrators and flaws, which severely impact toughness in ceramics. As arc welding is not an option, more unconventional methods are required. These approaches are discussed in future sections.

### **2.2.2 Brazing**

Whenever a material cannot be joined by fusion processes, brazing is one of the first non-fusion joining processes considered. Brazing is a process where two materials, similar or not, are joined together by melting a third material between them at or above 450 °C. Fluxes may be added to enhance flow and wettability of the material, which is typically called a filler or braze material. Melting points of filler materials are kept below the melting point of the base material to limit incipient melting of the base material. Limited melting and/or dissolution into the base material is one of the advantages of brazing. Other advantages include the ability to join dissimilar materials or even dissimilar material systems, join parts with greatly differing geometry, reduced residual stress and distortion relative to arc welding, and preservation of tight tolerances. A heat-affected zone still forms in brazing but is not as extensive as in fusion processes due to the lower temperatures reached during brazing. Brazed joints are typically made with a thin layer of filler material placed between the two surfaces to be joined, also called faying surfaces. A certain amount of the molten filler is also drawn outside the joined region by capillarity to form a fillet [18]. Fillets can either act as reinforcement for the joint or initiate cracks due to brittle intermetallic formation.

In practice, braze joints are made with such narrow gaps that filler material often does not need to be preplaced between the faying surfaces. Instead, capillary flow is enough to carry the filler material throughout the gap and sometimes overflow to form the desired fillets. Wettability is critical in causing this phenomenon. If the wettability between the substrate surface and liquid braze is unfavorable, then the filler will not flow and fill the gap. Figure 2.2 from the ASM

Handbook Volume 6 [18] illustrates the two differences in capillary behavior between wetting and non-wetting liquids.

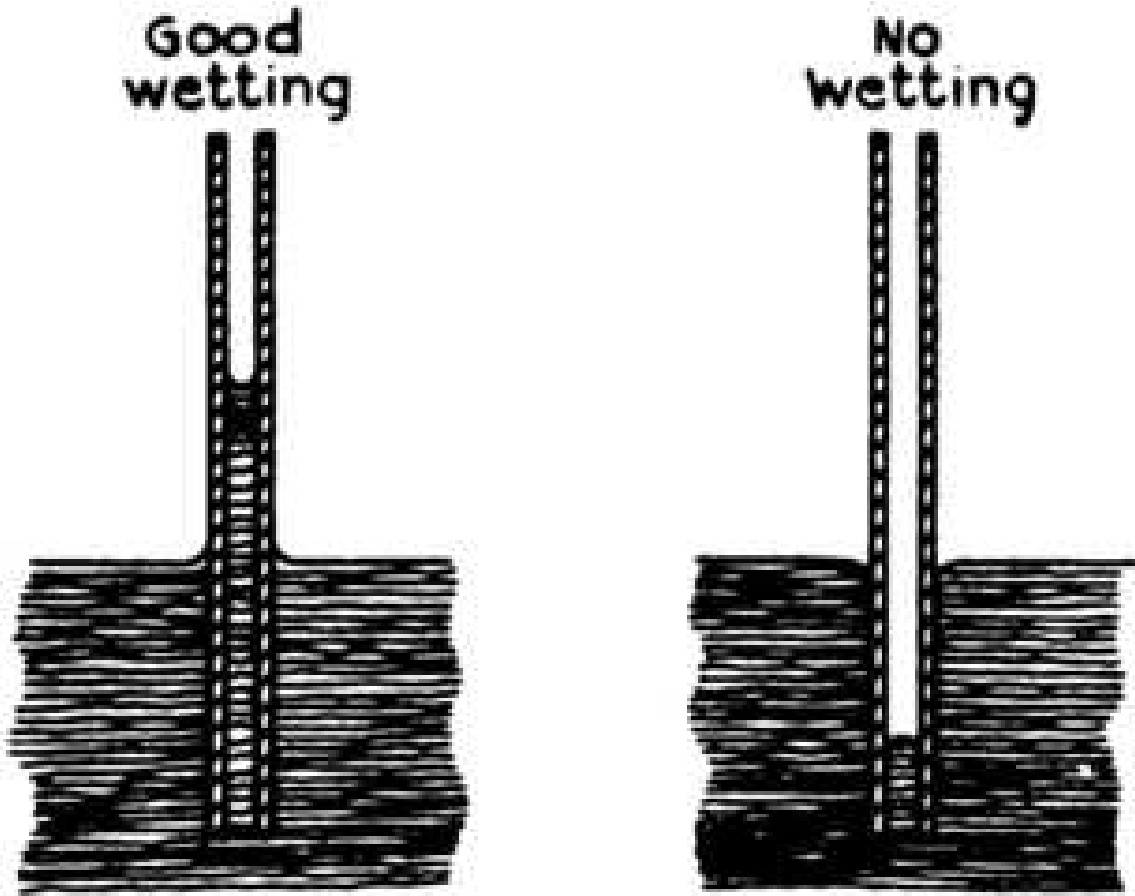


Figure 2.2 Behavior of wetting and non-wetting in plates immersed in a liquid, taken from [18]

If there is wetting between the liquid braze and the substrate then the molten filler will flow into the joint and achieve at least partial penetration; but if there is poor wetting the molten filler will not enter the joint and possibly retreat. The tendency of liquid filler to retreat is affected by the relative surface and interfacial energies. Thermodynamically, the tendency of a liquid to advance or retreat when in contact with a solid substrate is defined by Equation 2.1.

$$\frac{\Delta E_{\text{surf}}}{\Delta A} = \gamma_{\text{LG}} + \gamma_{\text{SL}} - \gamma_{\text{SG}} \quad (2.1)$$

In this equation,  $\Delta E_{\text{surf}}$  is the change in total energy of the surface,  $\Delta A$  is change in area, and  $\gamma_{\text{LG}}$ ,  $\gamma_{\text{SL}}$ , and  $\gamma_{\text{SG}}$  are the surface energies between the liquid and gas, solid and liquid, and solid and gas, respectively.

Equation 2.1 originates from the comparison of the energies of new interfaces created by the liquid advancing. If the liquid advances along the solid, the solid-liquid contact area and the liquid-atmosphere contact area increase while the solid-atmosphere area decreases. Thus, promoting wetting and flow of filler materials requires compatibility between the liquid and substrate, as captured by the term  $\gamma_{SL}$ . Materials with lower surface energies are more readily wetted and easier to braze. Essentially, whether a liquid will advance or retreat on a solid substrate depends on the comparison between the surface energy of the solid, the liquid, and the interfacial energy between solid and liquid. In the case of a vacuum or fully inert atmosphere, the equation is modified to simply use the surface energies of the liquid and solid themselves rather than their interfacial energies with the atmosphere, as shown in Equation 2.2.

$$\frac{\Delta E_{\text{surf}}}{\Delta A} = \gamma_L + \gamma_{SL} - \gamma_S \quad (2.2)$$

In this equation,  $\gamma_L$  and  $\gamma_S$  are the surface energy of the liquid and solid, respectively. There are a number of methods that can be used to experimentally determine the wettability between a given liquid and solid, such as capillary rise and sessile drop testing. If all three surface energies are known, then wetting can also be predicted. Surface energy can be roughly estimated from first principles by calculating the energy required to break each bond over an area. In solids, the heat of sublimation and atomic planar density can provide an estimate for surface energy [20]. Actual experimental measurement of the surface energy of solids is quite challenging, but experiments involving creep have generated trustworthy data [21]. The method to determine solid surface energy involves finding the load immediately before the onset of creep in a thin wire. Liquid surface energy is equal to the surface tension of the liquid in an ideal solution. Surface tension can be measured in a liquid with techniques analogous to tension testing in solids, but this is only valid for ideal solutions. Levitation and subsequent agitation of droplets to produce vibrations dampening out over time in the floating droplet can accurately determine the surface energy of liquids [22]. Both electrostatic and electromagnetic levitation methods determine surface energy, but electrostatic levitation is superior since it has a smaller effect on the vibrations of the molten droplet. The ideal scenario would be to perform these experiments in a zero gravity environment to completely eliminate the effect of the forces causing levitation.

While creep and levitation methods can experimentally determine the surface energies of solids and liquids, respectively, they do not address the interfacial energy between the two. Finding the  $\gamma_{SL}$  of a given pairing of liquid and solid requires experimentation involving contact. Fortunately, testing does not necessarily require equipment as advanced as electrostatic levitation but needs to be conducted every time for specific pairs. The easiest way to find the interfacial energy between a solid and liquid is by allowing the different media to contact each other and measuring the interior contact angle along the bounding line where solid, liquid, and atmosphere meet, known as the triple line. Interfacial energy can be found from this angle if surface energies are known for the solid and liquid using Young's equation, shown here as Equation 2.3.

$$0 = \gamma_{LG} \cos(\theta) + \gamma_{SL} - \gamma_{SG} \quad (2.3)$$

In this equation  $\theta$  is the contact angle between the liquid and solid, as shown in Figure 2.3 and all other variables represent the same terms as in Equation 2.1.

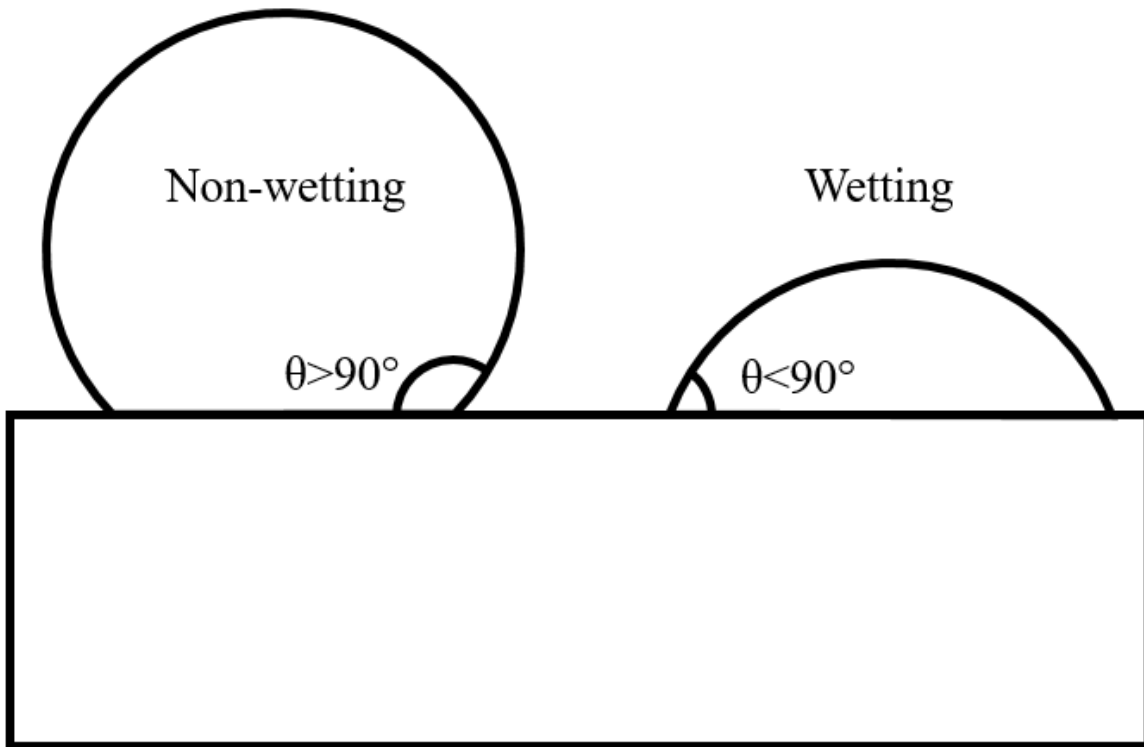


Figure 2.3 Wetting and non-wetting molten droplets on a substrate.

The Young equation is derived via a force balance at the triple line; the cosine term exists to resolve the force vector not lying along the substrate surface. Again, multiple experimental methods exist to determine  $\theta$ , the simplest being the sessile drop wettability test. In this method,

a sample of the liquid rests upon the substrate and achieves a measurable contact angle. Placing a droplet of water on a surface and measuring the angle made is an example of a sessile drop wettability test. Wettability tests for brazing systems are always conducted above 450 °C. A factor to be considered in wettability testing is the increasing influence of gravity with the size of the molten droplet. Water serves as a sufficient example system here since experience with the liquid is ubiquitous. When water is spilled on a table, a closer examination of the water-table interface shows the influence gravity has on contact angle. Most spills will generate a distribution of droplet sizes as well as a puddle. Looking closer, the droplets and the puddle have different contact angles despite their identical thermodynamic surface energies due to the influence of gravity. This phenomenon occurs because gravity acts as an additional force on the system and invalidates the Young equation, which does not account for gravitational effects. Gravitational forces act as another force at the line between solid and liquid as well as altering droplet shape. Smaller droplet sizes are therefore preferable, but too small of a droplet size has issues with chemical composition shifts from the increased surface area to volume ratio and volatilization of high vapor pressure elements. The only way to simultaneously address both issues is to do sessile drop wettability testing in a zero gravity environment, which is impractical in most experimental settings.

Wettability test methods besides the sessile drop have their own benefits and disadvantages. A popular technique is the capillary rise method, where tubes of the substrate material of interest are dipped into a molten bath of liquid filler, which then rises into the tubes. Contrary to the sessile drop method where gravity is a concern, the capillary rise technique depends upon gravity to arrest the rise of the liquid through the capillaries. Capillary force depends on the diameter of the tube, the contact angle between the solid and liquid, and interfacial energy between the solid and liquid, which is the quantity of interest [23]. The equation describing the height reached based on the force balance between capillary action and gravity, known as Jurin's law, is shown in Equation 2.4.

$$h = \frac{4 \gamma_{LG} \cos(\theta)}{\rho g d} \quad (2.4)$$

In this equation, h is height reached by the capillary rise,  $\rho$  is the density of the liquid, g is the acceleration from gravity, and d is the inner diameter of the tube. Note the equation only applies for tubes with a diameter less than the capillary length,  $L_c$ , given in Equation 2.5.

$$L_c = \sqrt{\frac{\gamma_{LG}}{\rho g}} \quad (2.5)$$

In equation 2.4, Jurin's law does not explicitly give the interfacial energy between the solid and liquid but can be rearranged by substituting in Young's law. The modified version gives the solid-liquid interfacial energy if the solid-gas interfacial energy is known, as shown below in Equation 2.6.

$$h = \frac{4 (\gamma_{SG} - \gamma_{SL})}{\rho g d} \quad (2.6)$$

The capillary rise technique is especially well suited for brazing systems because it is a more direct corollary to the flow of filler metal between the faying surfaces. This conclusion does not necessarily mean capillary rise is the optimal test method for any given system, as the sessile drop method is simpler to perform. In the case of this work, capillary rise is not as insightful because the heating scenarios unique to laser brazing are not replicable with a molten bath.

What is not captured by these methods is how variables impact each of the quantitative values of the surface energy terms. In the case of  $\gamma_S$  and  $\gamma_L$ , the cohesive forces intrinsic to the system under a given set of thermodynamic variables drive the surface energy term. The term  $\gamma_{LS}$  is the measure of adhesive forces between the solid and liquid. Surface conditions can change the surface energy of a solid [24]. The surface energy of solids changes in the presence of contamination and by the extent of oxidation. In materials such as SiC, there can be surface energy changes depending on whether a surface is terminated by C or Si atoms, which in turn affects wetting. Chemical reactions can alter which species terminates the surface, including oxidation and filler/substrate interactions. Silicon carbide is susceptible to oxidation and may actively oxidize or form a passive oxide layer under different atmospheric and thermal conditions [25]. Active oxidation removes material from the surface of SiC by forming SiO and CO, which are both gaseous. Passive oxidation of SiC forms a SiO<sub>2</sub> layer. Active versus passive oxidation can be determined with a Pourbaix diagram. Further oxidation requires diffusion of oxygen and/or Si through the oxide layer. Oxygen is typically the element that diffuses, as Si is a larger atom and thus has lower mobility through the SiO<sub>2</sub> layer [2]. The differences in chemical and structural makeup between SiO<sub>2</sub> and SiC lead to different thermophysical properties,

including surface energy. The interfacial energy of the filler/SiO<sub>2</sub> layer is also different for a given molten filler compared to the interfacial energy between the same molten filler and a SiC surface. In metallic systems the problem of oxidation can be resolved with the addition of a flux.

Fluxes are a substance added to a brazing system to remove oxides and other contaminants from the faying surfaces and serve as a protective barrier against further oxidation during the process. Fluxes contain an assortment of compounds depending on the material systems and application but are always designed to melt at a lower temperature than the braze itself [18]. Flux with a higher melting point than the filler would not be able to flow through the joint before the braze and provide the cleaning action required for a sound metallurgical joint.

Issues arise with flux entrapment, as solidified flux has poor mechanical properties. Once a clean metal surface is established, wetting is driven by the compatibility between the substrate and the filler, as captured by the term  $\gamma_{SL}$ . In metallic systems, compatibility is determined by the potential for the filler and the substrate to form an alloy. If alloying is present then  $\gamma_{SL}$  will be large and can overcome  $\gamma_S$ , leading to wetting and joining. Wetting occurs because the filler will locally alloy and/or dissolve the substrate at the interface. In some cases, dissolution may be too great and erode the substrate, resulting in material loss and a potential increase in the melting point of the braze until the filler metal solidifies [28].

Ceramic systems do not typically employ a flux during brazing. Many ceramics are oxides, so a flux designed to remove oxides would be inappropriate. Silicon carbide is not an oxide ceramic, but fluxes are still avoided. A technique called active metal brazing serves as an alternative. Active metal brazing is a technique wherein an element with a higher affinity for at least one of the elements comprising the ceramic substrate is added to the braze. For SiC, elements such as titanium and vanadium can be added; the two elements are strong carbide formers, both having a higher affinity for the carbon atoms in SiC than the Si itself [28].

Active metal brazing modifies the surface of the ceramic being joined to be more compatible with the liquid filler. The joining process is accomplished through the formation of a reaction layer as well as diffusion of the active element into the ceramic material. Creating a reaction product layer, in part, works by altering the crystalline misfit between the substrate and the solid to be formed from the filler metal. In two experiments where pure C of the diamond allotrope was brazed using an Ag-Cu-V and Ag-Cu-Ti filler, respectively, heterogeneous

nucleation of the non-active elements in the filler was accommodated by formation of reaction products between the active elements and the diamond [29,30]. A large reason for this result is the crystalline misfit between the solidifying metals and the substrate surface. During solidification on a substrate, the atoms of the solid formed must be able to accommodate some amount of strain due to a lack of a perfect 1:1 match between the lattices of the substrate and solid nuclei. A smaller crystalline misfit reduces this strain energy by requiring less local deformation from the solid forming, in turn reducing the total energy required to bond to the substrate and strengthening the bond overall. Figure 2.4, taken from a paper on brazing different crystallographic planes of diamond, shows the difference in crystalline misfit between different planes of the TiC reaction product and diamond surface [30]. In this figure, the TiC (111)/Diamond (100) interface will exhibit smaller misfit indicating a greater probability of TiC nucleation than Cu or Ag.

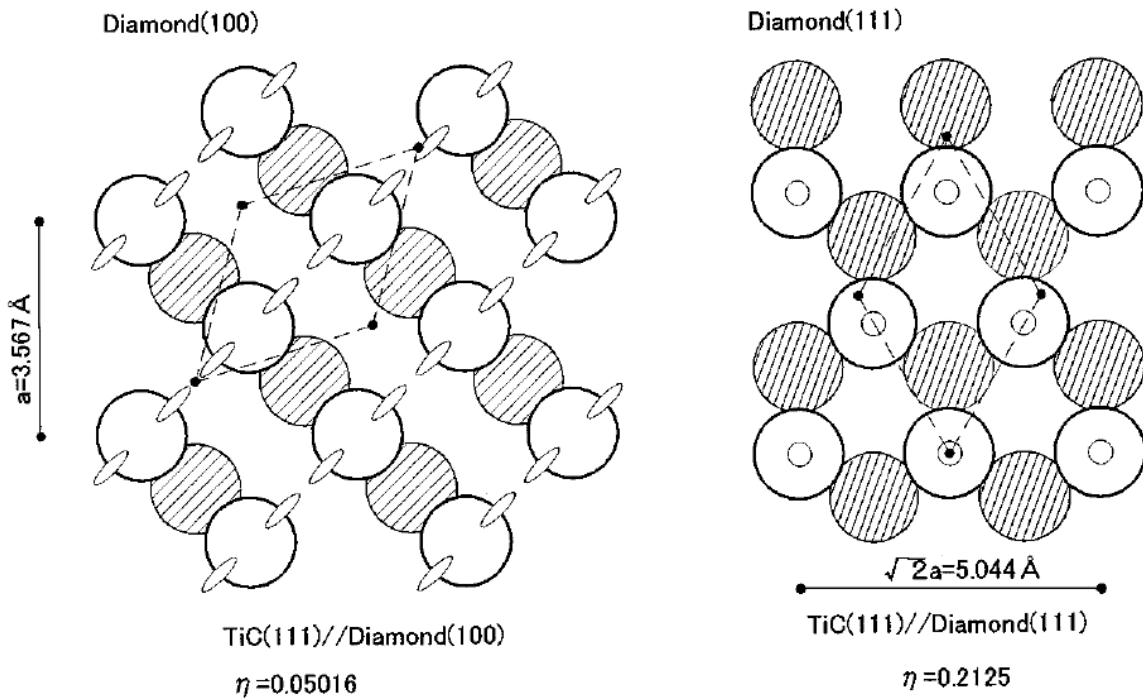


Figure 2.4 Misfit between TiC and diamond on different planes, with ellipsoids and small circles representing free C bonds, light circles as C-terminated TiC surface, and  $\eta$  means misfit [30]

The TiC surface is more amenable to subsequent nucleation of the silver and copper phases in the filler. Essentially, the reaction product layer will act as an intermediary between the ceramic and the metal to allow for bonding. Another way to accomplish a similar effect is by prior metallization of the ceramic surfaces. This process exposes the entire ceramic to

contamination and diffusion of deleterious elements from the metalizing process instead of only affecting the faying surfaces as in active metal brazing.

The active element is not only limited to forming a reaction layer, as it also diffuses into the ceramic substrate and remains after joining. Diffusion can be an issue in ceramic systems, as the active element may be considered a contaminant. Silicon carbide is not an exception with Ti known to diffuse into SiC. Figure 2.5 shows a backscattered electron image of a SiC to 316 stainless steel joint with Ag-Cu-Ti filler, including the results of an electron probe microanalysis line scan [31].

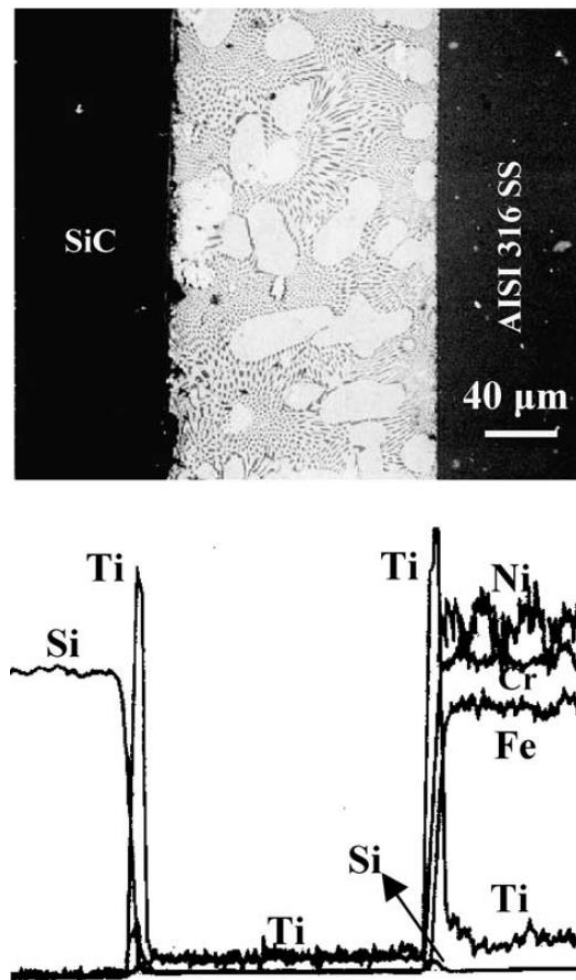


Figure 2.5 Electron backscattered electron image and EPMA scans of 316 stainless steel joined to SiC with Ag-Cu-Ti filler, taken from [31]

The active element in an active metal braze strongly segregates to the faying surface and diffuses inwards. Enough diffusion occurs to largely deplete the active element in the middle of

the joint, leaving behind a microstructure dependent on the elements left behind. The tendency of active elements to segregate towards the ceramic faying surface is enough for joints to see the active element in the base metal migrate through the braze to the ceramic faying surface even if the sole source of the active metal is from the metal rather than the braze. This scenario can occur with undesirable elements and prevent successful joining, which can be solved with interlayers between the faying surfaces [32]. Interlayers also mitigate residual stress issues from different coefficients of thermal expansion (CTE) between the ceramic and metal, but SiC has a CTE closer to the range of metals than most ceramics.

Active metal brazing is a reliable technique to join SiC. One of the first active metal fillers developed to join SiC was a Ag-Cu eutectic with varying amounts of Ti. This design offers two advantages: Ag-Cu eutectic brazing fillers are commonly incorporated in joining metals and readily available and adding Ti to the system is as simple as re-melting. Ag-Cu-Ti filler was also used to join other ceramic systems such as Al<sub>2</sub>O<sub>3</sub> and Si<sub>3</sub>N<sub>4</sub>. While this filler system successfully wets and joins SiC through the formation of a reaction layer, the melting temperature of Ag-Cu-Ti fillers is too low for applications in turbines. A filler consisting of pure metals would give the highest melting point achievable, but most pure metals do not wet SiC [34]. Table 2.1 [34] summarizes the experimental contact angles of selected metals with SiC in an argon atmosphere heated by induction.

It can be seen in Table 2.1 that Si and Ni filler formed small wetting angles. Tin and copper, on the other hand, showed large wetting angles, indicating poor wettability. Copper metal will form a reaction layer with SiC comprised of copper silicides instead of copper carbides. Silicon carbide is different from many other ceramic systems in that Si tends to form silicide compounds with a range of other elements alongside or to the exclusion of carbide compounds. As seen in copper, these silicides do not necessarily promote as good wettability as the titanium carbide layer. Nickel silicide is an exception in that it acts to achieve wetting. Note that reaction layer formation is not all that is needed for joining; the layer formed must also be compatible with the remainder of the filler. The low contact angle of Si without the presence of a reaction layer exemplifies how wetting is controlled by surface energies between different substances and how the reaction layer only exists as a way of modifying the surface energy and solid-liquid interfacial energy of an otherwise unfavorable surface. Thermodynamics predicts

reaction layer formation if the kinetics of the reactions is favorable. Thermodynamics also predict the formation of silicides, carbide, or both. Figure 2.6 provides Gibb's free energy of formation for carbides and silicides for a range of elements with SiC at 0 K serving as the reference energy in an Ellingham type diagram [35].

Table 2.1: Contact angles of selected filler metals in an argon atmosphere heated by induction [34].

| System                             | T (K)             | $\theta$ (degrees) | $W_a$ (JM <sup>-2</sup> ) | $\gamma_{sl}$ (JM <sup>-2</sup> ) |
|------------------------------------|-------------------|--------------------|---------------------------|-----------------------------------|
| $\alpha$ -SiC (polycrystalline)/Si | 1683              | 38.25 $\pm$ 0.44   | 1.346                     | 1.489                             |
|                                    | 1710              | 37.27 $\pm$ 0.13   | 1.350                     | 1.468                             |
| $\alpha$ -SiC (monocrystalline)/Si | 1770              | 37.96 $\pm$ 0.52   | 1.338                     | 1.444                             |
| $\beta$ -SiC/Si                    | 1740              | 41.49 $\pm$ 0.33   | 1.312                     | 1.488                             |
| $\alpha$ -SiC(polycrystalline)/Sn  | 523               | 154.11 $\pm$ 1.42  | 0.054                     | 3.203                             |
|                                    | 598               | 152.34 $\pm$ 0.51  | 0.061                     | 3.149                             |
|                                    | 623               | 151.23 $\pm$ 0.48  | 0.066                     | 3.130                             |
|                                    | 673               | 148.86 $\pm$ 0.96  | 0.077                     | 3.088                             |
|                                    | 723               | 145.30 $\pm$ 1.20  | 0.094                     | 3.040                             |
|                                    | 798               | 142.74 $\pm$ 1.16  | 0.107                     | 2.980                             |
|                                    | 823               | 142.01 $\pm$ 0.68  | 0.111                     | 2.962                             |
|                                    | 848               | 141.79 $\pm$ 0.52  | 0.111                     | 2.946                             |
|                                    | 873               | 141.29 $\pm$ 0.88  | 0.114                     | 2.927                             |
|                                    | 923               | 139.98 $\pm$ 0.77  | 0.121                     | 2.890                             |
|                                    | 1023              | 135.16 $\pm$ 0.49  | 0.148                     | 2.801                             |
| 1073                               | 133.51 $\pm$ 0.48 | 0.157              | 2.761                     |                                   |
| $\alpha$ -SiC(polycrystalline)/Cu  | 1423              | 133.15 $\pm$ 1.41  |                           |                                   |
|                                    | 1583              | 129.45 $\pm$ 1.10  |                           | (Reaction)                        |
|                                    | 1723              | 124.36 $\pm$ 7.77  |                           |                                   |
| $\beta$ -SiC(polycrystalline)/Cu   | 1423              | 157.09 $\pm$ 3.25  |                           |                                   |
|                                    | 1573              | 142.00 $\pm$ 9.68  |                           | (Reaction)                        |
|                                    | 1716              | 129.70 $\pm$ 6.23  |                           |                                   |
| $\beta$ -SiC/Ni                    | 1770              | 74.00              |                           | (Reaction)                        |

Titanium tends to form silicides and carbides in parallel during wetting of SiC [35]. The creation of multiple compounds can be beneficial, as compounds may exist which wet to one phase but not to another. When silicides and carbides are both present on the interface the range of liquid metals which may heterogeneously nucleate to solidify increases. Titanium is not alone

in forming silicides and carbides with SiC: zirconium, hafnium, chromium, tantalum, tungsten, and molybdenum share this property [35]. Titanium is preferable to these elements because it is the lightest and thus more suitable for turbines. Titanium is also less expensive than most of these other elements based on current market prices.

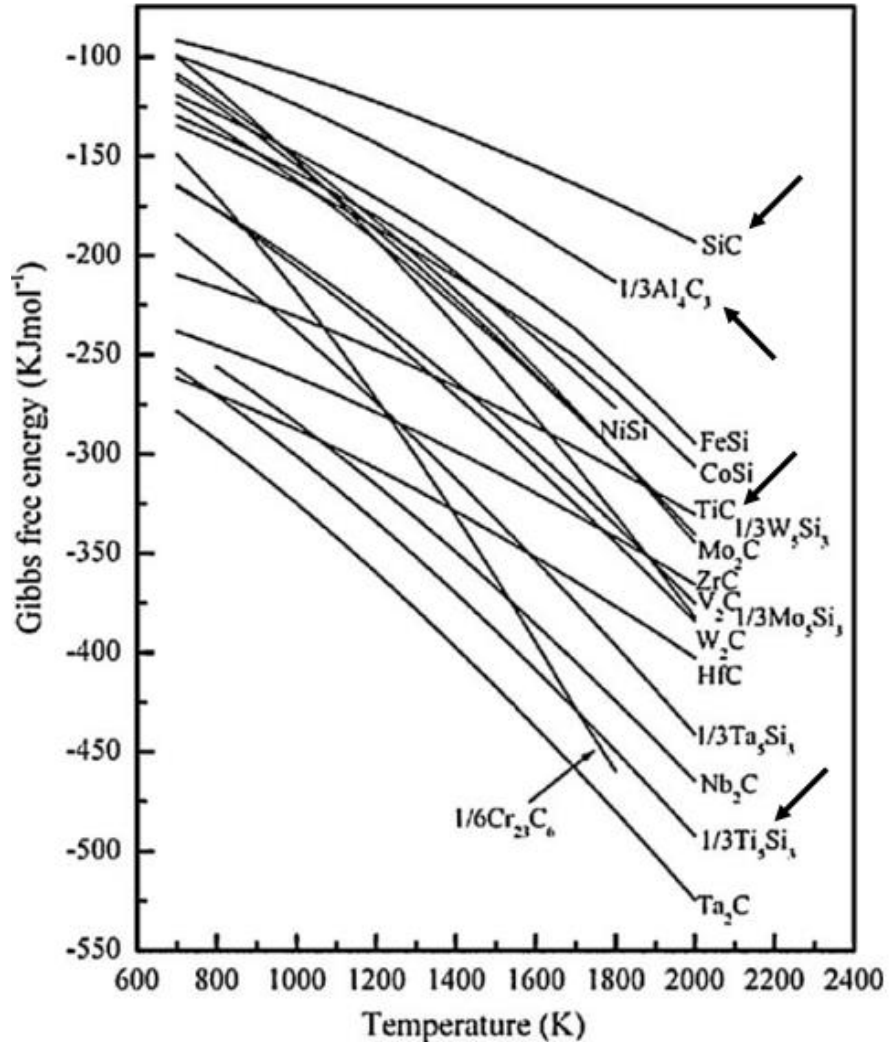


Figure 2.6 Ellingham type diagram for the formation of carbides and silicides with SiC at 0 K as the reference energy, as taken from [35]

### 2.2.3 Oxidation Effects

Active elements come with their own challenges, most notably oxidation. All the elements previously mentioned that form silicides and carbides with SiC are also strong oxide formers, with oxidation predicted to occur below even 1 ppm of oxygen. Silicon metal normally wets on SiC, but oxidation increases the contact angle from values of 40° to as much 76° for tests

performed between 1000 and 1200 °C [36]. This phenomenon of decreasing wettability occurs because metals and their oxides are different materials with different bonding structure and properties; therefore, metals and their oxides naturally present different wetting behavior. The flow of liquid filler metal occurs at the triple line, so if oxide is present at this point instead of bare metal the oxide would determine the local equilibrium instead of the metal. If the oxide has a low liquid-solid interfacial energy with the filler, then the oxide prevents wetting even if the metal has a favorable liquid-solid interfacial energy.

Oxygen influences the wetting behavior of active elements in other ways. Depending on the activity of oxygen in the system, oxygen can aid wetting on oxide ceramics by facilitating surface adsorption of the wetting liquid [37]. The activity range within which this phenomenon occurs varies across metals. In most circumstances, it would be more proper to just prevent excessive oxidation from occurring. A vacuum environment is the most obvious solution for oxidation but attaining high vacuum can be a challenge. Back-filling and purging with inert gases lessen the need for a high vacuum but still has long processing times. Using a vacuum also negates the time saved by implementing a laser heat source since establishing a vacuum takes a long time relative to the few minutes needed for laser processing itself.

Inert gas atmospheres can resolve the oxidation issue, but the gas must be of high purity to avoid oxidation of active elements. Oxidation occurs at partial pressures as low as  $10^{-5}$  bar  $O_2$  and lower, which corresponds to 99.999% pure Ar gas at one bar of pressure. Using an atmosphere partially or completely comprised of reducing gases serves as another solution to oxidation and works for many systems. However, some systems form new deleterious compounds when exposed to common reducing gases. Examples include aluminum hydride which is water soluble and silicon hydride which is a pyrophoric gas. Carbon monoxide and hydrogen, the two most common reducing gases, are also toxic and explosive, respectively. These hazardous properties do not prevent the gases from serving as options but do complicate implementation.

Some more exotic solutions to oxidation exist. Because oxidation reactions are fundamentally redox reactions involving the transfer of charge, the reactions can be counteracted and even reversed with applied voltage. Experimental work saw reduced contact angle by controlling oxidation behavior with applied voltage [38].

Another approach to the oxidation problem is to join with oxides. A filler material is not required to be metallic in nature. The selection of oxides of adequate chemistry can create enough flowability for the filling of the braze gap. A group in Germany has been researching oxide-based filler for laser joining of SiC since the early 2000s, with the most recent composition released from 2016 at the time of this writing [39-42]. In their work, the researcher's main motivation was to encapsulate fuel with SiC in nuclear reactors for a high operating temperature. Metallic systems, metal silicide systems, exothermically reacting Ti-C-Ni systems, and oxide systems were considered as options for filler systems. The researchers concluded that oxide fillers in the  $Y_2O_3 - SiO_2 - Al_2O_3$  system were optimal for their goals. Reasons for this choice include the ability to tailor melting point by modifying proportions of the three components, capacity to join in open air, high temperature stability, and matching of coefficients of thermal expansion to reduce thermal stresses from joining. A reaction between the filler and the substrate still occurred in this instance. Silicon dioxide originally existed on the surface of SiC due to passive oxide formation and would melt and join the filler during brazing. Sintering aids mixed in with silicon carbide would also become part of the filler and modify the properties of silicon carbide. Thus, different types of silicon carbide have varied interactions with these oxide fillers. Finally, since the research goal was to encapsulate fuel material to contain fission products, the joints must be leak tight. The researchers report low leak rates of helium maintained at 900 °C exposures and strengths of  $112 \pm 52$  MPa. The hermeticity and acceptable strength of the joint created indicate oxide fillers can join silicon carbide.

Not all reaction with the substrate is beneficial. Erosion is a concern for brazing metallic systems, and elements can be "too active" with ceramic substrates and cause cracking. Cracking is observed in silicon carbide exposed to molten nickel [43]. Thus, active metals may promote the formation of a joint incapable of bearing any meaningful loads. Large coefficient of thermal expansion mismatch creates thermal stresses large enough to generate microcracks in silicon carbide, which would occur when joining a SiC piece to a cobalt-matrix tungsten carbide composite with a Ag-Cu-Ti filler and laser heat source [44]. Despite the cracking, this reported work demonstrates that silicon carbide would be capable of surviving laser heating through its combination of thermal conductivity and thermal shock resistance. Fracture occurring during cooling after the filler metal was bonded to the SiC indicates the contraction of the filler metal is greater than the SiC caused the cracking. Laser heating, despite its highly localized nature, can

still produce even heating throughout the filler metal. The paper cited also performed simulations of the heating and cooling response from their laser processing parameters using the LS-DYNA solver for finite element analysis. Results from experimentation and finite element simulations both show even temperature distributions throughout the filler metal even with laser heating of the base materials and no direct heating of the filler itself [44].

#### **2.2.4 Other Non-fusion Joining Techniques**

Joining SiC requires non-fusion joining techniques, but brazing is not the only non-fusion joining technique available. Other ways of joining SiC exist, though these methods do not as readily solve the problem of joining SiC to dissimilar materials. The different approaches will be discussed below.

The most straightforward way to join silicon carbide is to simply join in the green state and then sinter. Sintering after joining cannot make SiC-metal joints because the sintering temperatures required for silicon carbide would melt nearly all non-refractory metals. Even in the case of refractory metals, creep may occur since sintering is often conducted under high pressure and high temperature. There are variants of this method that do not involve the use of pressure [46].

Green-state sintering is accomplished by adding material between the two bodies to be joined. Paste containing particles of SiC with a binder and possibly additives to aid in joining is applied between the two surfaces. A combination of pressure, temperature, and time remove the binder through pyrolysis [45]. Gas bubbles may form during pyrolysis of the binder, compromising the integrity of the joint. Temperatures required for sintering remain high, specifically 2150 °C. Joining in the green state also has intrinsic challenges with dimensional tolerances from shrinkage during sintering. When joining dissimilar ceramics, an even greater challenge arises because of the stresses that develop from different shrinkage rates during sintering. More specifically in the case of RB-SiC, joining in the green state will not work because it is not a sintered material and therefore never exists in a green state.

Using SiC particles embedded in a binder can join sintered SiC. A binder containing SiC particles and other additives as needed is applied between the pieces of SiC to be joined and heat is applied until a joint is formed [47]. This process is generally performed in an inert atmosphere.

Again, porosity created during pyrolysis of the binder is a concern that must be addressed when using this technique.

A similar method using powders in the joining area with applied heat and pressure may be implemented to join RB-SiC. The key difference between each method involves the ceramic which remains after pyrolysis - in this case, the ceramic is silicon oxycarbide rather than silicon carbide [48]. Shear strength increased from as low as around 4 MPa at 1000 °C to an average of approximately 21 MPa at 1200 °C. These experiments were also conducted in an inert atmosphere to prevent loss of carbon from the formation of either CO or CO<sub>2</sub> by oxidation from air.

SiC can also join to itself after sintering by hot pressing [49]. Surface roughness creates irregularities that may frustrate joining, so adding SiC powder between the joining surfaces makes creating a sound bond easier. Hot pressing will not work to join SiC to metals due to different melting points.

In contrast to the other joining techniques discussed, diffusion bonding can join dissimilar materials. Creating a diffusion bond requires applying pressure over time at temperature in a vacuum environment. The cost of equipment capable of simultaneously performing all three of these operations can range into the millions. Similar and dissimilar materials can be joined with this process [50]. Interlayers may or may not be implemented on a case by case basis. Because the entire component experiences the same temperature, residual stresses are reduced. However, thermal stresses caused by coefficient of thermal expansion mismatch are not reduced and exposing the entire component to temperature may cause undesirable changes in microstructure. Furthermore, the vacuum chamber required for this process places a strict limit on the maximum dimensions of a part to be joined. The process also takes a few hours as compared to the few minutes required for laser brazing. Diffusion bonding is also not practical for the repair of components because of the pressure required for joining. Overall, diffusion bonding exists as an option for joining silicon carbide with advantages and disadvantages relative to brazing and each process has its own application space with some overlap.

### 2.3 Laser Processing Experimental Techniques

This section contains information on some of the equipment involved and principles behind experimental procedures.

Laser is an acronym for “Light Amplified by Stimulated Emission of Radiation”. Exact details on how a laser beam is created are beyond the scope of this thesis. Three characteristics of laser light distinguish it from other photon sources: laser light is monochromatic, phase coherent, and collimated. Monochromatic means the photons comprising the beam possess the same wavelength and energy. Phase coherency refers to the peaks and troughs of each photon aligning with each other. The peaks and troughs referenced can be energy, electrical field, or magnetic field. Collimation refers to the photons traveling parallel to one another instead of being emitted radially in all directions as in a light emitting diode or fire.

The principles of thermodynamics prevent an ideal laser beam from existing. If a laser beam was perfectly collimated with no error, then the laser would be able to travel indefinitely without diverging. If a beam never diverged, entropy would remain constant forever or until the beam impinged on a surface. A system having constant entropy indefinitely defies the laws of thermodynamics, so perfect collimation is impossible. Laser beams are also never perfectly monochromatic or phase coherent, but the deviation is small enough to be ignored for the purposes of this research. Imperfect collimation is significant as a focusing lens must be added after the beam has been collimated to achieve the desired beam diameter. Consequentially, laser beams can be focused or defocused depending on the strength of the lens and the distance to the target. The intensity of the beam also varies throughout its profile. Beam intensity profiles can take on several shapes, known as transverse electromagnetic modes [51]. These profiles are depicted in Figure 2.7 [51].

Most lasers in industry operate in the 00 or 01\* mode. Figure 2.7 only shows where actual laser radiation exists and does not show the magnitude of the radiation within the profile. By default, the intensity profile follows a Gaussian distribution. Depending on the application, different profiles may be desired. Creating these profiles requires various optics geared to the desired profile [52]. The heat imparted to the SiC at the point of impingement will conduct radially throughout the bulk.

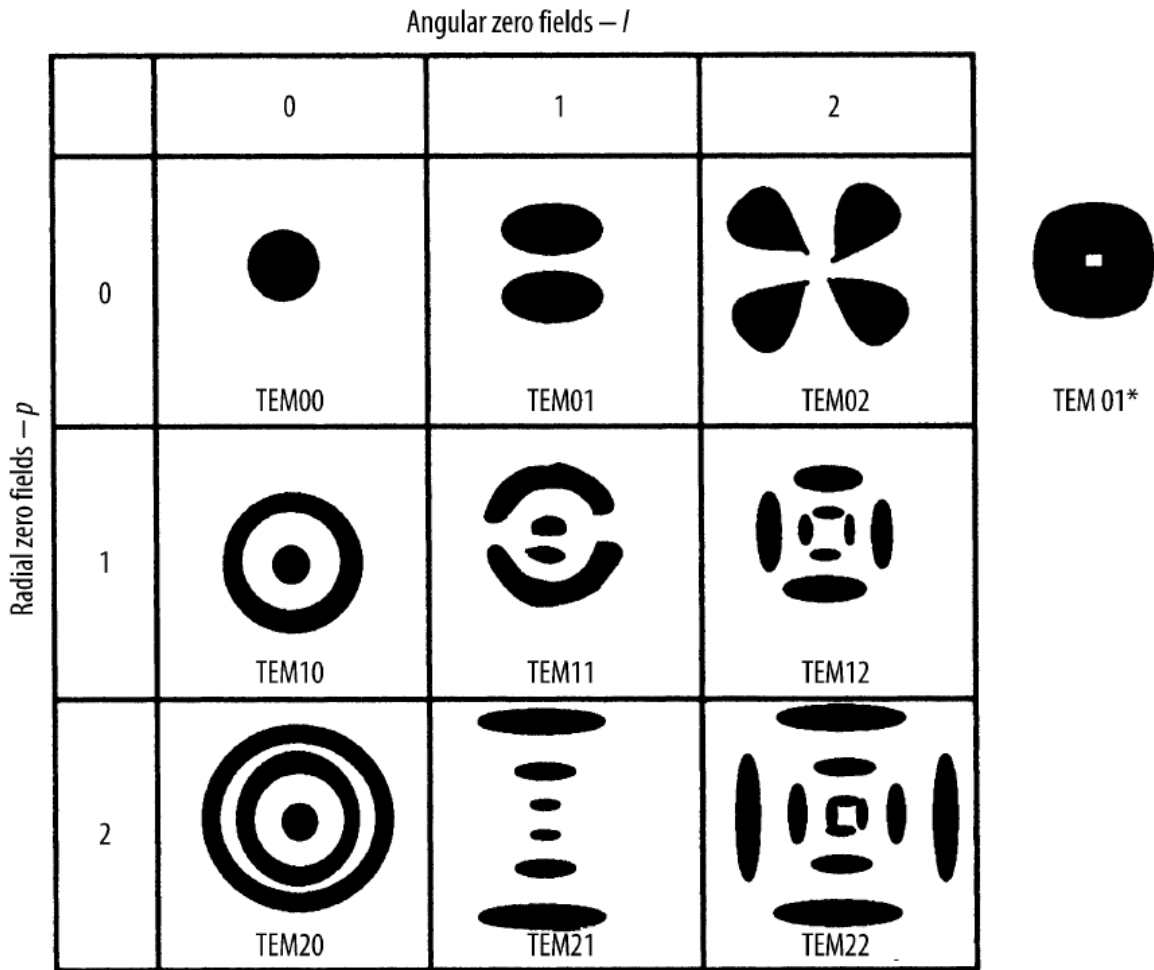


Figure 2.7 Intensity profiles for transverse electromagnetic modes in laser beams [51]

Altering beam diameter and intensity has a significant impact on the base substrate. Laser heating with a focused beam is the second most effective way to locally introduce heat into a material, only less than electron beams in energy density. A focused beam with high energy density can damage the substrate. An uncontrolled beam diameter also allows laser radiation to impinge upon regions intended to be heated only through conduction from the initially heated region. Beam diameter must be known to calculate the average intensity and the maximum safe intensity of the beam. Direct measurement of beam diameter is precisely taken via optics [54]. A more practical, but less precise method, for determining beam diameter is to irradiate holes in a target and then measure their diameters. This method is advantageous when the knowledge of the exact beam profile is less important than knowing the edge of sufficient radiation that can cause alterations to the substrate. If the target was struck with the beam enough times to develop a hole with clean edges, the beam diameter is simply the diameter of the hole made [54]. Targets with

low thermal diffusivity and a low temperature of either decomposition or vaporization are preferred. These two factors prevent heat from spreading further than the true diameter of the laser and over-measuring the diameter. Kapton™ film satisfies these requirements and is readily available. Laser pulses instead of continuous radiation mitigate this problem as well.

Typical gap sizes in brazing are quite small and the filler material is different than the base material(s). Thus, thermal cycling (heating and cooling), phase transformations and mechanical loading will cause the development of a triaxial stress state. In service, braze joints are often designed to be subjected to shear stress; however, a pure shear stress state is not realistic because of the existence of bending components that would result in tension and compression [55]. Shear testing still applies, as there will also be unavoidable bending stresses in practice considering how joints will perform in assemblies.

Stray radiation can overheat filler metal to the point of vaporization and change the chemical composition. Damage to fixtures may also result.

Chapter 3  
CHAPTER 3: EXPERIMENTAL PROCEDURES

The exact methodologies and processes involved in the research are described here. Section 3.1 describes how the diameter/width of the laser beam at different focal widths was determined. Section 3.2 describes finding the maximum allowable intensity before the RB-SiC is damaged and how temperature control was achieved. Section 3.3 provides details about the synthesis of the filler metal used in testing. Section 3.4 details sessile drop wettability testing procedures, contact angle measurements, and microstructural analysis. Section 3.5 elucidates the creation of single lap joints and their mechanical testing and evaluation. The laser involved in all experimentation is an ytterbium fiber laser made by IPG with a 1070 nm wavelength beam, 1.1 kW maximum power, operated in continuous wave mode, and with no or random polarization. The laser chamber setup used for all experimentation, both wettability testing and lap joint brazing, is pictured in Figure 3.1.

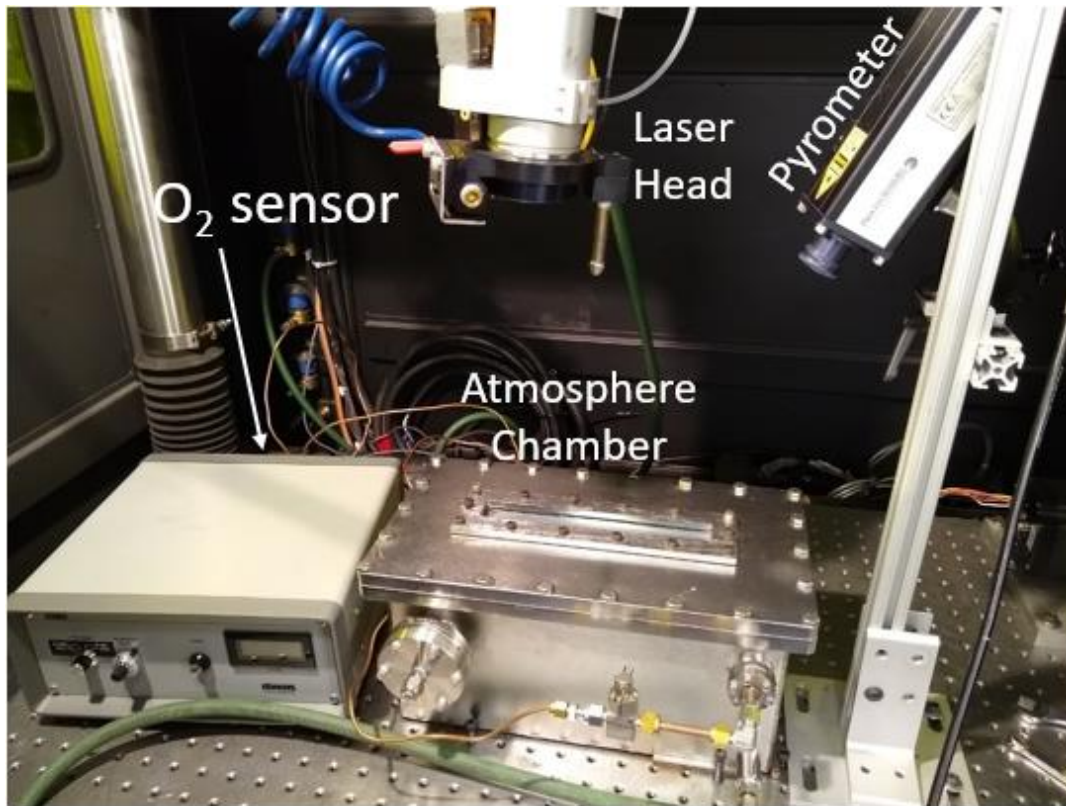


Figure 3.1 Laser chamber used for experiments, including sealed chamber and O<sub>2</sub> sensor for atmospheric control and non-contact pyrometer for temperature measurement

### 3.1 Beam Diameter Measurement

Beam diameter was measured by irradiating holes in Kapton™ film. The film chosen was 50 microns thick and 1 inch wide. Sections of the film were cut out of the roll using scissors and secured in place with masking tape. The samples were placed atop firebrick to limit heat conduction from the backing material. Laser pulses one millisecond in duration with no ramp up or ramp down spaced 0.5 s apart were fired in ten shot bursts. The focal length varied 0.25 inches at a time, with a sharp focus set as the zero point and focal distance always increasing from this length. Note that none of the holes approached the width of the film. Beam powers of 500 and 1000 W were used at each focal length. The edges of the holes were not always completely removed from the Kapton™ film due to beam intensity lessening near the edges, but a single sharp flick by hand was enough to remove these artifacts and permit precise measurement of hole diameter. Images of the holes were taken with an optical stereoscope and measured in ImageJ. Lengths were measured across two orthogonal directions and averaged to account for any eccentricity in the holes. Final calibration of hole diameter versus focal distance ignored hole diameters at focal distances of 1.25 inches away from sharp focus onwards because the intensity was insufficient to make a consistently measurable hole. Beam diameter varies linearly with focal length, so extrapolation predicted beam diameters outside the range of data. Only the linear region of data was used for extrapolation because beam diameter varies linearly except near the focal point. Beam diameter near the focal plane does not narrow down to an infinitely small point but rather takes on a curved shape with the minimum achievable beam diameter in the middle of the curve. Images of the films with the laser-burnt holes and a schematic of how beam diameter varies with focal distance are shown in Figure 3.2.

This image reflects the distortion created in the films when the holes were made. Hole diameters were measured using ImageJ software despite the distortion; these measurements simply required distinguishing between the shadows made by the remaining film and the holes themselves. The shadows appeared substantially darker than the holes, so this was not difficult. The calibrations resulting from laser metrology are shown and discussed in Chapter 4.

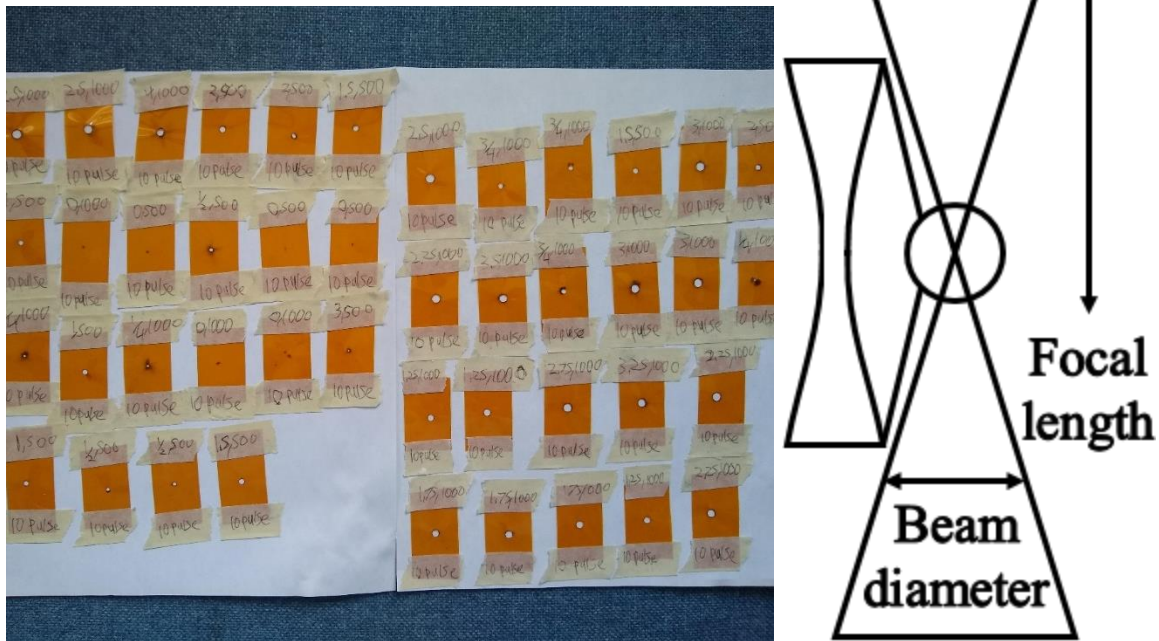


Figure 3.2 Kapton™ films after laser radiation to create holes and beam diameter dependency on focal distance

### 3.2 Substrate Damage Threshold and Preheating

Reaction-bonded silicon carbide has good thermal shock resistance but can be damaged from excessively local and rapid heating. Focused laser beams locally heat materials up quickly, so a threshold of beam intensity to avoid RB-SiC damage is needed. Beam diameter was varied by changing focal distance, hence the need for a beam diameter calibration. Power and exposure time were varied as well. The samples and the beam spot both remained static during the exposure. In wettability and lap testing, the beam will be rastering over the sample. The beam spot was fixed to ensure the intensity was safe and not appearing so by spreading the heat through rastering. Once an intensity that caused detectable cracking was determined, tests with full-minute exposure at a sub-threshold laser intensity were conducted to ensure that the intensity level was safe for experimental purposes. Exposing the sample to the beam for this length of time elevated the temperature of the samples, causing the SiC to glow from gray body radiation. This visual demonstration indicates the sample had successfully survived laser radiation up to the preheating and brazing temperatures.

Knowing safe irradiation parameters enabled samples to be exposed to the beam for the minutes needed to melt filler metal and then form bonds. The procedure of controlling temperature with a system which only controls heat input is quite different from that in a system controlling ambient temperature, such as a furnace. Heat input to the system occurs at a constant rate because SiC does not change absorptivity with temperature at the wavelength of the laser in this work. Heat loss from the system occurs via radiation and convection, which are quartic and linear with temperature, respectively. The temperature of the system is controlled by the balance of heat input and heat loss as a function of temperature, with heat input constant for a given power. Therefore, a given beam power will produce a maximum reachable temperature for a given coupon/part geometry. As well, this maximum temperature is not immediately achieved; time is required for heat to soak throughout the sample to reach a steady state.

The relation between temperature, beam power, and raster time was evaluated by varying beam power and raster time. Power varied from 100 to 500 W in 100 W increments. Beam intensity was kept constant at  $120 \text{ W/mm}^2$  by varying focal distance to match spot size with the diameter needed; higher beam powers had a longer focal distance. The temperature was recorded with a non-contact pyrometer able to measure temperatures in the range of 750 to 2500 °C. Coupons of RB-SiC measuring 1 x 0.5 x 0.125 inches were placed on a piece of firebrick and their surfaces were cyclically rastered over with the laser beam. The beam traveled at a constant speed of 1 in/s. Geometric midpoints of the top surface were targeted by the pyrometer for measurement. Figure 3.3 shows the raster pattern, to scale. Beam diameter is not included in the figure because the diameter was varied to keep intensity constant.

These experiments were performed in open air. Reaction-bonded silicon carbide experiences oxidation in air at high temperature to the degree where the samples would discolor afterward, but this oxidation did not appear to affect the temperature of the system significantly relative to the beam. The laser beam interferes with pyrometer measurements due to similar wavelengths between the signal measured and the laser beam. To resolve this issue, temperature data for calibration purposes was taken at set intervals after the beam had ceased operation. Even though melting in the free silicon regions would affect these results, this same effect persists throughout all tests, thus rendering the data valid and comparable. Data collected while the beam

was on differed from the data immediately after the beam was shut off so data before shut-off are discarded.

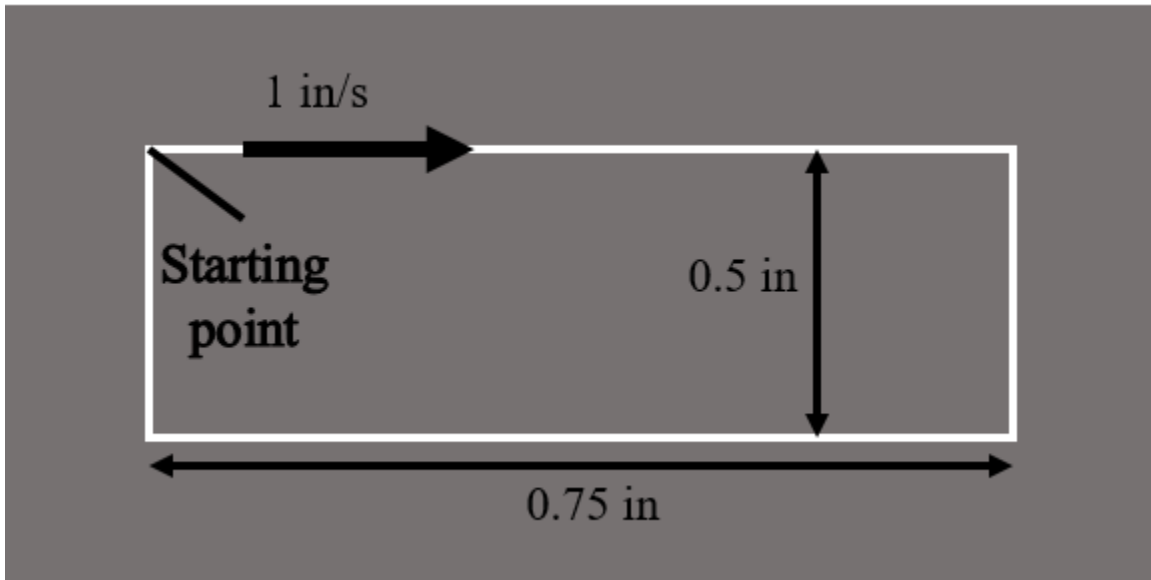


Figure 3.3 To-scale image of raster pattern used for preheating calibration, with the white box showing the raster pattern and gray box showing the RB-SiC surface

Samples were also heated in open air without moving the beam. The pyrometer measurement point was coincident with the beam used for heating. These tests showed severe surface damage because the stationary beam created locally extreme temperatures. The tests were performed to examine what types of surface damage can occur during laser heating if damage thresholds are exceeded without causing a fracture. The surfaces of RB-SiC coupons heated with both moving and static beams were imaged with light optical stereoscopy. These images are shown later.

### 3.3 Filler Metal Synthesis

The filler metal contained Si, Al, and Ti. Silicon came in lumps 99.9999% pure. Aluminum was procured in block form, 99.99% pure. The Ti was in granular form taken from Ti sponge, 99.99% pure. Si and Ti were weighed out to obtain the correct weight fraction. Al was also weighed but sectioned first to generate pieces small enough to result in the correct mass. After weighing, the components were melted together with an arc melter. The metal was shielded by flowing Ar gas for at least 60 seconds before striking the arc. Each melting iteration contained all three elements, though the exact concentrations were not measured during the arc melting

step. Final buttons of filler metal were flipped and re-melted after they were solid and no longer glowing. Chemical segregation was reduced by this second-melting practice, and by increasing the flow rate of the Ar gas, which also increased the cooling rate as the final melt was solidifying. The arc melter was powered by a Miller Dynasty 350 and actively cooled with a Miller Coolmate 3, which used 45% DI water - 55% ethylene glycol coolant and minor proprietary additives to reduce electrical conductivity. The button melting setup is shown in Figure 3.4.

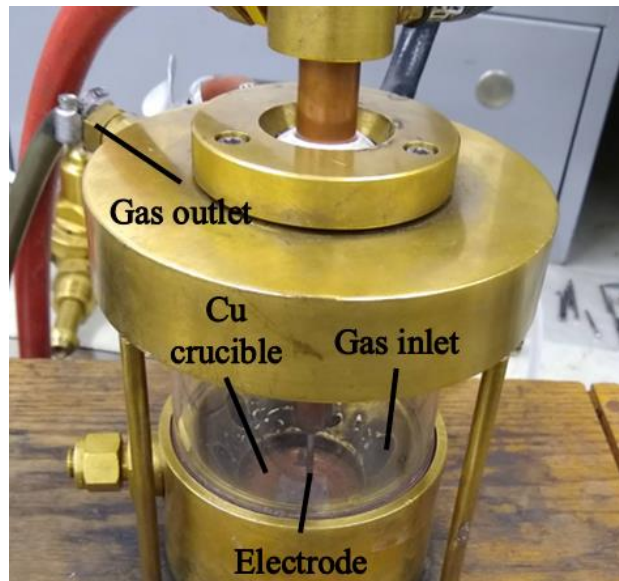


Figure 3.4 Arc melter used to synthesize filler metal

The total mass of the constituents before melting was 10 grams. The weights were checked before melting and after the creation of the final button to ensure no significant losses of components occurred. When sectioning the buttons, care was taken to remove the surface material because of higher oxygen content. Furthermore, the exact composition of the outside surface is more likely to be off-chemistry from the target composition than the interior of the button due to segregation. Many of the arc melted buttons developed an extra growth on the top surface in the later portions of solidification, likely from the Si content, as shown in Figure 3.5.

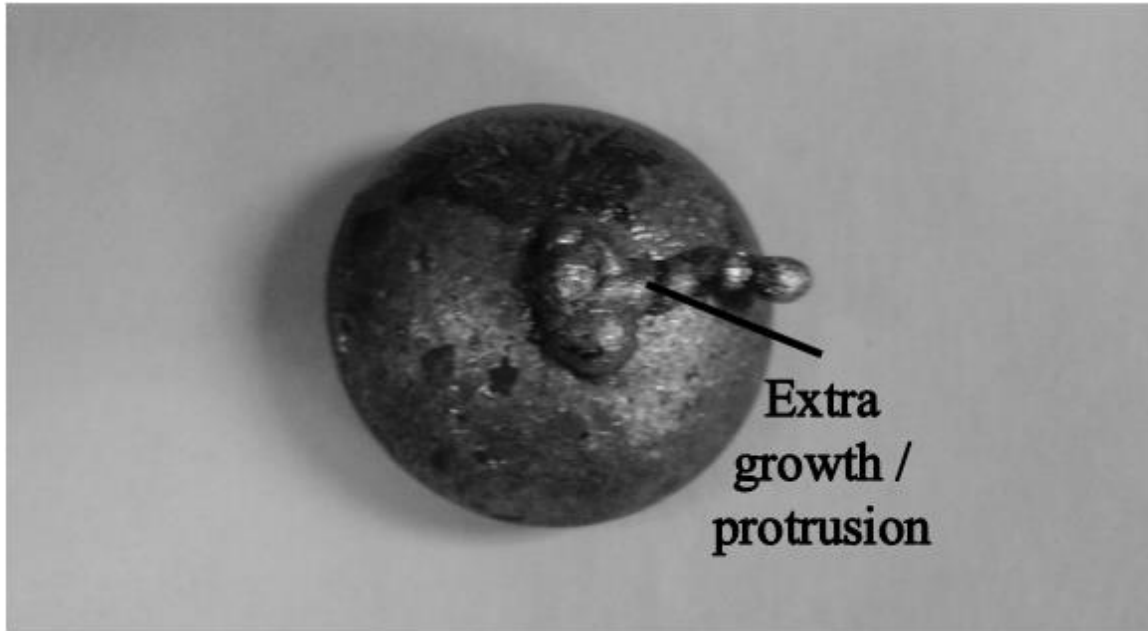


Figure 3.5 Extra growths created during later portion of solidification by Si content, grayscale

The extra material was kept attached for weighing purposes but removed and discarded afterward. Melts where the electrode was noticed dipping into the molten button were discarded and the tungsten was reconditioned before further melting of the filler metal. Reconditioning of the electrodes involved grinding off the metals wetted to the surface, sharpening the tip to approximately a 45° included angle, and truncating the tip by grinding the tip flat.

### 3.4 Wettability Testing

All wettability testing was conducted inside a controlled atmosphere chamber, with Ar and a maximum of 15 ppm O<sub>2</sub>. The pressure inside the chamber was slightly above one bar so in case of a leak, it would lose Ar instead of aspirating air back into the chamber. The chamber was necessary because preliminary testing in air produced no useful results except for a mess of oxides. Filler metal for wettability testing was sectioned out of the buttons as described in Section 3.3. Cuboids were chosen as the geometry of choice, as they are simpler to fabricate, and when kept molten long enough, surface tension would pull the molten droplet into the spherical cap shapes typically observed in sessile drop wettability testing. The cuboids were 0.10 grams in weight and the ratio of their longest axis to the shortest did not exceed two. The samples were cleaned for 15 minutes in ultrasonically agitated acetone at room temperature before experimentation.

The RB-SiC substrates did not experience any surface conditioning before testing besides 20 minutes in an ultrasonically agitated acetone bath at room temperature for cleaning purposes. Two of the RB-SiC samples were textured using the Yb-fiber laser. Each ablation was performed with 10 pulses, each one millisecond long and spaced ten thousandths of an inch from center to center in a square grid. Beam power switched between 150 and 200 W to give different hole depths. The laser-ablated samples showed decreased wetting when compared with unconditioned samples using similar wetting test parameters. These samples were not cleaned before texturing but were cleaned afterward for 20 minutes in ultrasonic acetone at room temperature. No further testing was conducted on textured samples. However, the reason why the textured sample did not enhance wettability is unknown. Surface oxidation, oxy-carbide formation, and loss of Si or C could have been the reason for the low wettability.

Wettability testing followed a three-step beam procedure. In the first step, the laser beam rastered over the surface in the same pattern as in preheat testing described in Section 3.2. The second step consisted of a changing pause time with the purpose of uniformizing the temperature of the substrate. Step three was a secondary raster where the beam irradiated on material closer to the filler metal. Preheat rastering was done with a 200W beam at  $120 \text{ W/mm}^2$  intensity for 60 seconds for all preheated samples. Pause time was varied to control the uniformity of the preheat temperature, as made possible by measuring the temperature after a given time during the preheating tests. Duration of the secondary raster was either 3, 10, or 30 seconds. One particular sample was given a secondary raster time of 300 seconds to determine the effect of significantly extended times on the occurrence of surface reactions. A summary table of the controlled parameters in wettability testing is in Table 3.1.

Beam parameters were identical between the preheat raster and the secondary raster. Filler metal was placed so the geometric center of the largest face was in contact with the geometric center of the RB-SiC coupon surface. The assembly was placed on top of firebrick to match the heat transfer regime from the preheat testing. A to-scale diagram of the secondary raster, beam diameter, and filler metal is shown in Figure 3.6.

Table 3.1 Parameters in Wettability Testing

|                                 | 3 s Secondary<br>Raster | 10 s Secondary<br>Raster | 30 s Secondary<br>Raster | 300 s Secondary<br>Raster |
|---------------------------------|-------------------------|--------------------------|--------------------------|---------------------------|
| No Preheat                      | x                       | x                        | x                        |                           |
| 455 °C Preheat,<br>46.5 s Pause | x                       | x                        | x                        |                           |
| 535 °C Preheat,<br>34 s Pause   | x                       | x                        | x                        |                           |
| 665 °C Preheat,<br>27.5 s Pause | x                       | x                        | x                        |                           |
| 1050 °C Preheat,<br>5 s Pause   | x                       | x                        | x                        | x                         |

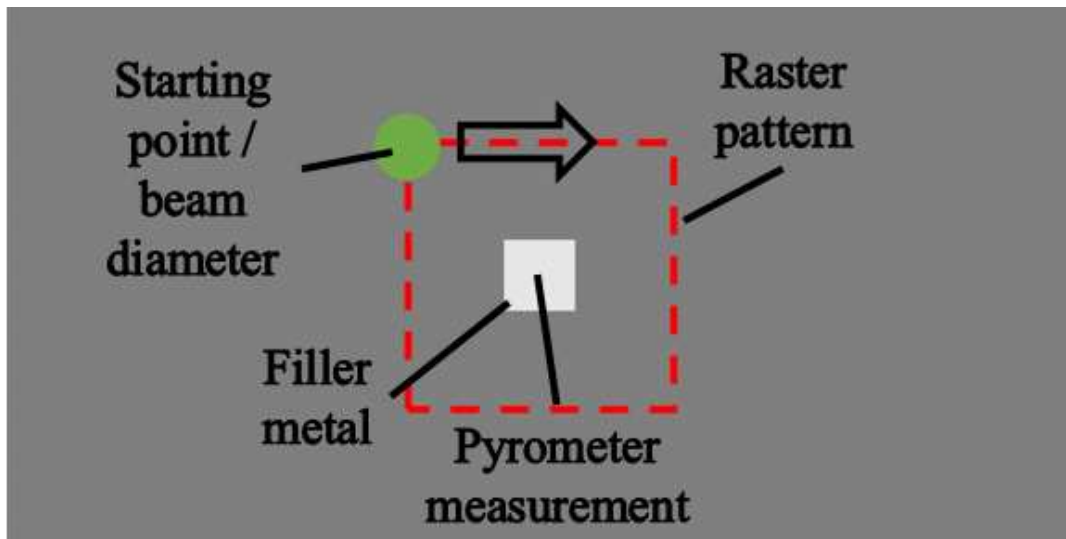


Figure 3.6 To-scale diagram showing beam diameter, size of ideal filler metal cuboid, and raster pattern for secondary rastering in wettability testing

The temperature was recorded with the same non-contact pyrometer in preheat testing, and another pyrometer capable of measuring temperatures between 100 and 700 °C. Instead of recording temperature in the RB-SiC, the pyrometer was aimed at the center of the filler metal. Contact angle was determined after the filler droplets solidified by placing the samples on the side and optically imaging with a stereoscope. Select samples were imaged on the surface with

scanning electron microscopy. Some other samples were sectioned through the middle of the filler metal and transverse to the RB-SiC long axis. Hot mounting created cracks in the RB-SiC from the pressure needed to sinter the mounting media, so all other samples were cold mounted. Regardless of how they were mounted, transverse sections were ground and polished by hand. Hand grinding was done with 180, 320, and 600 grit SiC sandpaper. Contamination is only a concern if particles of the grinding media embed in the filler metal. The surface of the samples and the SiC sandpaper are both covered in a passivation layer that prevents bonding. Additionally, the diamond polishing steps should remove any contamination were it to occur. High pressure was maintained during this process and grinding pads were changed frequently, as silicon carbide grinds itself slowly. Hand polishing involved diamond slurries with a six and one-micron step. The six-micron step involved a high nap polishing pad and the one-micron step used a low nap. Grinding removes material more readily from the filler metal than the RB-SiC since the filler is much softer than SiC grinding media but RB-SiC is at a similar hardness. Consequentially, the RB-SiC surface is more prominent so the first polishing step uses a high nap pad to facilitate leveling out the two surfaces. Low nap polishing media is used in the final step because it is less aggressive and the six-micron step has already leveled the surfaces of the two different materials.

Once polished, transverse sections were imaged by scanning electron microscopy. No etching was done beforehand. Backscattered electron imaging, i.e. contrast by atomic number differences, provided enough contrast to see microstructural features. Energy dispersive spectroscopy was also done to analyze the depth of diffusion for Ti and Al. It was impossible to measure Si diffusion depth into the substrate because RB-SiC is largely made up of Si.

### **3.5 Lap Joint Testing**

A lap joint consisted of two RB-SiC coupons stacked on top of each other with filler metal inserted in between. All the lap joints were held in place during rastering by a silica fixture. The silica fixture was made by carefully carving wax into a negative of the mold shape desired. Iterative dip coatings in a slurry containing silica and binder built up enough material to hold the RB-SiC and filler at joining temperatures. After melting out the wax the binder-silica mixture was fired to create a solid silica shell, which held the joints in place during lasing. Two

such shells are shown in Figure 3.7. The bottom one had seen only one thermal cycle while the top one, several.

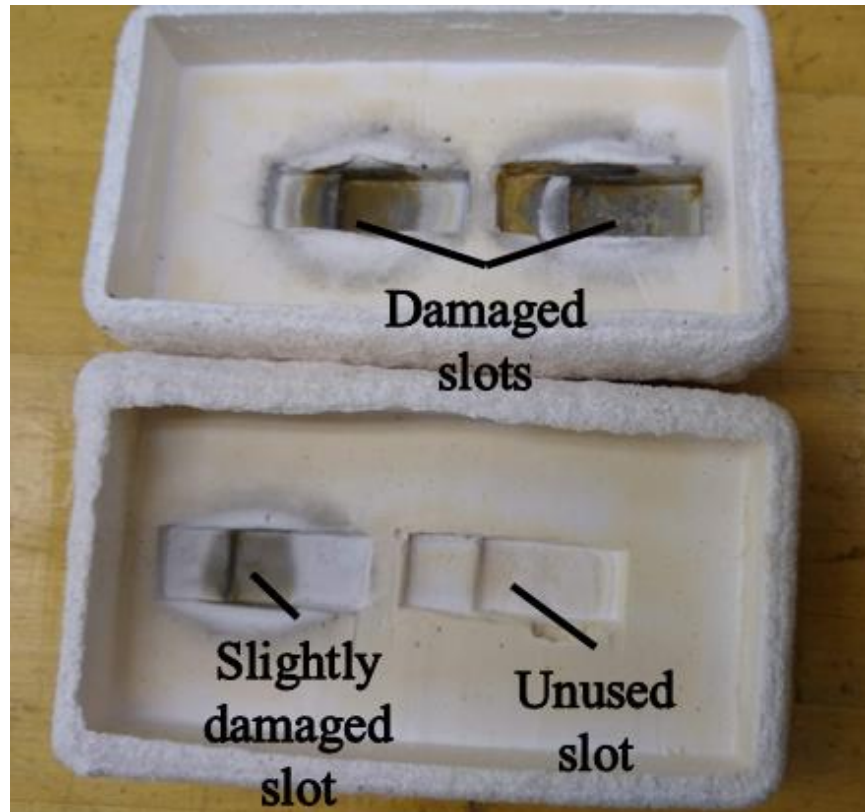


Figure 3.7 Silica shells used to hold RB-SiC coupons and filler metal during joining

The addition of another RB-SiC coupon also affected the heat transfer scenario. Heat loss from the system is proportional to area, so increasing the area of the system by adding more material requires more power in the beam. As such, a new thermal calibration was needed. For the thermal calibration and all lap joint tests, the RB-SiC coupons were placed in the silica mold so 50% of their area overlapped, creating a half inch by half inch overlap region. The spot measured by the pyrometer was always in the geometric center of the top surface of the overlapped region. Every raster pattern also had the spot measured by the pyrometer in the middle of the area traced by the path of the beam. Figure 3.8 shows the geometry of the thermal calibration tests done for the lap joints, with the red line being the beam path, dark gray as the overlapped region, and white spot as the pyrometer measurement point.

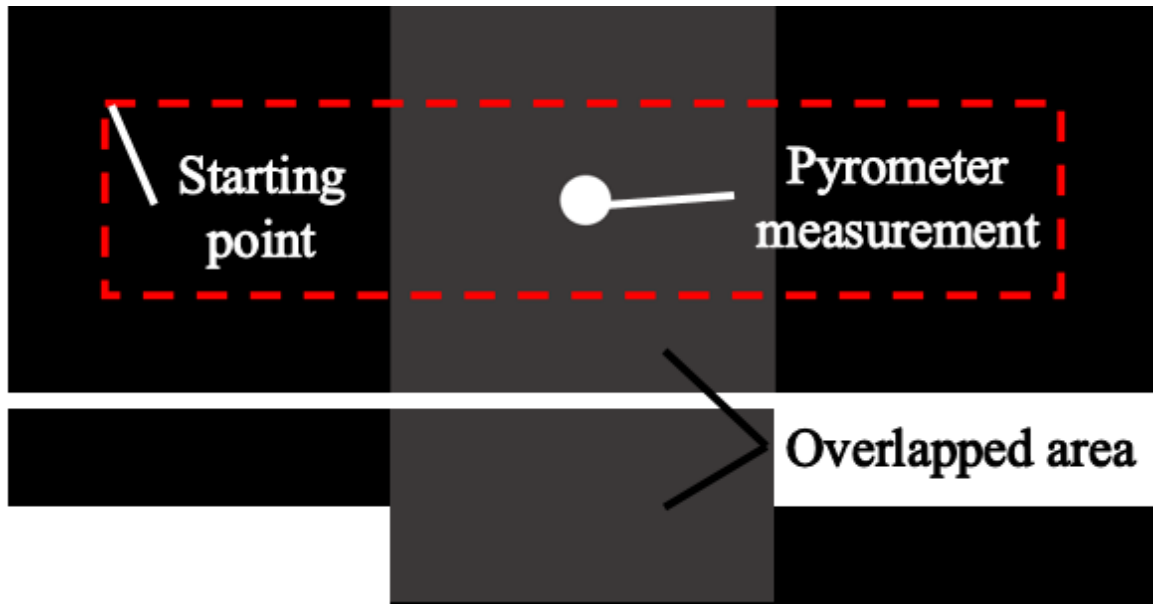


Figure 3.8 Top down view of the thermal calibration test geometry for lap joints, with dark gray as the overlapped region, red the beam path, and white the pyrometer measurement point

The thermal calibration tests were performed in air without filler metal present. Beam power was 500W and intensity was  $120 \text{ W/mm}^2$ . Travel speed was one inch per second, and the total raster time was varied. Duplicate thermal tests were done to verify the repeatability of thermal behavior.

Filler metal was prepared by grinding parallel flat surfaces into the sides of the filler metal buttons. This action allowed thin slices to be cut out of the filler metal with a slow-speed saw. Attempting to cut too thin of slices led to catastrophic fracturing, so the sections were mounted with Crystalbond™ and ground to thickness on 180 grit SiC. Thickness varied across an individual foil by as much as 25 microns, so the slices were binned into varying thickness ranges - values are 150 to 200, 200 to 250, and 250 to 300 microns. Once the proper thickness was achieved, the foils were cleaned in ultrasonically agitated acetone for 15 minutes. The last step in the preparation of the filler metal was cutting the samples into half inch by half inch sections with a sharp knife.

The lap joints were prepared in the controlled atmosphere chamber. Maximum oxygen concentration in the Ar atmosphere was measured to be 13 ppm; oxygen was not actively scavenged. The chamber was overpressured so any leaks would release Ar rather than allowing air to get drafted into the chamber. Before sealing the chamber, RB-SiC coupons were placed in

the bottom of the slots. Filler metal was placed and centered on the lower faying surface. Then the top coupon of RB-SiC would be positioned on top of the filler by allowing the far edge to contact the mold first and then adjusting the remaining edge downwards to avoid shifting the filler metal. Dedicated tweezers and tongs positioned the substrates and braze to prevent contamination. The level of the fixtures was checked before and after loading the pieces. Table 3.2 shows a table summarizing the parameters for lap joint testing.

Table 3.2 Lap Joint Testing Parameters

| Sample Number | Power (W) | Secondary Raster Time<br>(s) | Average Foil Thickness ( $\mu\text{m}$ ) |
|---------------|-----------|------------------------------|--|
| 1             | 500       | 60                           | 225                                      |
| 2             | 500       | 60                           | 275                                      |
| 3             | 500       | 90                           | 275                                      |
| 4             | 500       | 120                          | 275                                      |
| 5             | 500       | 180                          | 275                                      |
| 6             | 500       | 180                          | Cuboid in Middle                         |
| 7             | 500       | 180                          | 175                                      |
| 8             | 500       | 180                          | 225                                      |
| 9             | 500       | 180                          | 275                                      |
| 10            | 500       | 120                          | 275                                      |
| 11            | 500       | 180                          | 275                                      |
| 12            | 400       | 180                          | 275                                      |
| 13            | 600       | 180                          | 275                                      |
| 14            | 400       | 180                          | 225                                      |
| 15            | 600       | 120                          | 275                                      |
| 16            | 500       | 120                          | 225                                      |
| 17            | 500       | 90                           | 225                                      |
| 18            | 500       | 180                          | 225                                      |
| 19            | 600       | 180                          | 225                                      |
| 20            | 400       | 120                          | 225                                      |

Table 3.2 Continued

|    |     |     |     |
|----|-----|-----|-----|
| 21 | 600 | 120 | 225 |
| 22 | 600 | 90  | 225 |
| 23 | 500 | 90  | 225 |
| 24 | 500 | 180 | 225 |
| 25 | 400 | 180 | 225 |
| 26 | 500 | 120 | 275 |
| 27 | 600 | 180 | 275 |

The raster pattern for preheating, beam diameter, and pyrometer measurement spot were the same as in the thermal calibration tests done for the silica shells. Beam power for preheating varied between experiments. Unlike preheating in wettability testing, the preheat for lap joints caused melting in the filler. There was a secondary raster for the lap joints as in wettability testing. Beam parameters for the secondary raster were different between tests, but identical to the preheat beam parameters within a sample. The secondary raster was aimed at the surface directly above the faying surface. Wettability tests had small amounts of laser radiation impinging on the filler metal, but the lap joints did not because these areas were covered entirely by the substrate. Figure 3.9 shows the path of the secondary raster for lap joints to scale in orange.

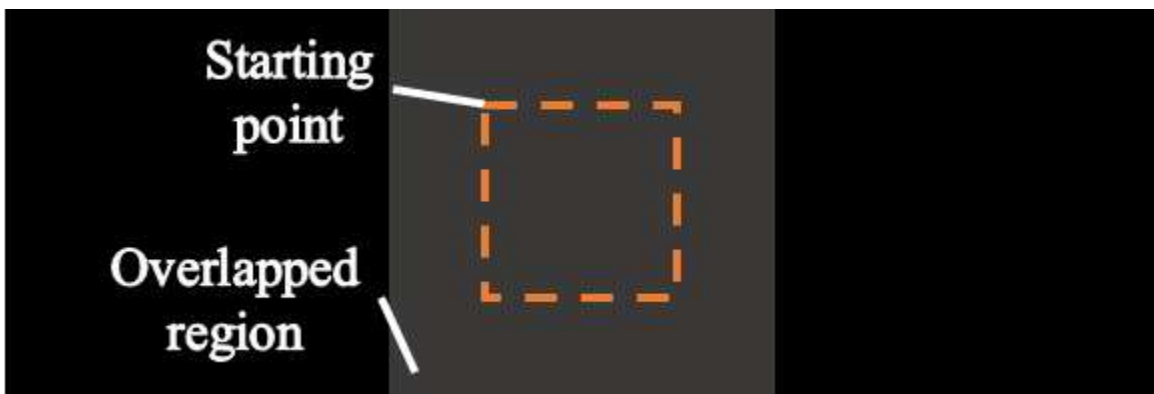


Figure 3.9 To-scale image of the path taken by the secondary raster in orange

In most of the joints, filler metal was observed to flow out of the gap and solidified on the outside of the joint. To record the overflow that was unique to each sample, every sample was

imaged with a light optical stereoscope. Every surface of each sample was captured except for the surfaces on the edges away from the joint. Selected samples were also examined using scanning electron microscopy, primarily in the backscatter mode, to examine the overflow features and other features of interest on the surface. Energy dispersive spectroscopy identified which elements were present in the overflow features.

All the joints were then sheared to failure. Shear force was applied parallel to the long axis of the assembly. The aluminum fixture used in the shearing process was machined in house. Crosshead displacement speed was 0.5 mm/min. Some samples experienced failure in the RB-SiC with the bond remaining intact. Samples that had fractured in the substrate but were able to remain in place in the fixture were loaded again until fracture occurred in a manner preventing them from being held. The overflow features on many of the samples also made setting the samples in the fixture difficult. Pockets were added to the fixtures to account for the overflows, but sometimes samples were still unable to be loaded in the fixture. In these cases, the overflow features were broken off just enough to allow for mechanical testing; if the removal of excess material was not needed, the overflows were left attached to the samples. The mechanical testing fixture with a sample loaded and two samples outside are shown in Figure 3.10.

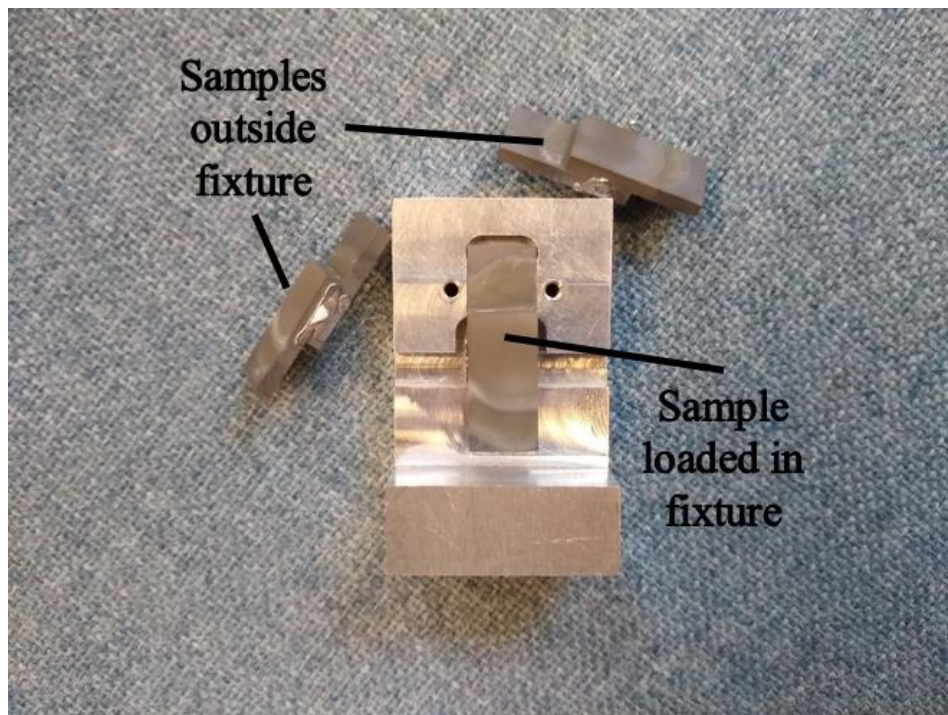


Figure 3.10 Mechanical testing fixture with example samples

The fracture surface was imaged with a light optical stereoscope and selected fracture surfaces were imaged with scanning electron microscopy. Analysis of elemental distribution was performed via energy dispersive spectroscopy and backscattered electron imaging. Area fraction for elements was computed using energy dispersive spectroscopy maps and thresholding in ImageJ.

One test was done with a cuboid of filler metal having the same weight as a foil in the 250 to 300-micron thickness range. The filler metal was placed in the middle of the faying surface of the bottom piece. Owing to the increased thickness relative to the fillers, the top piece of RB-SiC was at an angle. This procedure was not repeated because of the erratic behavior of the filler metal.

Preliminary test runs for lap joints gave early data about parameter ranges. These tests partially bonded the filler metal to the RB-SiC on the upper piece, as the upper portion experienced higher temperatures than the lower piece in pre-steady state situations since the upper piece received direct laser irradiation during the secondary raster. These tests only caused partial bonding since beam power was too low, as beam parameters were copied over from the wettability tests without adjusting for the increased volume of material. The bonding failure motivated the redo of the thermal calibration for lap joints. Only the limited runs of preliminary tests had too low of a power to fully melt the filler metal; all other tests experienced complete melting.

Chapter 4  
CHAPTER 4: RESULTS & DISCUSSION

This section will present the experimental results obtained and their implications, particularly regarding the braze filler metal overflow problem. The thermodynamic behavior of competitive oxidation of the alloying elements in the filler metal will be discussed. The effect of impurity on the strength of the oxide skin and silicon loss will also be elucidated.

Four main conclusions arise and are summarized here to help guide the reader. They are: developing the ability to laser process ceramics with the CSM system, the effect of oxidation and oxide layers, mechanisms leading to oxide layer breakthrough, and extensive diffusion.

#### **4.1 Beam Diameter Calibration**

As discussed earlier, defocusing of the beam is needed to prevent damage to the RB-SiC substrate and knowing the beam diameter at a given focal position is critical to the control of defocusing. Beam diameter at a given distance was found by irradiating 50 micron-thick Kapton™ film taped to firebrick at differing focal distances. Hole diameters were measured with a light optical stereoscope. At larger beam diameters the holes would cause the film to warp, preventing the film from lying flat, which made focusing for imaging more difficult. However, using two lines in a “+” shape through the center of the hole and averaging their lengths was enough to attain reliable and repeatable measurements. The diameter of the holes as a function of height below the focal plane is shown in Figure 4.1.

Beam diameter varied linearly and monotonically with focal distance, except in the region very close the focal point. This condition indicates the above graph is not representative of the actual beam diameter. Power varies linearly with hole diameter until the non-linear region of the plot is reached. Hole width also begins to decrease past a certain point which comes later for the higher power measurements. This phenomenon is caused by the decrease in beam intensity preventing the formation of holes in the Kapton™ as beam width increased. The beam does not abruptly stop making holes because intensity changes throughout the cross-section of a laser beam; power in a laser beam follows a Gaussian distribution, so the edges of the beam will stop creating holes before the middle.

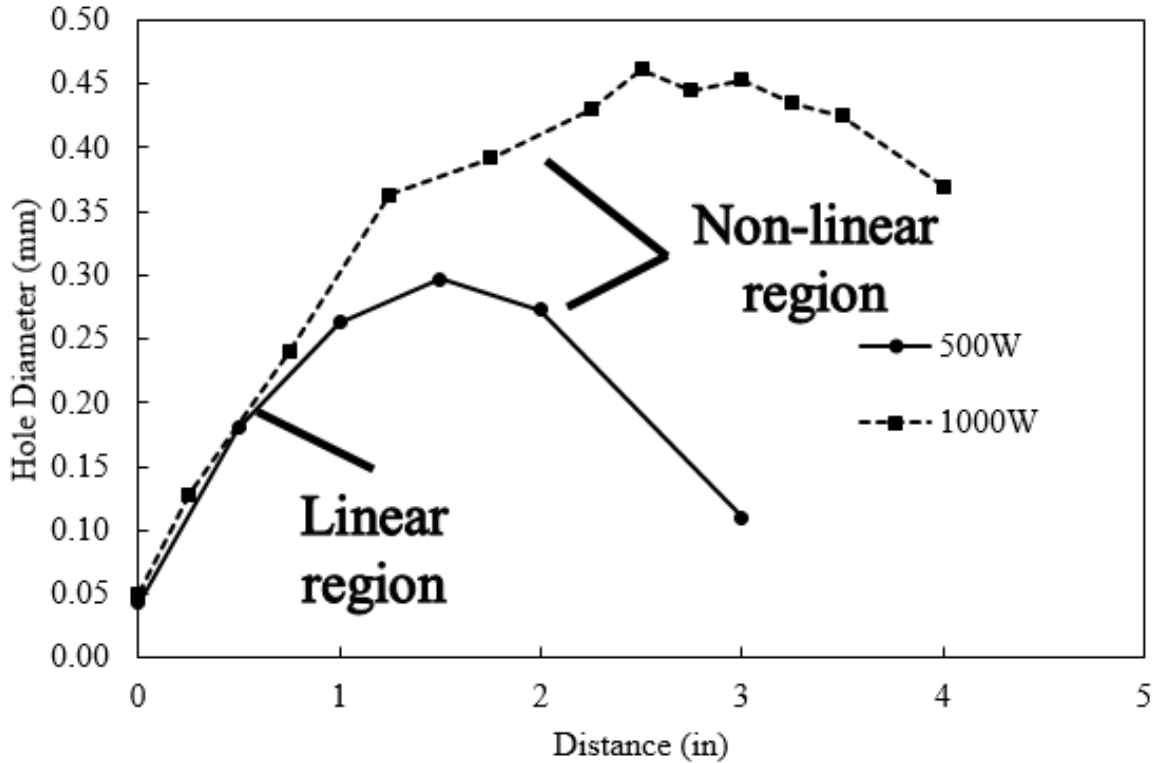


Figure 4.1 Hole diameter in Kapton™ film versus focal distance

To avoid using data points at larger beam diameters that are invalid, analysis was restricted to data from the linear region. Values for beam diameter beyond this range were extrapolated according to a linear relationship. The 500 and 1000 W holes were grouped together for the extrapolation because the differences in beam diameter between the two were minimal. Equation 4.1 shows the linear regression equation for extrapolating the beam diameter, and Figure 4.2 shows the region of data used in the regression analysis for determining Equation 4.1.

$$W(\text{mm}) = \left( \frac{D(\text{in.})}{4} \right) + 0.052 \quad (4.1)$$

In this equation, D is the distance from the focal plane in inches and W is the beam width in mm. The unit conversion is pre-factored into the equation. The coefficient of regression,  $R^2$ , for the hole diameter data is 0.99.

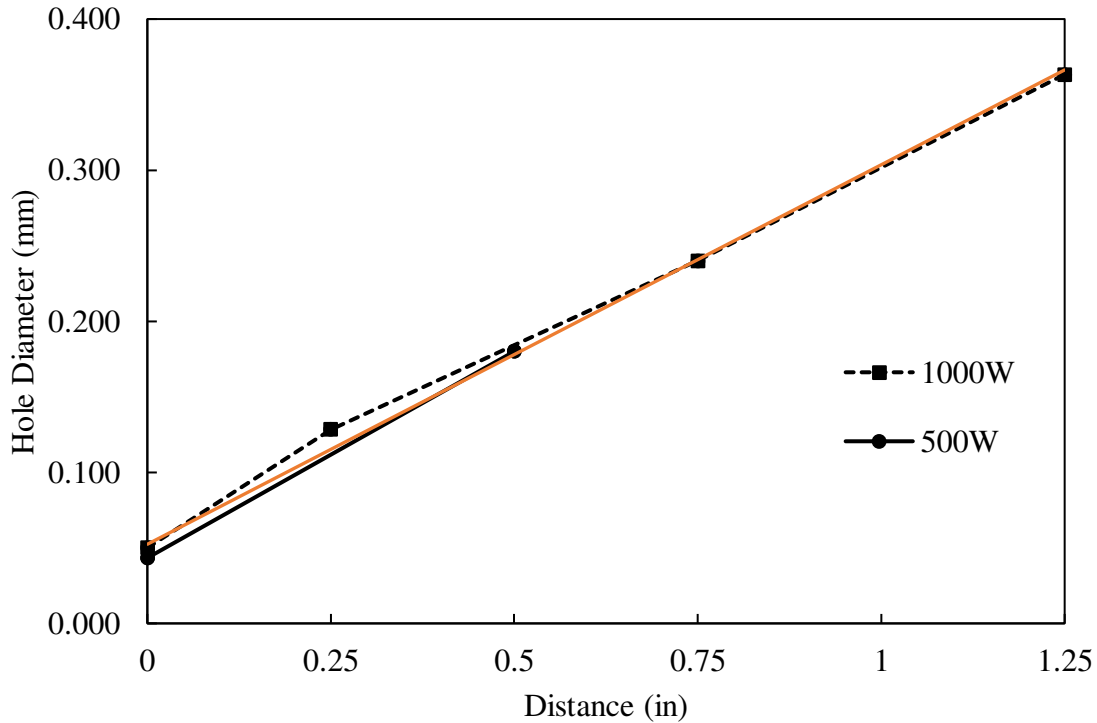


Figure 4.2 Hole diameter used to measure beam width as a function of distance from the focal plane, with the orange line showing the linear regression extrapolated values.

The linear regression generated beam diameter values were used to control the distance setting of the laser head throughout the rest of the experiments.

## 4.2 Preheating

The steady-state temperature of a system is the temperature where heat flux out of the system is equal to heat flux into the system. The determination of steady-state condition is simple for an environment such as a furnace; the heat fluxes are equal when the temperature of the material being treated in the furnace is equal to the temperature of the ambient in the furnace. Put simply, the steady-state temperature of material placed in an open furnace is the temperature of the air inside the furnace.

Unfortunately, the same consideration about steady-state temperature in furnaces does not apply to laser processing. Lasers supply heat directly to the material they impinge upon. Heat then flows out of the material by a mixture of conduction, convection, and radiation. As the RB-SiC was held in place by an insulating material, conduction losses can be neglected. Radiative heat transfer rate is quartic according to the Stefan-Boltzmann Law. Convective heat transfer is

more complicated and may take on a variety of mathematical functionalities, e.g. convective heat transfer rate may take on polynomial forms with powers less than 4. An overall heat loss rate equation for the laser processing conditions encountered in this work can be described as a polynomial of degree 4 with constants determined by analyzing experimental data.

There were two heat transfer scenarios of interest in this work, namely the wettability tests and the lap joints. While pyrometer temperature measurements were taken for both, the data recorded while the laser beam is active were affected by laser interference. Figure 4.3 shows an example of the data collected when the pyrometer measurement spot and beam target were overlapped once an RB-SiC coupon was placed atop steel. Beam power was 500W, the intensity was 120 W/mm<sup>2</sup>, and pyrometers measured temperature ranges of 100 to 700 and 750 to 2500 °C, respectively.

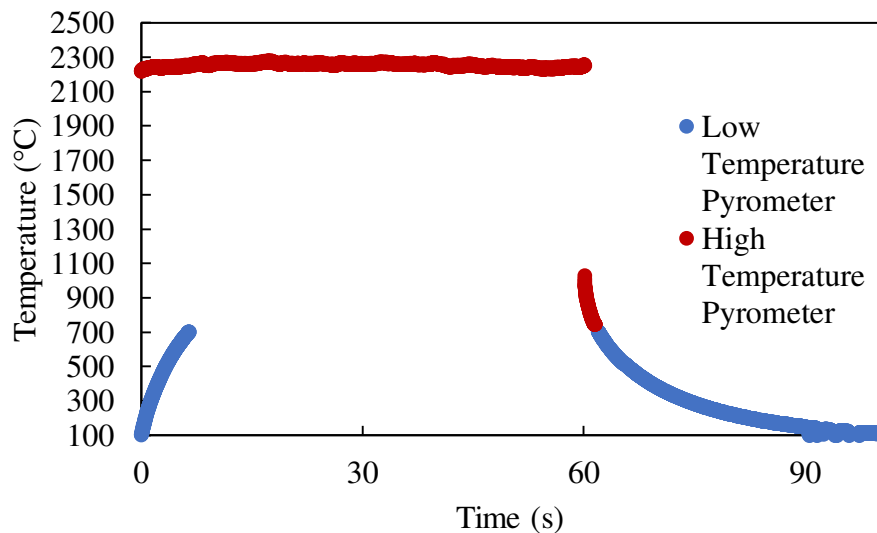


Figure 4.3 Comparison between data collected with 100 to 700 and 750 to 2500 °C pyrometers with beam and pyrometer measurement point overlapping

The data for the high temperature pyrometer is judged invalid because the temperature in the substrate must be continuous and that large of a jump would likely cause fracture by thermal shock. The low temperature pyrometer showed a gradual increase in temperature at heating and tapering off at cooling, as is expected. High temperature pyrometer data read a constant value of around 2245 °C while the beam was on, and then instantaneously dropped to 1031 °C when the beam was turned off. Thermal shock aside, a drop this sudden is unrealistic in the absence of

active cooling systems. The fluctuation and divergence of data from the two pyrometers were observed because of the interference between the laser beam and the high temperature pyrometer during measurement. The distribution of wavelengths emitted by a hot body roughly depends on its temperature according to Wien's approximation as written in Equation 4.2,

$$\lambda_{\max} = b/T \quad (4.2)$$

where  $\lambda_{\max}$  is the peak wavelength of the distribution, T is absolute temperature, and b is a constant equal to 2900  $\mu\text{m}\cdot\text{K}$ . Pyrometers measure temperature by measuring the peak wavelength a hot body gives off. Since the instrument cannot detect which is the source of radiation, a source of light brighter than the actual signal will override the measurements. A quick calculation with Wien's approximation shows the wavelength corresponding to 2245 °C is 1.15  $\mu\text{m}$ , or 1150 nm, which is close to the wavelength of the laser in this study of 1070 nm. Interference between the two readings is likely the cause of such erratic readings. The small difference of 80 nm, or 7.5%, is not enough to disconfirm the laser interfering with temperature measurements because Wien's approximation is not fully accurate. Furthermore, no interference is seen with the low temperature pyrometer which does not register photons with wavelengths shorter than about 3 nm. An attempt was made to block the signal from the laser, but the laser reflections are much brighter than the pyrometer signals.

Fortunately, the temperature immediately after the beam is shut off is functionally equal to the temperature immediately before the beam is shut off. Measuring temperature while the beam is on is mostly useful for measuring the time it takes to achieve steady-state temperature; the value of steady-state temperature itself can be taken right when the beam shuts off. Steady-state temperature is paramount in the analysis of steady-state heat loss rates as a function of temperature. Heat flux into the system is defined by multiplying the power of the laser beam with the absorptivity of the substrate. Absorptivity changes as a function of wavelength and temperature. Lasers are monochromatic, so only absorptivity dependency on temperature needs to be considered. The absorptivity of silicon carbide at 1064 nm, the wavelength of Nd:YAG lasers, is relatively constant with temperature. Figure 4.4 shows the change in absorptivity of silicon carbide with temperature at 1064 nm, which is close to 1070 nm of the Yb-fiber laser in the present case [3].

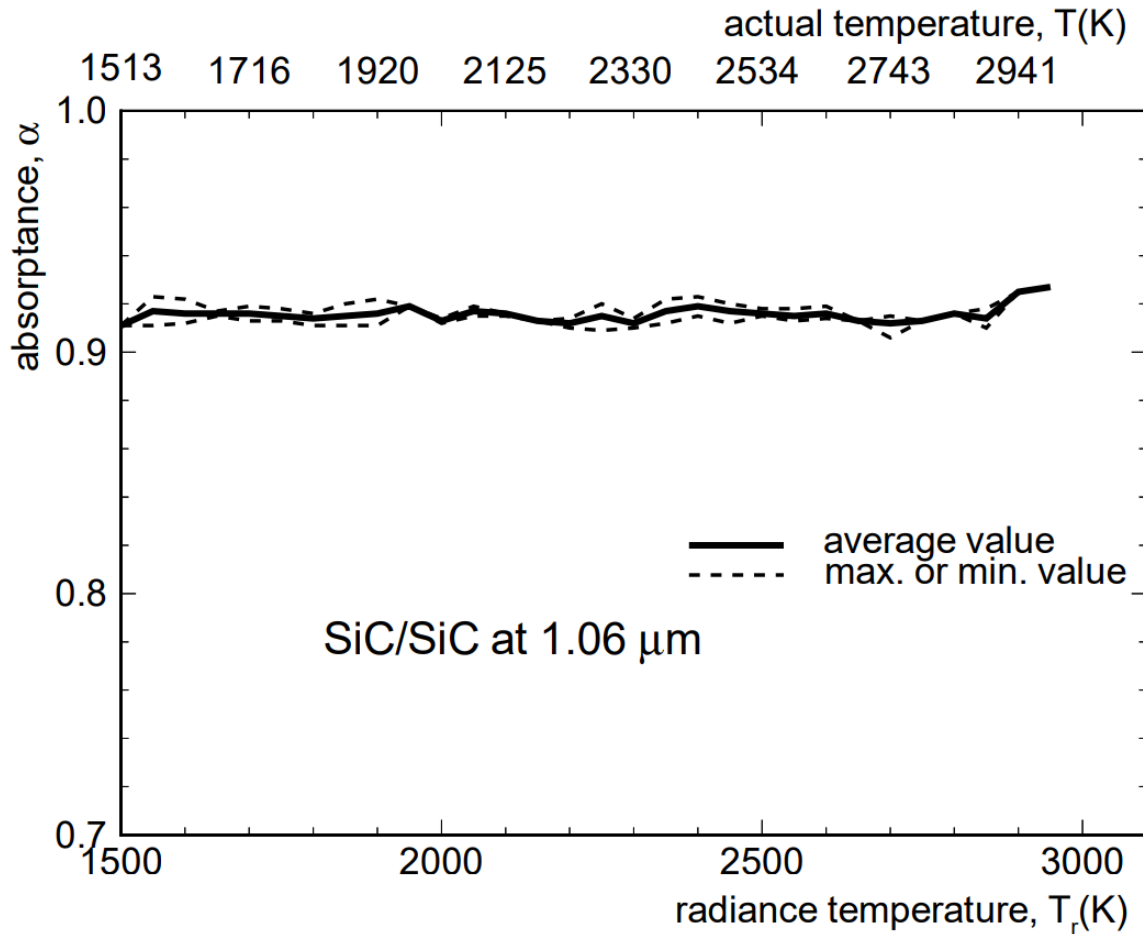


Figure 4.4 Changes in absorptivity with temperature at 1064 nm for silicon carbide [3]

A relatively constant absorptivity with temperature allows the heat input to be considered constant. Heat output is then the only variable determining achievable temperatures. Since pyrometer data were recorded for all samples in addition to the pyrometer data recorded during preheat testing, the equation describing steady-state temperature as a function of laser power can be found.

#### 4.2.1 Heat Transfer in Wettability Testing

Laser power is not the only variable changed though, so the equation also depends on the geometry of the RB-SiC being heated, the fixture material and how it is holding the substrate, and the raster pattern itself. The raster patterns for preheating affect the entire sample, but the rasters for secondary heating focus more heat toward the region where the filler metal would be melted, creating a hotter middle and cooler outside. The quantity of filler metal has an effect as well by increasing the area for heat losses and slowing cooling and heating because of the added

thermal mass. Phase changes, especially melting and solidification, also have their own enthalpy requirements that amplify this effect. Therefore, the preheating experiments done without filler present most readily show the steady-state temperatures achieved by laser heating. Figure 4.5 shows the temperatures reached after the laser was shut off after achieving steady-state temperature by rastering according to the pattern shown in Figure 3.2 on firebrick backing.

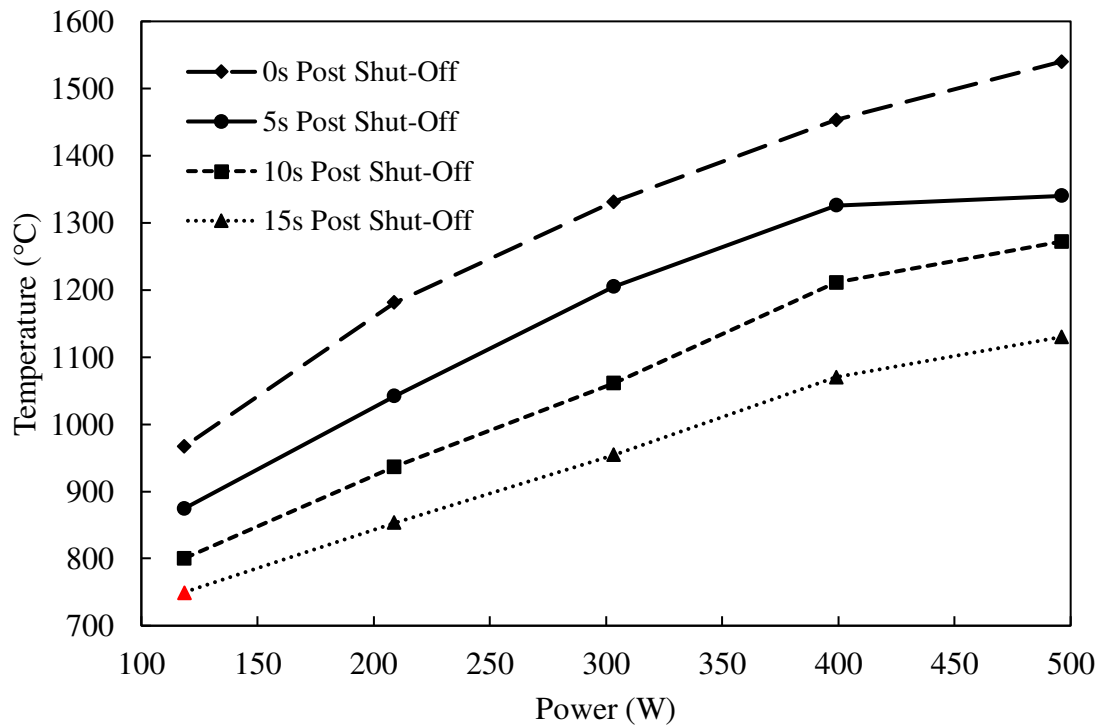


Figure 4.5 Temperature recorded by pyrometer for different times after beam shut-off when rastering over single coupon atop firebrick, only one reading per point due to consistent behavior

The data point highlighted in red is questionable because it is exactly 750 °C, the lowest temperature measurable with this pyrometer. Another data point of note is the five second post shut-off point after the 500 W raster. This sample did not follow the trend of the other data points - the value is lower. Examination of the cooling curves shown in Figure 4.6 after the laser is shut off explains why this data point does not follow the trend.

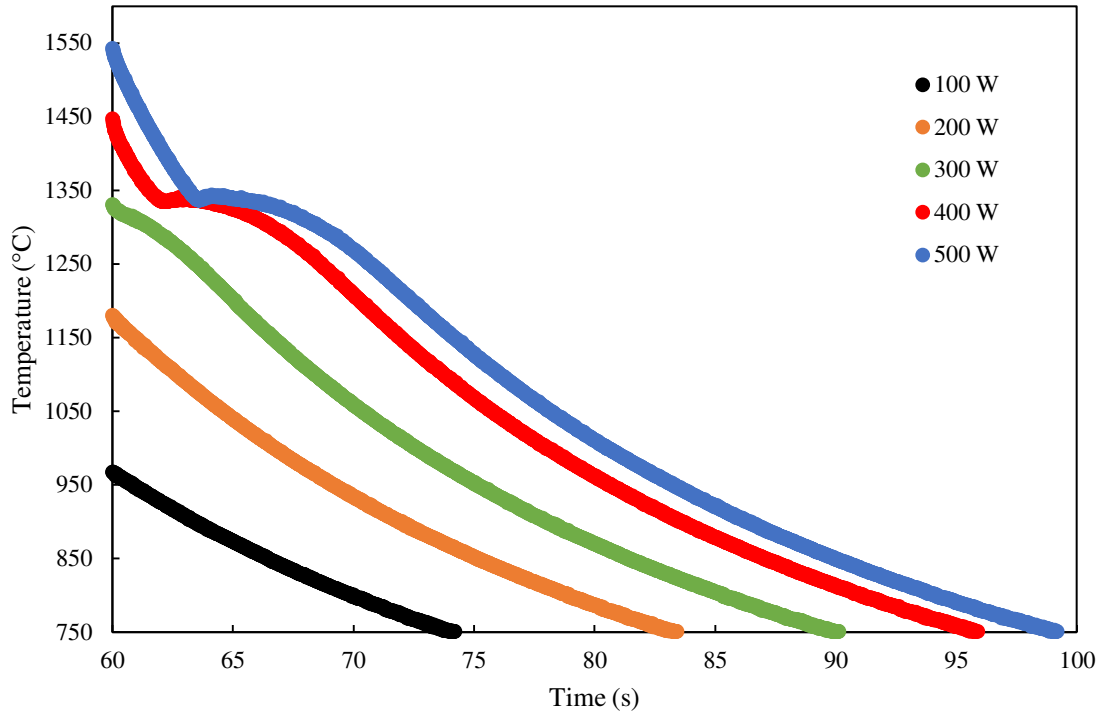


Figure 4.6 Cooling curves after the laser beam is shut off for different powers

Both the 400 and 500 W curves clearly exhibited an inflection point at 62 and 63 s after the laser beam was shut off, respectively. The 300 W curve showed a slight sign of inflection at 60 s. All three of the inflection points occurred at approximately 1340 °C, indicating the onset of solidification. Release of heat of fusion temporarily halted cooling creating undercooling. This cessation of cooling is caused by the solidification of free Si in the RB-SiC. Pure Si melts at 1414 °C, but the free Si in RB-SiC is alloyed with impurities due to the SiC synthesis process that would lower the melting temperature. Typical cooling curves look like the 100 and 200 W curves, which do not see melting because they do not exceed the melting point of Si at 967 and 1176 °C, respectively (Figure 4.6).

Since the steady-state heat transfer scenario assumptions do not account for the enthalpy from solidification, only data from before the onset of solidification can be analyzed. From this information, Equation 4.3 can be constructed.

$$Q_{\text{loss,wet}} = 47\text{E-}12 * T_{\text{abs}}^4 \quad (4.3)$$

In this equation,  $Q_{\text{loss,wet}}$  is the heat loss rate for the wettability testing scenario in units of Watts. Information specific to this scenario is contained in the constant before absolute temperature. Analysis below reveals convective heat losses are minor compared to radiative at the temperatures in these experiments. The regression to find this equation had an intercept near zero but was forced to have an intercept at zero to be more accurate. As this equation only accounts for radiative heat losses, it would be inaccurate for lower temperatures. This limitation is not a concern because temperatures low enough for this equation to be invalid were not encountered in any of the work performed since filler material needed to be melted.

#### 4.2.2 Heat Transfer in Lap Joints

Equation 4.3 only applies to the exact scenario encountered in wettability testing. Changing the fixture material holding the RB-SiC or changing surface area will both alter the coefficient. Also, preheat rasters for lap joints were twice the duration of those done for wettability tests, taking 120 seconds and using powers of 400 to 600 W. Developing an expression like Equation 4.3 is essentially through plotting temperature as a function of power, i.e.  $T^4$  versus power. The slope of the line made in this plot is then the coefficient in Equation 4.3. Note the independent axis is on the vertical axis instead of the conventional horizontal axis to simplify the mathematics of regression. This plot is given in Figure 4.7.

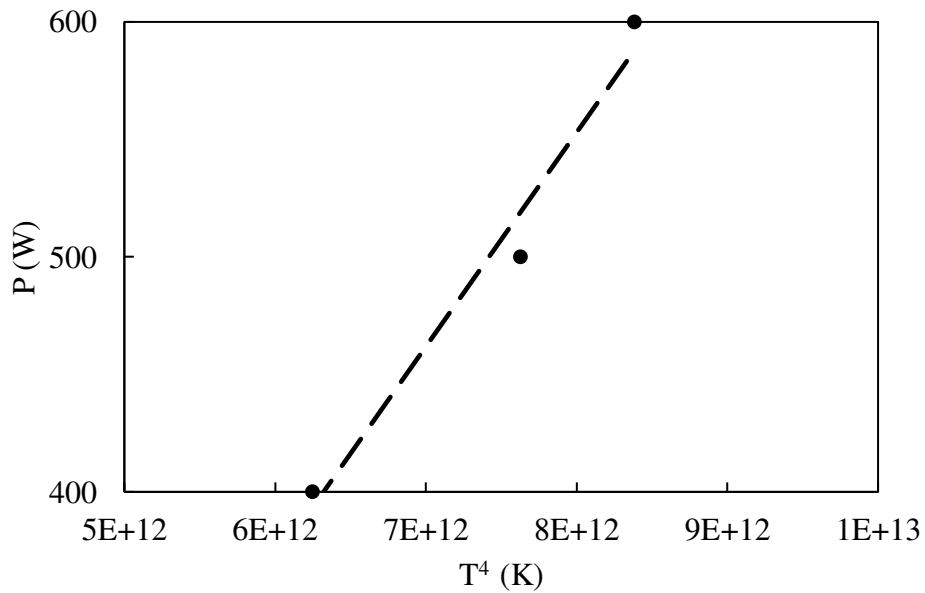


Figure 4.7 Plot used to find Equation 4.3

Equation 4.3 has a higher coefficient because the total area is larger in the lap joint testing, increasing the rate of heat loss. For the same reason, higher powers would be required for the lap joint experiments. In practice, thermal calibration similar to that described here must be conducted for laser brazing for every geometry. Fortunately, this calibration requires only a simple setup and a small number of tests. Joining large size components that could act as a heat sink would require semi-infinite assumptions. In that case, one geometry can be representative of thermal calibration for many others. Modeling the heat transfer may solve this issue instead of having to redo thermal calibration for new geometries. Using insulating materials such as firebrick and silica also aid in reducing the total energy consumption of the process.

Because the silica fixtures made to hold lap joints contained multiple slots, each slot was verified in the following as having identical thermal performance. To ensure uniform thermal performance and balance, two RB-SiC coupons were placed into the slots in the same configuration as they would be for making a lap joint but without the insertion of filler metal. Placement of the pyrometer beam and the raster pattern were identical to how they would be for lap joint creation. Raster time was only 60 seconds instead of the 120 seconds used for brazing preheats. Beam parameters were 500 W with 120 W/mm<sup>2</sup> intensity. Figure 4.8 shows the results of the test.

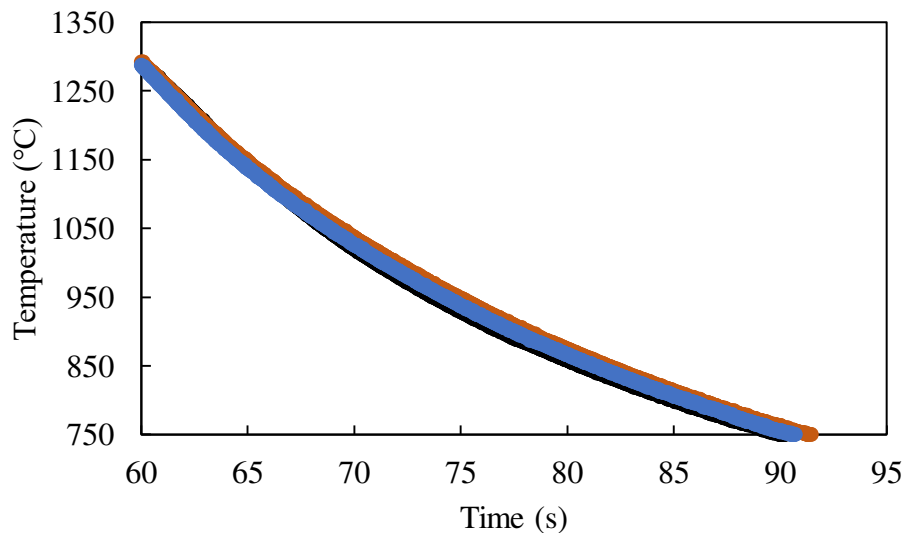


Figure 4.8 Comparison of thermal behavior between different silica fixture slots to ensure consistent behavior

Figure 4.8 expresses how the thermal behavior between the slots is consistent enough to treat each slot interchangeably. This result is expected since the slots are all thermal insulators, so the only significant heat transfer mechanism is radiation. Loading material to be joined in different slots would not change how quickly a material radiates away heat; only the innate emissivity of the material, exposed surface area, and temperature affect radiative heat transfer.

### 4.3 Laser and Thermal Effects on the Substrate

Reaction-bonded silicon carbide can operate at high temperatures, but not necessarily at the extreme temperatures involved in laser brazing. Regions directly under the laser beam or immediately adjacent to the laser spot experience locally extreme temperatures so some damage on the RB-SiC surface would be expected.

The most severe type of damage possible is fracture and cracking. Reaction-bonded silicon carbide has a higher thermal diffusivity than steel and many metals but does not have as high of a fracture toughness. Therefore, the rapid heating of a small region will cause localized thermal expansion, leading to localized strain and possibly fracture. If the strain energy is not too great a crack may grow, then arrest as predicted by linear elastic fracture mechanics (LEFM). A focused beam should not be used to heat RB-SiC because the beam will simply cause fracture through localized heating. High travel speeds may be deployed to avoid this phenomenon by spreading out the energy delivered and thus avoiding high thermal gradients which could cause fracture. However, defocusing is much easier. Figure 4.9 shows the fracture surface of a sample heated with a focused beam.

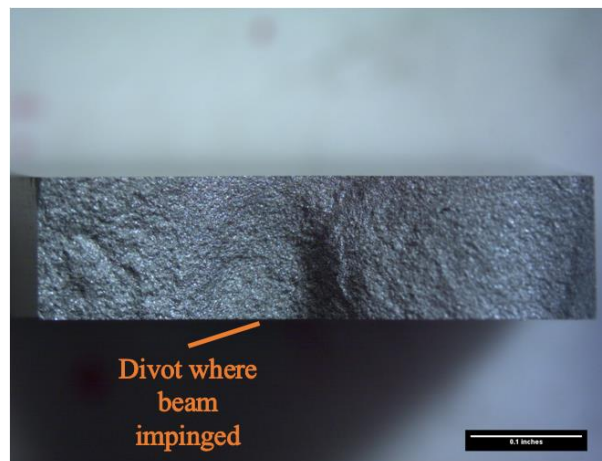


Figure 4.9 The results of a focused beam impinging on a RB-SiC coupon

A visible divot in the middle of the sample in the region underneath where the beam impinged as represented by the shadowed area is further proof of the effects of a focused beam on a RB-SiC coupon. While fracture did occur in this test, focused radiation does not always cause failure. At low enough intensities or short enough exposure time RB-SiC can survive laser radiation. Lower intensity and shorter exposure time both address the same cause of fracture, namely severe thermal gradients creating strain gradients. To find the space of beam intensity that would be safe for the RB-SiC in this study, a set of iterative experiments in which RB-SiC was exposed to laser radiation of decreasing intensity with short pulses was conducted. If light optical stereoscopy of the samples did not reveal signs of cracking or surface gouging, then the exposure time would be increased. The first intensity to reach one minute of exposure without damage was declared the maximum safe intensity moving forward. This experiment was performed in open air with a steel backing because excess radiation after fracture would damage a ceramic backing. These data are shown in Table 4.1.

Table 4.1: Intensity and exposure time results used to evaluate the intensity needed to avoid fracture

| <b>Intensity (W/mm<sup>2</sup>)</b> | <b>Exposure Time (ms)</b> | <b>Result</b> |
|-------------------------------------|---------------------------|---------------|
| 233,000                             | 100                       | Damaged       |
| 112,000                             | 50                        | Damaged       |
| 978                                 | 100                       | Undamaged     |
| 978                                 | 500                       | Undamaged     |
| 978                                 | 2,500                     | Fractured     |
| 740                                 | 2,000                     | Fractured     |
| 520                                 | 5,000                     | Fractured     |
| 261                                 | 2,500                     | Undamaged     |
| 261                                 | 10,000                    | Undamaged     |
| 261                                 | 25,000                    | Undamaged     |
| 261                                 | 60,000                    | Undamaged     |

### 4.3.1 Surface Texturing

A focused beam with short exposure time can also be used for machining multiple varieties of ceramics [56]. In this work, a short experiment to create surfaces with a grid of laser ablation and texturing was conducted. The laser was focused and struck the sample in a regular square grid with ten thousandths of an inch spacing. A single pulse impinged at each point, lasting one millisecond in open air. Power varied from 100 to 1000 Watts in 100 W increments, with one extra data point done at 50 W. Light optical stereoscope images of the resultant surfaces are shown in Figure 4.10.

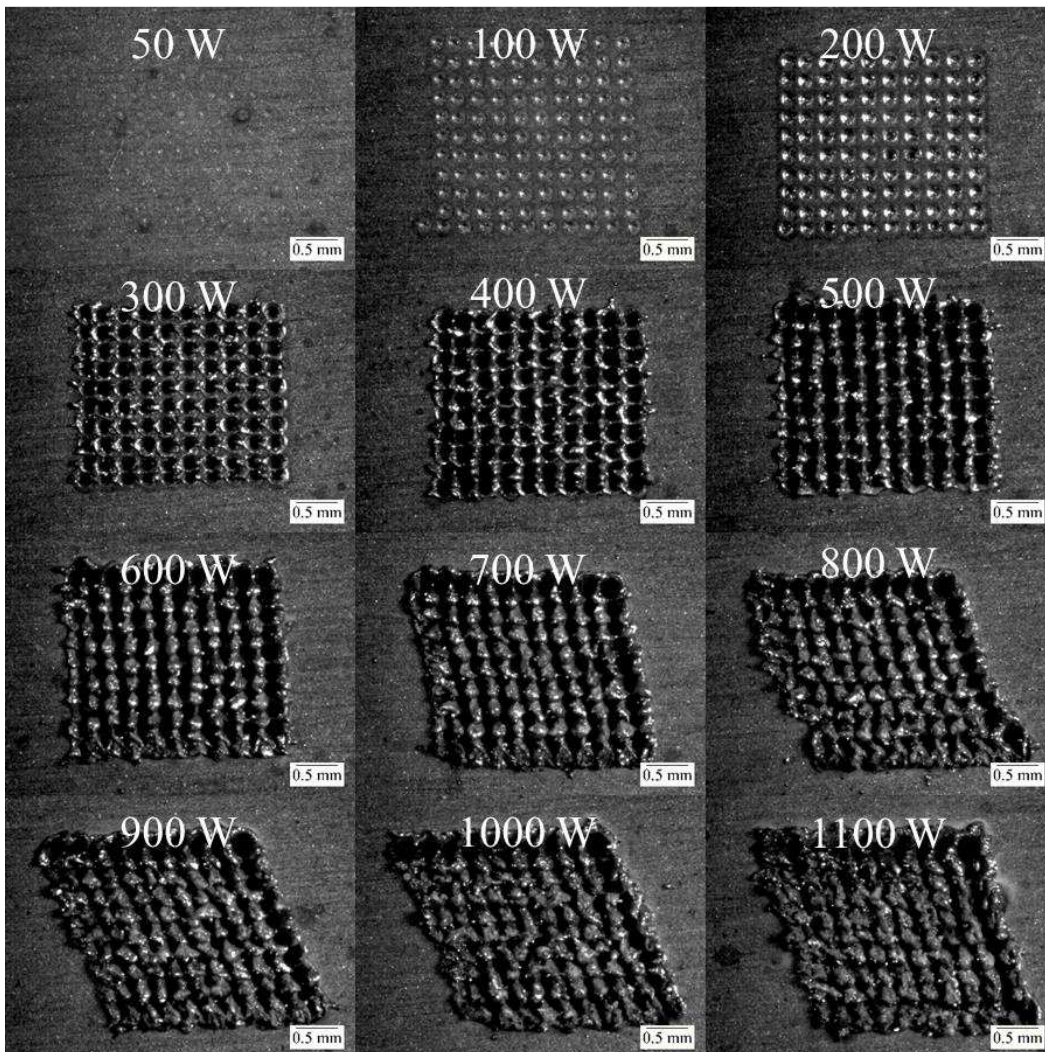


Figure 4.10 Results of laser ablation on RB-SiC surface in grid with varying power; distortion in grid (700 to 1100 W) from CNC issues

Perturbations from a square grid were caused by issues with the CNC computer. These grids effectively express three key results: RB-SiC fracture from a focused beam is caused by the resultant thermal gradients and not the beam, which causes surface damage. The ability of the beam to damage the surface has applications but this effect is detrimental to joining. Damaging the surface in a controlled manner can create texture or holes for mechanical anchoring of joints. The transition between divots and holes is around 300 W, depending on what aspect ratio is defined as a “divot” versus a “hole”. Surface texture affects wettability, and holes for mechanical anchoring may improve strength [57]. Ablating material with the laser also allows for laser machining, though too high of a laser power or too long of a pulse will lead to issues with oxidation. Ablation is ideally done with extremely short laser pulses, in the range of femtoseconds [58], but the fastest pulse possible with the Yb-fiber laser used in this work is one millisecond. In addition to fracture, surface ablation and texturing, free Si can also melt and flow, leading to irregularity as seen in the 300 to 1100 W samples shown in Figure 4.10. Liquation of Si can be avoided entirely with the reduction of laser powers. RB-SiC is also more susceptible to oxidation than sintered SiC due to the free Si. An oxygen-free atmosphere, a reducing atmosphere, or vacuum are all potential solutions for substrate oxidation. Highly localized loss of material such as that caused by ablation can be avoided entirely by defocusing.

#### **4.3.2 Surface Damage Mechanisms**

Thermal damage to RB-SiC is primarily a result of oxidation and material loss. Both were examined by impinging the laser beam on the substrate surface for 60 seconds in open air with a firebrick backing. The beam was either rastered according to the pattern in Figure 3.2 or kept static in the center of the flat surface. The pyrometer measurement point was in the geometric center of the sample in both cases. Beam power was 500 W, travel speed for rastering was one inch per second, and intensity was  $120 \text{ W/mm}^2$ .

The static spot sample reached higher temperatures than the rastered sample. A precise value for the difference is unknown because depending on the degree of oxidation on the surface, emissivity changed. Emissivity values for SiC and SiO<sub>2</sub> are different, and emissivity must be known for accurate pyrometer measurement. Observation of the sample during cooling showed the center region of the sample (immediately near the beam) glowing differently than the rest of the sample which confirms the changing emissivity. The temperatures measured by the

pyrometer, without factoring in emissivity changes, were 1820 and 1540 °C, respectively. Actual error in measurement for the severely oxidized surface may not be too large, as the beginning of the solidification bump in the cooling curves only differed by around 40 °C. Either way, the temperatures reached as a result of the laser energy were enough to cause damage to the RB-SiC. Figure 4.11 shows the surface of the sample heated with a static beam spot.

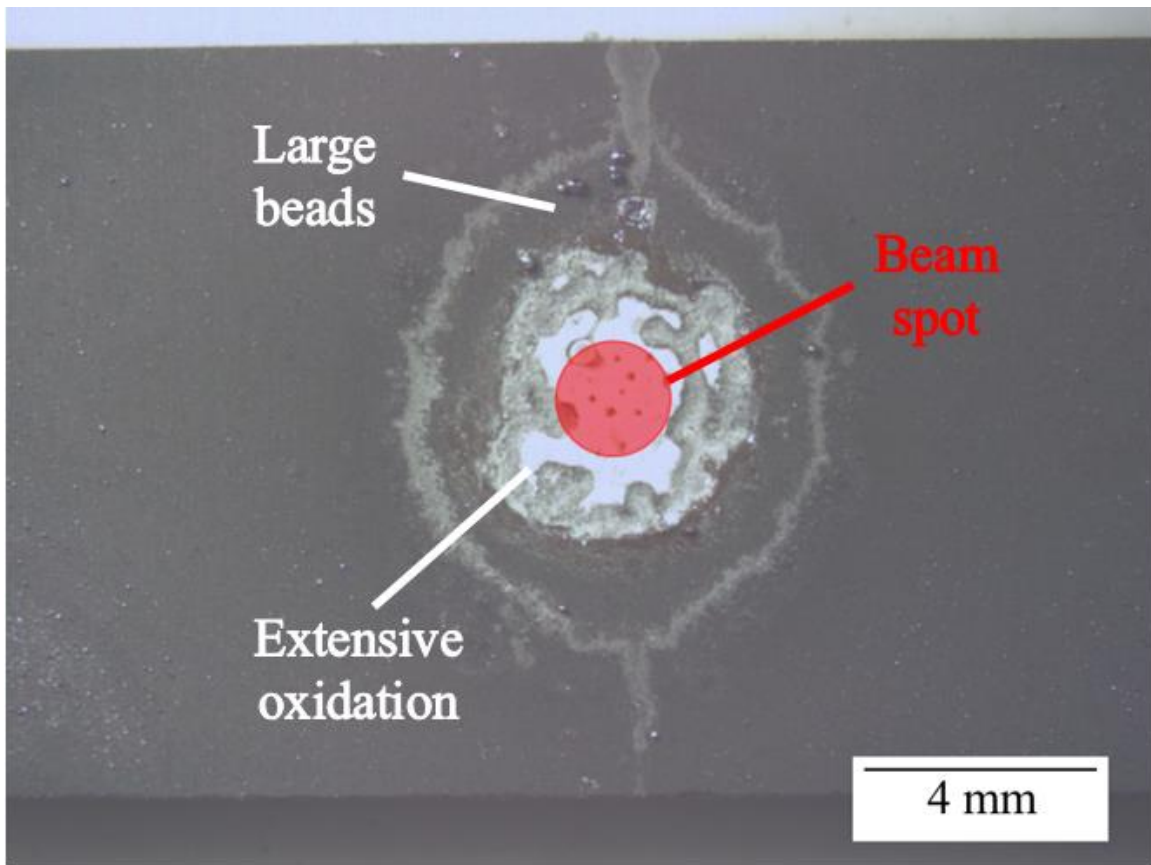


Figure 4.11 Results of oxidation experiment with transparent overlay illustrating beam position and diameter

Figure 4.11 shows extensive oxidation in and around the laser spot and extending beyond the diameter where the beam impinges on the surface. As such, damage from the heat of the laser beam, while local in nature, will be observed outside the laser point of incidence. Gaseous SiO is another possible reaction product when Si is oxidized. The heavily oxidized region is depressed inwards relative to the rest of the surface, indicating material loss, thus SiO formation is highly likely. Observation during the test also showed a plume rising from the sample, lending credence to SiO formation as an explanation. Oxidation is not the only observation made from Figure 4.11; a ring of discoloration is present around the oxidized circle. The ring represents a region of

free silicon loss where the SiC network remains. The remaining SiC is expected to have a reduction in strength compared to fully dense RB-SiC because of the intrinsically high porosity. Surface roughness is also increased for the same reason. Bead-like features attached to the surface are evident near the hotter areas. The size of the beads grew as these get closer to the hot regions. In fact, these beads are present on most of the samples heated with the laser, regardless of whether filler metal was used or not. This observation is a clear indication that the appearance of these beads is a phenomenon intrinsic to the substrate and not the filler metal. Figure 4.12 shows the sample where the beam was rastered instead of being kept static.

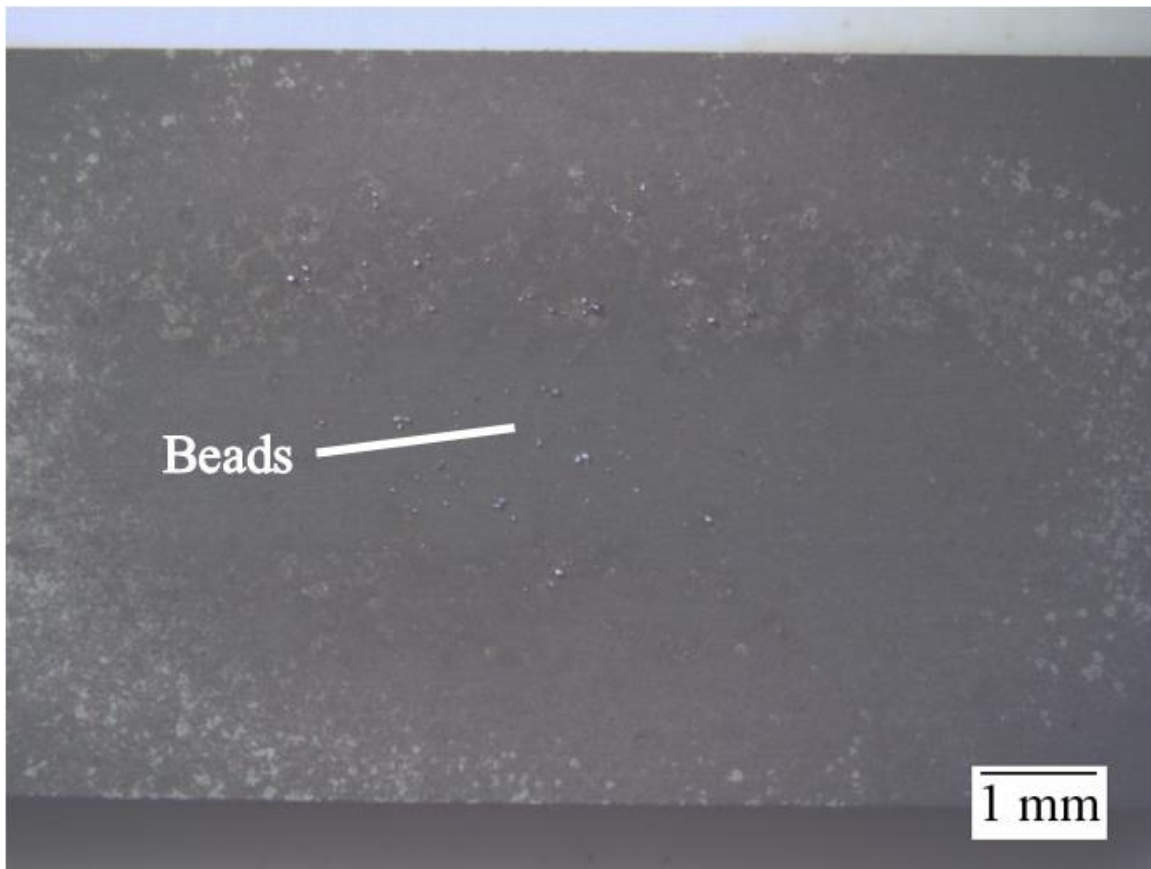


Figure 4.12 RB-SiC sample exposed to rastered beam instead of static beam

Rastering spread the heat imparted by the beam out over a larger area, so the temperature reached was lower. Bead size also decreased, while increasing in number. The increased bead size is a result of beads coalescing, which reduces the total free energy of the beads as described by the Gibbs-Thomson Effect. The beads are mainly comprised of silicon along with the impurities concentrated in the free silicon regions from the RB-SiC synthesis process. They

appear on the surface when the RB-SiC exceeded the melting point of Si, liquefying Si and allowing it to flow to the surface. Flowing to the surface would expose the beads to oxygen, turning the Si on the surface into a SiO<sub>2</sub> skin. Silica does not wet silicon carbide without surface treatment [59], so the beads would have a high contact angle. Higher temperatures would increase bead size because the amount of free Si migrating to the surface increases with temperature and the flowability of molten Si is enhanced with temperature. Neighboring beads will have greater opportunity to coalesce under these conditions.

Figure 4.13 shows energy dispersive spectroscopy scans of a bead imaged on a wettability testing sample reflecting the impurities present.

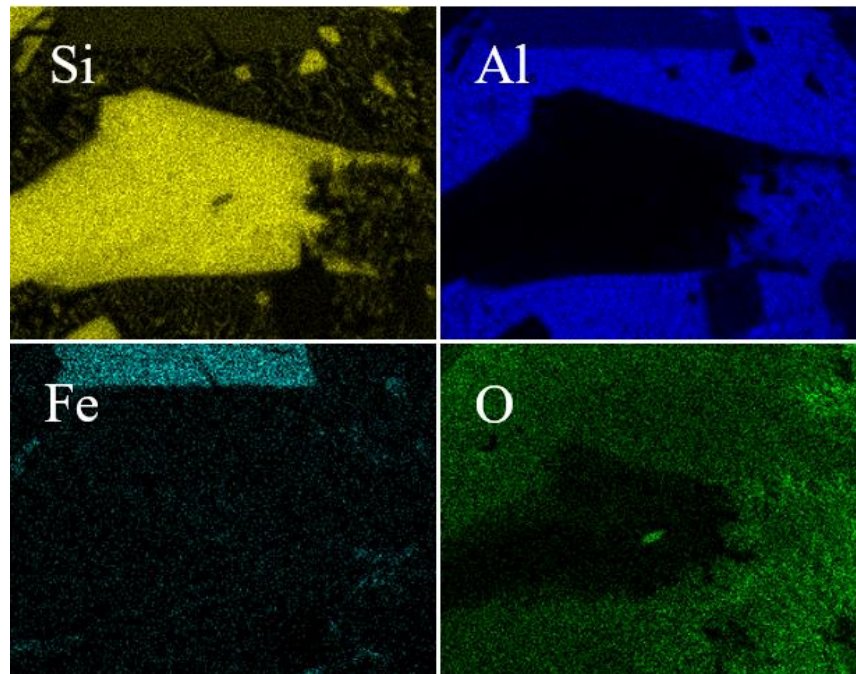


Figure 4.13 EDS scans of bead developed during wettability testing

Aluminum is present because the wettability tests involve filler metal, which contains aluminum. Iron, however, does not originate from the filler metal since high purity elements were used to melt to make the filler metal. The source of iron is the RB-SiC itself. Silicon sourced for the RB-SiC in this work was derived from ferrosilicon, thus the residual iron. Using iron-containing silicon to synthesize RB-SiC concentrated the iron in the last regions of free Si to solidify, which is often the surface. When Si at or near the surface melts and flows to form beads, the iron comes with it. Free Si may also introduce iron into the filler metal itself; the

effect of this introduction will be discussed later. Loss of free Si from the RB-SiC leaves behind SiC as mentioned earlier. Figure 4.14 shows the four different levels of free Si loss encountered with electron backscattered electron imaging.

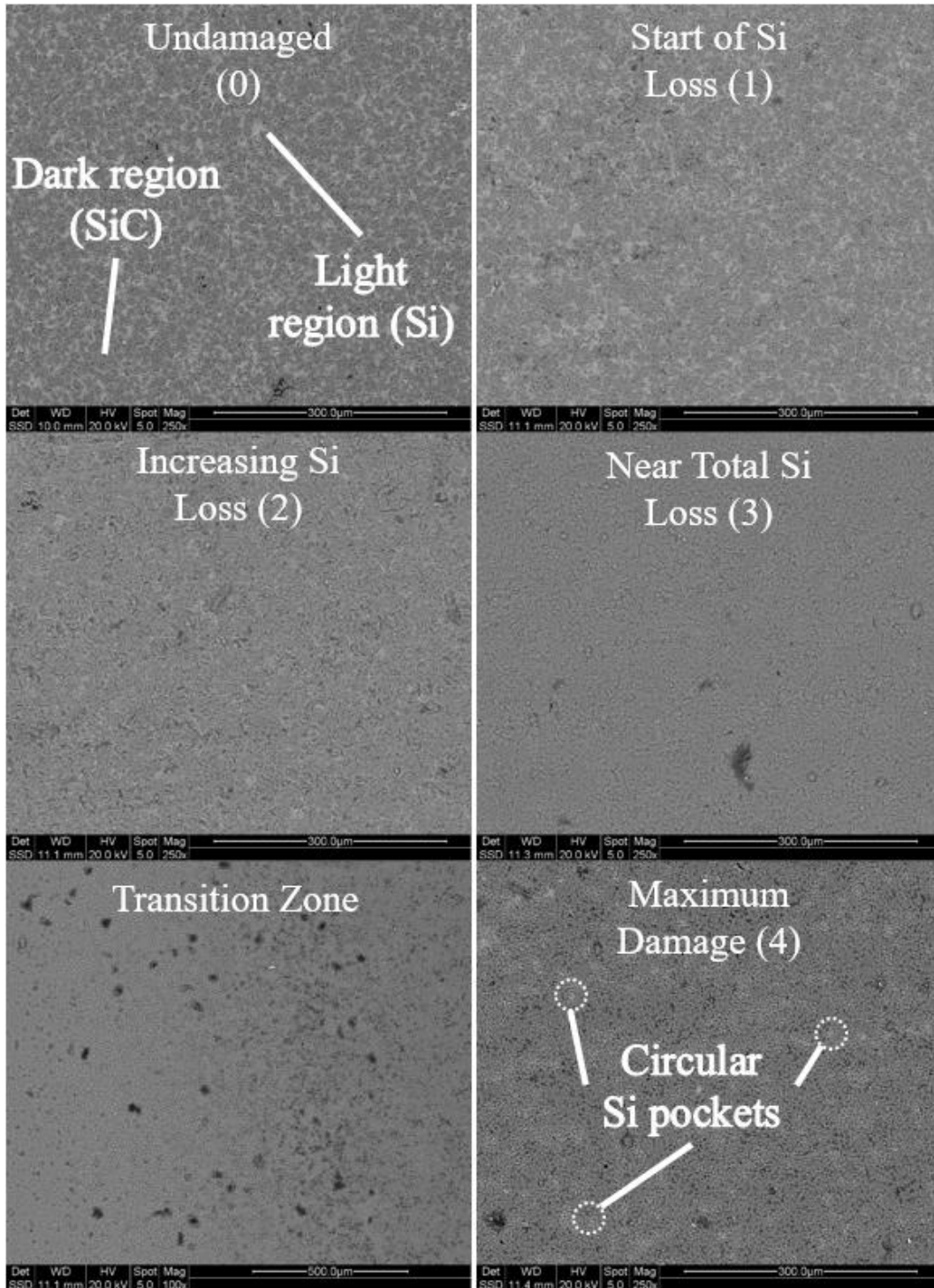


Figure 4.14 Different levels of Si loss and surface damage seen in RB-SiC with zone labels

Note the lower left image is at a different scale than the rest of the images. This scale change is done intentionally to show the transition from zone two to zone four. Zone zero has 40 area% Si (by image analysis), zone one has 34 area% Si, zone two has 26 area% Si, zone three has 20 area% Si, and zone four has 11 area% Si. Zone three is present within the transition zone. The image for zone zero was taken from a RB-SiC coupon never exposed to laser radiation. Backscattered electron imaging is based on atomic number contrast; higher atomic number elements will appear brighter on these images. Iron, though concentrated during RB-SiC synthesis, is not concentrated enough on the surface to be seen at these magnifications. Therefore, the only two elements present should be silicon and carbon. Silicon carbide has a lower average atomic number than Si and should appear darker. Of course, SiC is not an element. In the case of compounds, brightness in backscattered electron imaging comes from the weighted average of the atomic numbers. The darker regions in the image are SiC and the brighter regions are Si. It is noticeable that silicon regions decrease in quantity and thickness with the increasingly damaged zones. Zone four is an exception. In addition to losing Si, the remaining Si has changed morphology into more circular pockets which may be the precursor to surface bead formation. This precursor stage cannot be confirmed without in-situ experimentation.

Surface damage cannot be entirely avoided. Direct damage from the beam can be avoided by defocusing. At low intensities, fracture and cracking are largely a non-concern. Contrarily, thermal damage is not resolved with any amount of defocusing. Laser processing employs shorter times and must, therefore, reach higher temperatures than furnace processing for the active metal reactions to occur in time. High temperatures lead to rapid oxidation unless the atmosphere is extremely clean. Surface material loss to bead formation will naturally occur with RB-SiC once the melting point of Si is exceeded, and losses from SiO formation occur for similar reasons. These occurrences cannot be avoided since the braze must melt. If sintered SiC were joined, instead of RB-SiC, surface material loss would not be a concern because of the absence of a Si network. These damage mechanisms are a result of the temperature and atmosphere rather than the beam itself and will happen regardless of the heat source used.

#### 4.4 Wettability Testing

Good wetting is fundamental to a good braze joint. Testing the wettability of a filler on the material to be joined is conventionally the first step in evaluating the feasibility of a brazing process. The filler alloy composition in this study was originally developed and tested in-house using a vacuum furnace. With even heating throughout the substrate and filler, long process times, and no atmospheric effects, vacuum furnace conditions are almost opposite those of laser conditions. Laser brazing is characterized by uneven heating because the system is not in thermal equilibrium with the surroundings and the heat source is localized, process times are shorter, and there is an atmosphere. These fundamental differences warrant wettability testing to be conducted for laser brazing even if wetting had occurred in a vacuum furnace.

All wettability tests had an Ar atmosphere with less than 15 ppm of oxygen. Firebrick backing was used in all the experiments to provide consistent thermal behavior to the preheat calibration performed earlier. Laser power was maintained at 200 W for all samples, with an intensity of 120 W/mm<sup>2</sup>. Raster speed was one inch per second. These parameters were constant between the preheat raster and the secondary raster. All preheats were performed according to the raster pattern in Figure 3.2. Preheat temperature was controlled by shutting off the beam for a certain amount of time to allow the RB-SiC to cool to the desired temperature. Temporarily shutting off the beam also eliminates thermal gradients in the samples prior to secondary rastering. Secondary rastering was done according to the pattern in Figure 3.5. All filler metal cuboids weighed 0.1 grams and did not exceed an aspect ratio (as defined in the Experimental Procedures Section) of 1.5. Experiments had secondary raster times of three, ten, and thirty seconds. The single exception was a sample given 300 seconds of secondary raster time. One sample was treated to only the preheat raster to verify the preheat did not cause melting. Another set of three samples were given the secondary raster without the preheat raster. Examining surface features and measuring contact angles was accomplished through light optical stereoscopy. Select samples had the surface imaged by scanning electron microscopy. Some samples were also sectioned through the middle of the filler, polished, and imaged with scanning electron microscopy. A stereoscope image of the preheat-only sample without a secondary raster is shown in Figure 4.15.

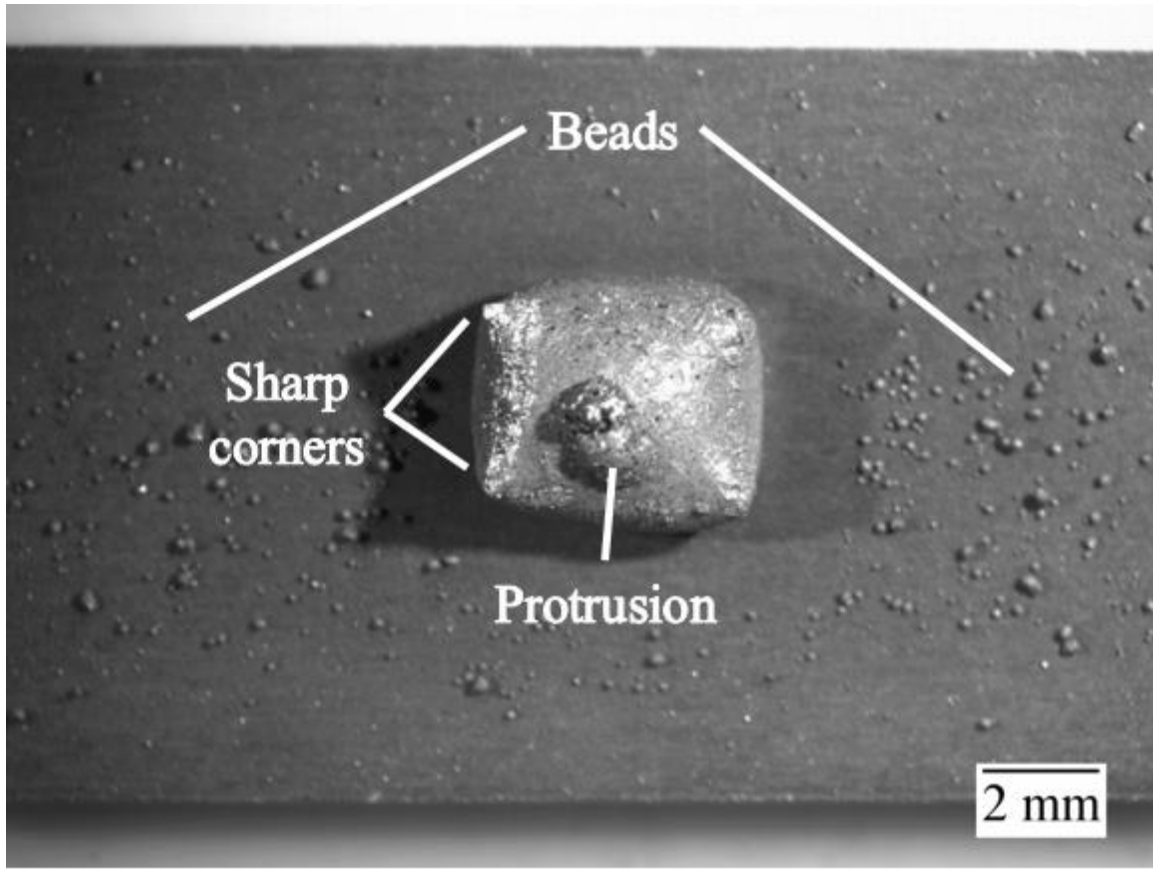


Figure 4.15 Light optical stereoscope image of wettability sample given only preheat raster

The sample is somewhere between the initial cuboidal shape and the spherical cap shape of the other samples. This result occurred because the sample experienced only partial melting. If the sample had completely melted, the filler metal would have been pulled into the spherical cap shape as in the other samples by surface tension. Melting, if any, of the filler metal would not leave the filler metal in the cuboidal shape. Except for specific compositions at features such as eutectic points, alloys do not melt at an exact temperature. Instead, alloys begin melting at the solidus temperature and finish melting at the liquidus temperature.

#### 4.4.1 Melting and Solidification Behavior

The Si-Al-Ti alloy has a pronounced difference between the solidus and liquidus. Figure 4.16 shows a Thermo-Calc simulation of the phase fractions present in the ternary filler system with increasing temperature.

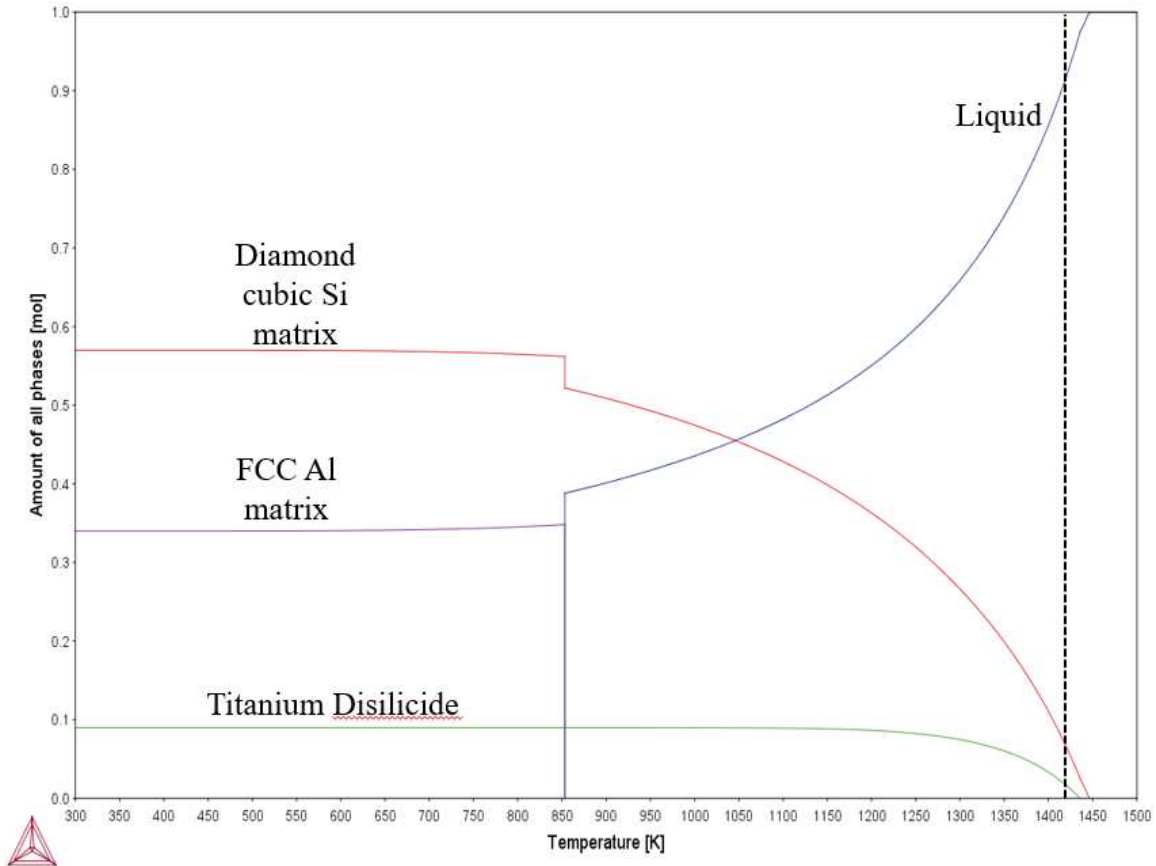


Figure 4.16 Simulation of melting in filler metal with phase descriptions added

At a temperature just below the solidus temperature of 850 K, three phases are expected to be present. These are 0.56 mol fraction of diamond cubic Si, 0.35 mol fraction of FCC Al, and approximately 0.09 mol fraction of  $\text{TiSi}_2$ .

According to pyrometer data recording of temperatures at the middle of the top surface on the filler metal, the peak temperature at the end of preheat rastering is approximately 1145 °C, (1418 K). The diagram shows this temperature (dashed line in black) is well within the melting range of the alloy but not above the liquidus temperature, explaining the partial melting behavior. However, adhesion is still present; the filler metal remained attached to the surface of the sample when removed from the chamber. Aluminum is the first element to melt and capable of wetting to silicon carbide as a pure element [35]. Titanium is the most active element in this filler metal, but the last element to melt since it is contained in  $\text{TiSi}_2$ . Aluminum is considered active in this system as well since it is thermodynamically capable of forming aluminum carbides by splitting SiC. Naturally, silicon will wet to silicon carbide. A Si-Al alloy will also wet and adhere to SiC

without Ti content [60]. Thermodynamics predict roughly half of the titanium in the filler is molten at 1145 °C, and the time spent below this temperature is longer than the time spent at this temperature due to the time it takes to reach steady-state. Titanium likely contributes to adhesion in this case by forming a reaction layer but cannot be said to be wholly responsible. The aluminum and silicon content of the alloy is the primary cause of the adhesion of the filler metal despite not fully melting. Aluminum aids in wetting because it can form a reaction layer, though not as strongly as Ti. Silicon is able to wet to both the Si and SiC phases in RB-SiC because it only needs to form more of the same bonds as what already exists within the substrate. These phenomena are further demonstrated in the three tests where there was no preheat. Pyrometer data recorded during these tests is shown in Figure 4.17.

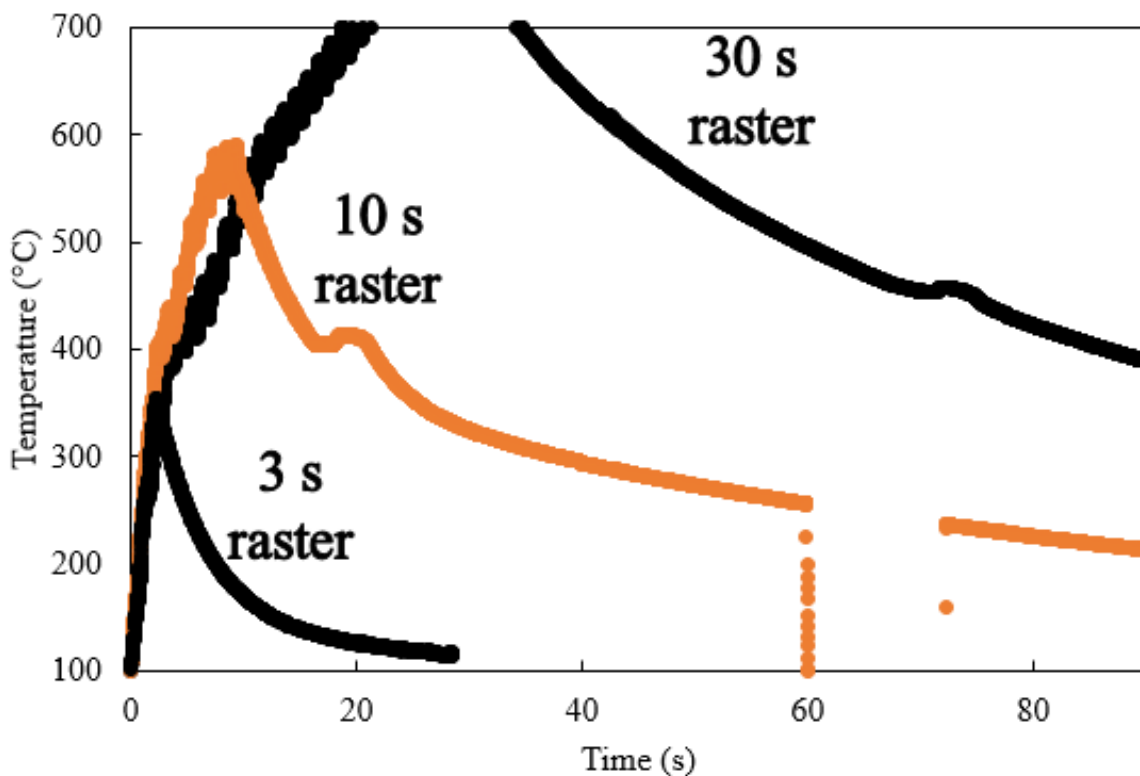


Figure 4.17 Low temperature pyrometer data from wettability tests with only a secondary raster

The gap in the 30 s rastered sample data exists because the low temperature pyrometer cannot measure values above 700 °C, and the gap in the ten second sample exists because of an unintentional obstruction in the path of the pyrometer beam. Extrapolating the two sides of the curve for the 30 second raster gives a peak temperature of around 780 °C. The two longer exposures also show solidification humps. Since free Si in the RB-SiC melts at much higher

temperatures than these humps (411 °C and 456 °C), proving partial liquation of the filler metal at lower temperatures. However, partial melting appeared to be less extensive than in the preheat only sample and not enough for adhesion. Proof lies in how they mostly retained their cuboidal shape and did not stay on the substrate surface at all. Simply tilting these samples while removing them from the chamber caused the filler metal to slide off. Inspection of the samples with three and ten second rasters showed few visible changes. The 30-second raster sample showed an interaction zone as shown by discoloration of the RB-SiC, but the discoloration does not cover the entire area where the filler cuboid contacted the surface as shown in Figure 4.18.

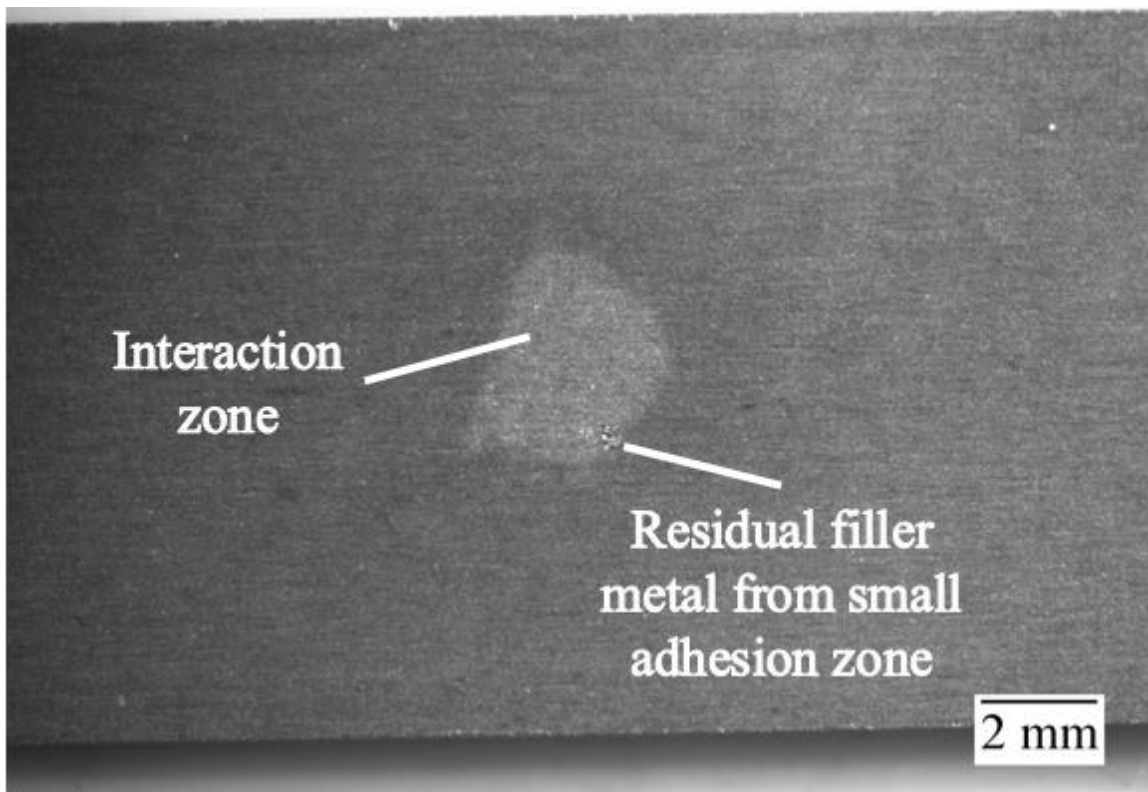


Figure 4.18 Surface interaction zone on wettability sample given only 30 s secondary raster

In addition to the interaction zone, there is a small island of adhesion too weak to hold the remainder of the filler in place. The surface of the RB-SiC is completely void of the beads exuded during higher temperature experiments, proving melting and flow of free Si is the source of the beads. The trials involving only the preheat and only the secondary raster showed both are needed to fully melt the filler and allow the filler metal to interact with the substrate. Preheat rastering was designed to spread heat over the entire sample. At most, the preheat can reach a steady-state temperature as described by Equation 4.2, which predicts a steady-state temperature

of 1179 °C or 1450 K for the RB-SiC alone. Having filler metal present decreases the steady-state temperature via an increase in surface area available for radiative losses. The melting point of the filler is 1170 °C but pyrometer data only show steady-state temperature in the preheat reaching 1145 °C, which is below the filler melting temperature. Preheating alone is inadequate for the brazing process to complete. Additionally, practical brazing typically involves a superheat of at least 50 °C above the melting temperature to ensure complete melting of the filler. Laser brazing will need even higher superheats to counteract the shorter process times.

Having a secondary raster would allow the filler to fully melt and adhere to the surface. However, performing only a secondary raster near the area to be joined without preheating would result in large thermal gradients potentially leading to inconsistent metal flow behavior. The thermal gradients would compromise the strength of the joints and possibly lead to a lack of joining in cooler areas. The preheating step makes the entire substrate warmer, reducing thermal gradients during the secondary raster to create a stronger joint. Heat sources other than laser could function just as effectively for preheating. Thus, the secondary laser raster is uniquely developed in this work - delivering more heat in a smaller area than other methods.

The combinations of preheat temperature and secondary raster time capable of producing sound joints are limited. Too much time spent on the secondary raster will cause excessive surface damage to the substrate, lose filler metal to vaporization, and increase the depth of diffusion of chemical elements into the substrate exceeding desirable amounts. Increased preheat temperatures reduce the amount of time needed for the secondary raster because of an already hot substrate. Figure 4.19 is a light optical stereoscope image of a sample given a 455 °C preheat and three seconds secondary raster time, with a maximum temperature of 671 °C after the preheat.

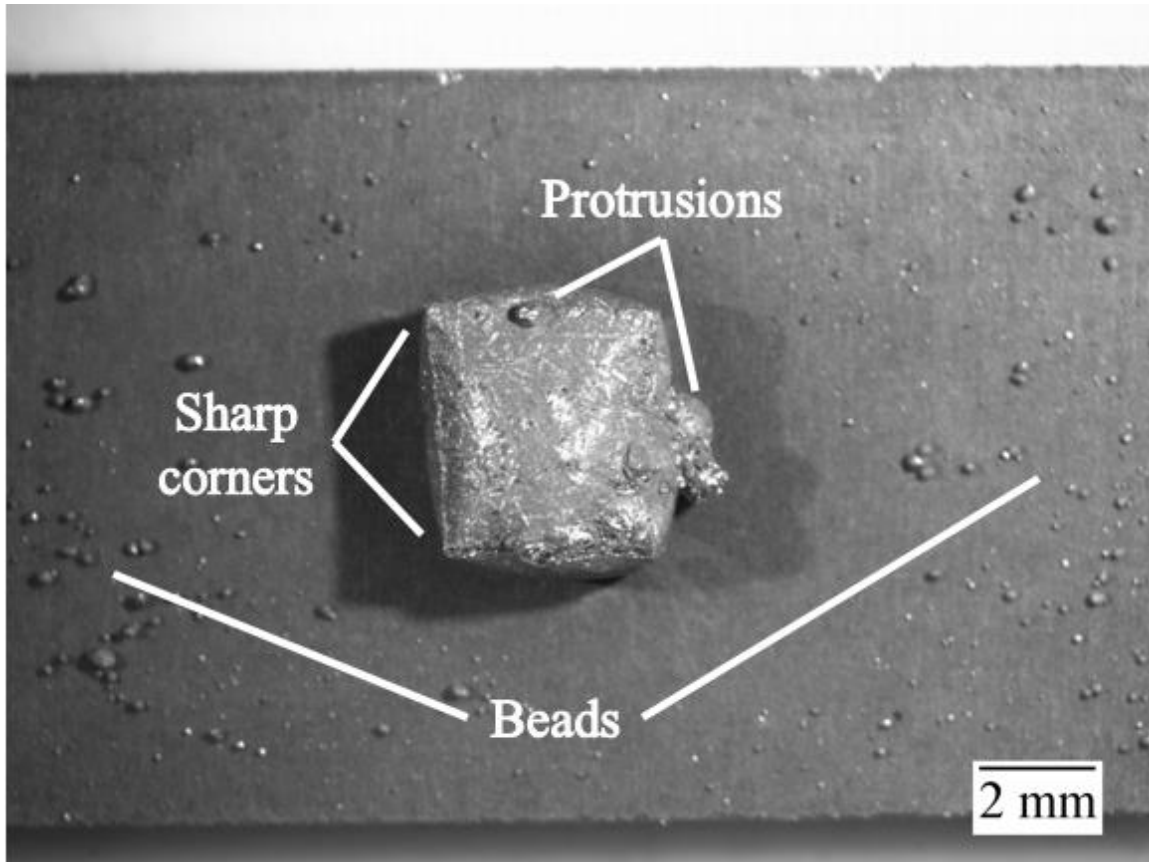


Figure 4.19 Sample given 455 °C preheat and three second secondary raster, the lowest parameters providing adhesion

The sample in Figure 4.19 shares similarities with the one given only the preheat raster. Beads have appeared on the surface because the preheat reached temperatures high enough to melt free Si in the RB-SiC, but the filler metal had not completely melted (with the retention of the cuboid shape). Pyrometer data showed the peak temperature achieved in the secondary raster of 668 °C, well below the melting point of the filler. While the secondary raster slowed the solidification of the partially molten filler metal, there was not enough energy delivered for melting. Liquid silicon and aluminum adhered to the surface, so the filler was attached, but not molten enough to properly develop a sessile drop with measurable contact angle. Another significant feature to allude to is the protrusion on the filler metal. Energy dispersive spectroscopy performed during scanning electron microscopy revealed these protrusions to contain Si and Al. Figure 4.20 shows a Scheil solidification simulation of this alloy generated using Thermo-Calc.

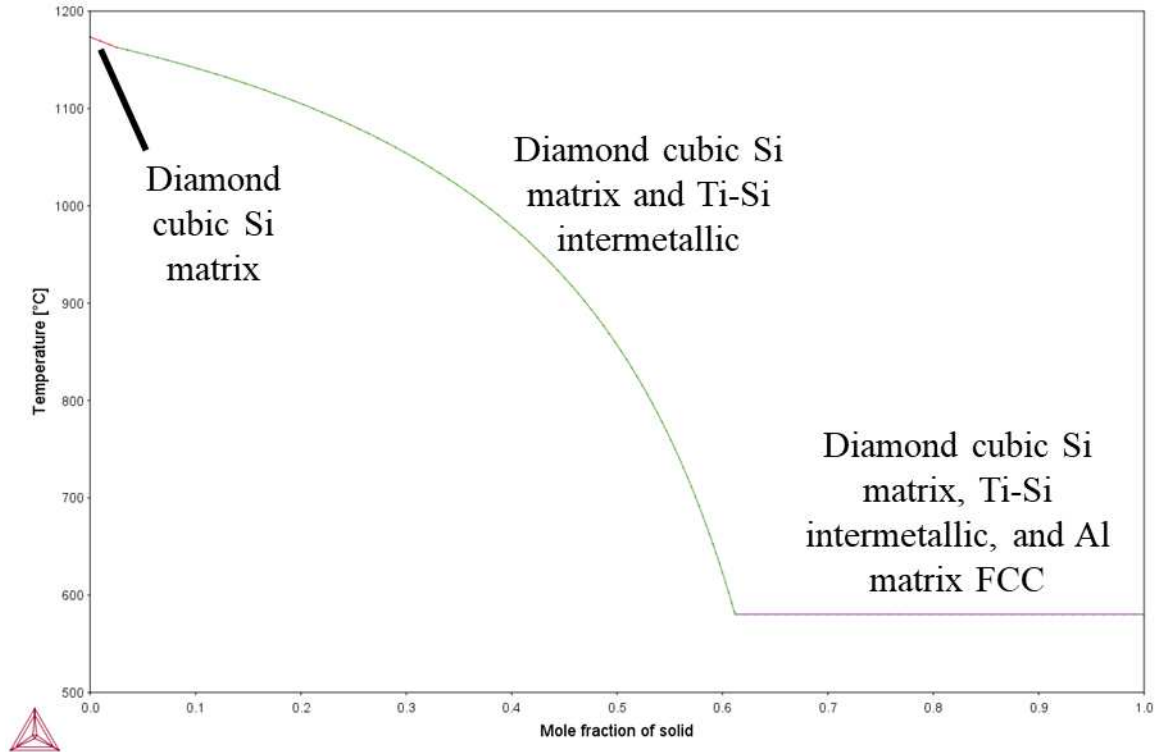


Figure 4.20 Scheil solidification simulation of the filler metal with phase labels

The aluminum dominant phase is the last to solidify, with Si ending the solidification process in similar temperature ranges. This analysis suggests the protrusions are comprised of Al and Si, while theory predicts titanium disilicide to solidify at this temperature as well. Scheil simulations only account for the effect of segregation during solidification but do not consider the effects of cooling rate changes. When the filler metal interacts with the RB-SiC substrate, Ti strongly segregates to the RB-SiC. The filler metal either forms surface reaction products or diffuses into the bulk RB-SiC with the remaining filler metal depleted in Ti. The leftover Ti tends to be closer to the surface of the substrate and located within the first regions to solidify.

Protrusions like those in Figure 4.19 are present in the lap joints and comprised of silicon and aluminum. They did not, however, appear to deplete the rest of the filler in titanium, the most crucial element for adhesion. Protrusions are more of a visual defect than a structural defect. They can be entirely avoided when making actual joints by placing constraints on the outside surfaces. They can also be easily ground off after joining. Since protrusions are outward irregularities and not divots, they do not act as stress concentrators nor compromise the structural integrity of the joint. Protrusions make contact angle determination complicated as they do not

allow for the viewing of the actual triple line in some cases. Some samples developed protrusions while others did not. The morphology of the protrusions also varied considerably; sometimes in elongated shapes and other times, more spherical in nature. Silicon expansion during solidification is the most likely explanation for the appearance of protrusions. Pure silicon is known to expand during solidification, and the filler metal alloy is mostly silicon.

#### **4.4.2 Oxidation in Wettability Testing**

Because the atmosphere contained some amount of oxygen, oxidation of the protrusion surfaces is in line with thermodynamic predictions. As the filler metal contained Si, Al, and Ti, which are all strong oxide formers, oxidation was expected to occur during testing. It is important to note that oxidation also occurred during synthesis of the filler metal, but that oxidation was restricted to the surface of the melted droplets; the surface material was not incorporated when preparing samples for testing because of this. The tendency of each element to oxidize can be predicted from an Ellingham type diagram. Figure 4.21 shows an Ellingham diagram with the three elements in the filler metal highlighted.

Oxygen concentration in the atmosphere was estimated to be at most 15 ppm, with a pressure of 1.1 to 1.2 atmospheres. These values correspond to a maximum possible oxygen partial pressure of  $1.8 \times 10^{-5}$  atmospheres, well above the minimum amount to oxidize the filler metal. RB-SiC is also susceptible to oxidation, particularly the free Si network. Based on the Ellingham diagram, aluminum is expected to experience more oxidation than the other components due to its higher affinity for oxygen. This effect is beneficial, as aluminum will preferentially oxidize and protect titanium from oxidation. As adhesion requires titanium, oxidized titanium will not be able to provide the active metal reactions necessary for wetting and adhesion. Sacrificial oxidation of aluminum helps increase the strength achievable.

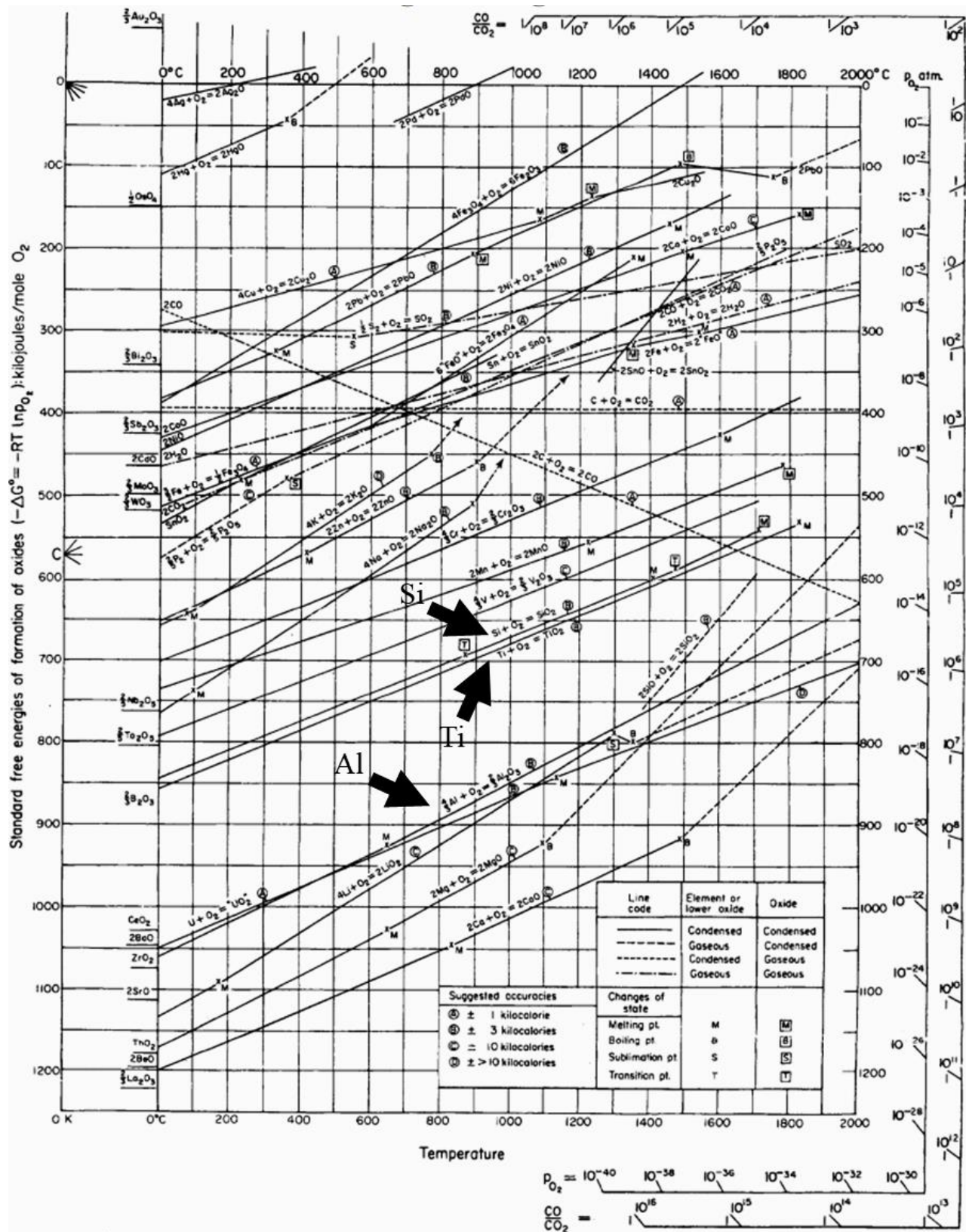


Figure 4.21 An Ellingham diagram with the elements in the filler metal highlighted [61]

If enough oxygen is present, aluminum will form an oxide layer on the surface of the filler while the filler is molten. The combination of aluminum solidifying last and having the greatest affinity for oxygen (amongst the three alloying elements in the filler) results in a skin that is predominately aluminum oxides. Most of the remainder of the skin will be silicon oxides, with minor amounts of titanium oxides. Titanium oxides are not expected to be plentiful because titanium tends to segregate to the RB-SiC surfaces and diffuse inward. Low concentrations of titanium in the filler before melting may also contribute to this phenomenon. Oxides have higher melting points than metals, so the oxide layer present on the outside surface is semi-solid. Pure alumina melts at 2072 °C, pure silica melts at 1710 °C, and pure titania melts at 1843 °C. These values are well above the temperatures reached during joining. Figure 4.22 shows EDS maps of a region on the top surface of a solid filler metal drop after a wettability test with a 1050 °C preheat and 300 seconds of secondary raster time.

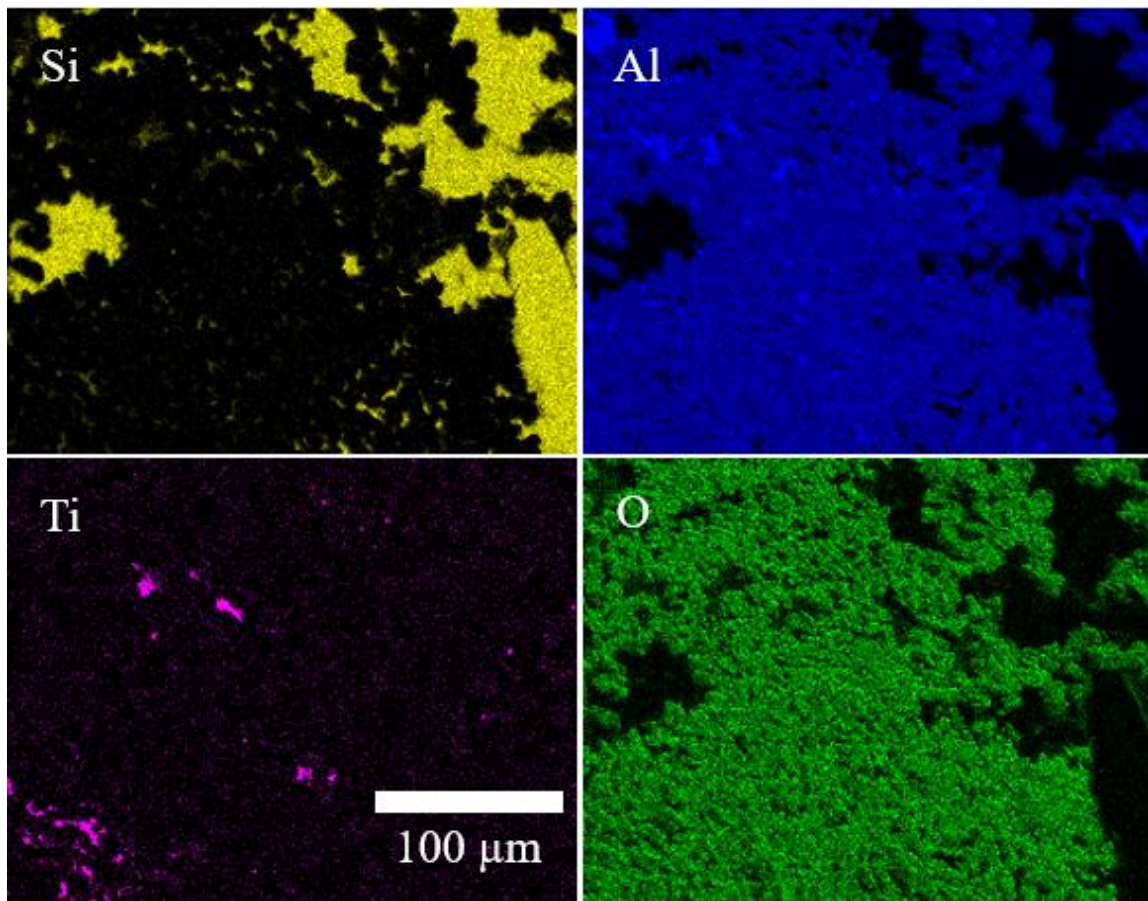


Figure 4.22 EDS maps of oxidized filler metal surface after wettability test

The sample in Figure 4.22 is a good representation of the oxidation behavior of a sessile drop that underwent a prolonged thermal cycle; its temperature was maintained longer than any other wettability samples. These images show oxygen is predominately bonded to aluminum, with silicon also oxidized, but to a lesser degree. EDS map intensity does not display an absolute quantity. Instead, this method displays the relative intensity of the element throughout different regions. A pure element would have an EDS map solid in color, as would the map for an element evenly distributed throughout a matrix of another element. Silicon on the surface would still be oxidized, but less than the aluminum. Titanium was also observed on the surface of the drop but not in large quantities. These elemental distributions are in line with predictions of where the three filler metal elements and oxygen should appear based on thermodynamics and Scheil simulation predictions.

Aluminum protects titanium from oxidation so titanium can react with the substrate. Having an  $\text{Al}_2\text{O}_3$  layer poses problems since it will hinder spreading of the molten filler on the substrate.

#### **4.4.3 Contact Angles**

The ability to spread depends on the balance of surface energies at the triple line. Oxides of the filler metal do not have high wettability on the RB-SiC surface and appear on the surface which includes the triple line. Contact angles achieved are influenced by oxidation and thus the ability of the triple line to advance is also affected by oxidation. Figure 4.23 shows the contact angles achieved as a function of preheat temperature and secondary raster time for completely melted samples.

The data seem to indicate that secondary raster time had the largest influence on reducing contact angle to approximately  $90^\circ$ . The effect of the preheat was unclear. However, the purpose of preheating was to uniformize the temperature on a sample while secondary raster controlled the final temperature of wetting. The samples that did not receive a secondary raster and the samples that were not given any preheat were omitted from this plot because of incomplete melting and incomplete measurements of contact angles. Ordinarily, contact angles this high would be cause for declaring a filler-substrate pairing unsuitable, but oxidation effects influencing the contact angles make this case an exception. The current issue is not wetting as will be demonstrated later; instead, it is spreading, which is why this filler was still used for lap

joint testing. Samples with surface texturing and the sample that received a 300 second raster are reported in Table 4.2.

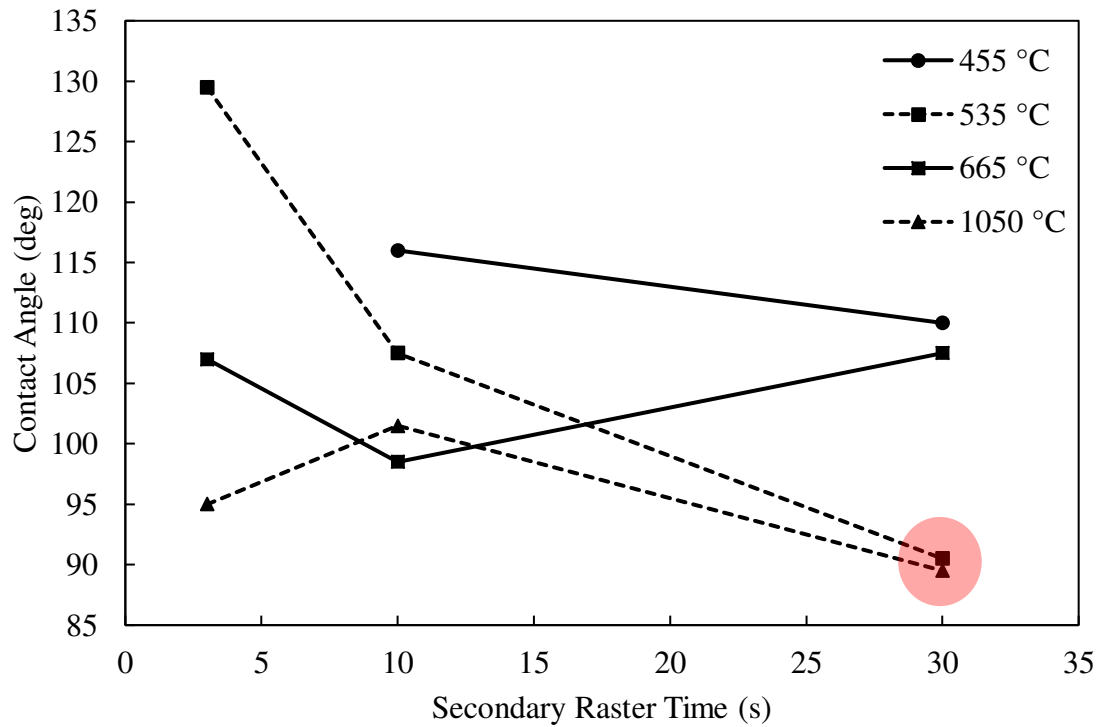


Figure 4.23 Contact angles as a function of preheat temperature and secondary raster time

Table 4.2: Contact Angle Responses for Samples with Unique Processing Conditions

| Processing Condition                                    | Contact Angle |
|---|---------------|
| 1050 °C preheat, 30 s secondary raster, 150 W, textured | 115°          |
| 1050 °C preheat, 30 s secondary raster, 200 W, textured | 118°          |
| 1050 °C preheat, 300 s secondary raster                 | 97°           |

Wetting did not occur according to the definition of low contact angle, as shown by Figure 4.23 and Table 4.2. Higher contact angles were seen in the surface textured samples because the laser texturing was performed in air. The oxidized surfaces were not as wettable by the filler metal, causing a rise in contact angle. The thin passive oxide layer that normally forms

on RB-SiC because of exposure to air is broken down during the active metal brazing process, but the layer would be thickened during texturing. The thicker oxide layer would require more time to break down. The texture from the holes also increased contact angles because wetting onto an irregular surface requires temporarily achieving lower contact angles. The filler metal could not achieve these lower contact angles, preventing spreading. The filler was unable to advance as needed to achieve the true equilibrium contact angle, as shown by the contact angle results for the same thermal parameters but without texture on the surface.

A drop is defined as wetting a substrate if the contact angles produced is less than  $90^\circ$ , the cut-off between where interfacial energy starts overcoming the surface energy of the substrate. Contact angles greater than  $90^\circ$  indicate the surface tension of the droplet - which is identical to surface energy for ideal solutions - was greater than the interfacial energy with the substrate. When this is the case, surface tension pulls the liquid to decrease surface area, reducing the contact area with the substrate in the process. Some contact is kept with the substrate because there is still some energy saved by contacting the substrate. Exceptions exist in cases like extreme hydrophobicity in materials with an equilibrium contact angle of  $180^\circ$  with water, but creating perfect non-wetting takes some surface engineering. Liquids on an incompatible substrate will still retreat to the equilibrium contact angle and not advance on the substrate.

#### **4.4.4 Sessile Drop Microstructure**

When applied to brazing and wettability tests, a non-wetting interface is expected to see gaps caused by the roughness of the solid before melting. In the case of the filler metal cuboids, these were ground to the correct size and weight using a 180 grit sandpaper and, therefore, exhibit surface roughness for non-wetting to be observed. Conversely, the interfaces inside of the solidified sessile drops are free of gaps. Figure 4.24 shows the cross-section of the incompletely melted sample given a  $455^\circ\text{C}$  preheat and three seconds of secondary raster time, with a maximum temperature of  $671^\circ\text{C}$  after the preheat.

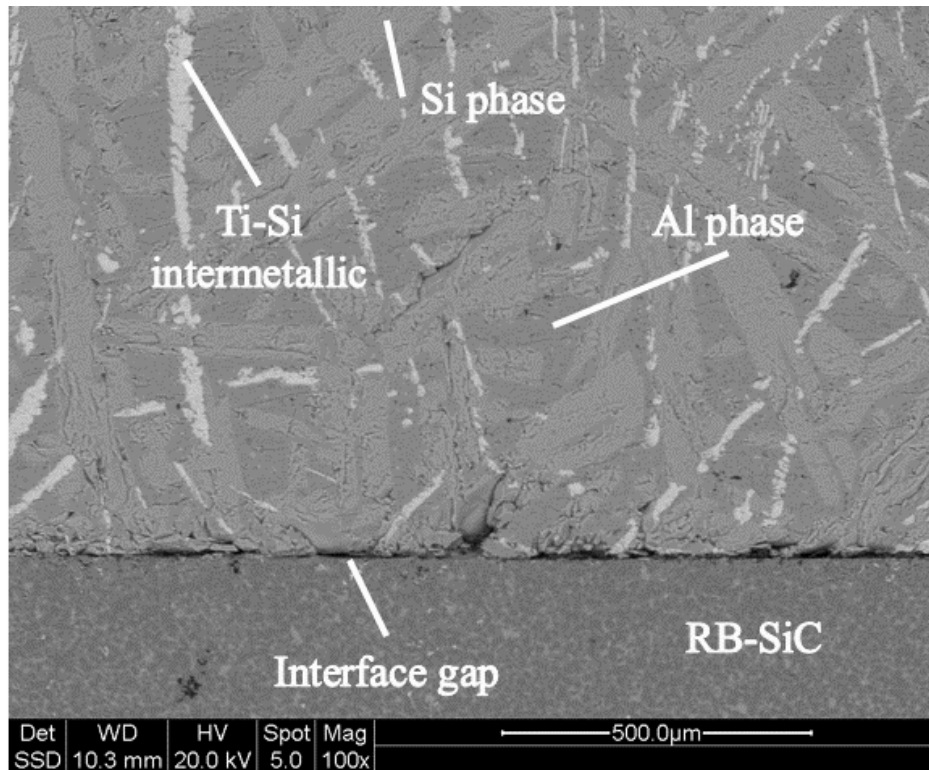


Figure 4.24 Electron backscattered electron image of sample given 455 °C preheat and three seconds of secondary raster time, with emphasis on the filler-RB-SiC interface

The light gray phase in the upper region is Si-Ti intermetallic, the dark gray phase Al matrix FCC, and the gray phase is Si matrix diamond cubic. In the lower region, the dark phase is SiC, the lighter phase free Si, and the bright phases are either Ti diffused into the substrate or Fe from the synthesis process. This same discussion holds true throughout the work, as all backscattered electron imaging took the sum of the signal from either side of the detector which gives contrast based on composition. Higher atomic numbers appear brighter and lower atomic numbers appear darker. Interfacial bonding occurred to the point where the sample could be cross-sectioned with a slow speed saw, mounted, ground, and polished without the filler metal detaching despite incomplete melting. However, the lack of complete adhesion is clearly visible in the extensive gaps. On the other hand, good adhesion should exhibit complete contact between the filler and substrate.

Figure 4.25 depicts an image generated the same way as Figure 4.24 but from a sample given a 650 °C preheat and 30 seconds of secondary raster time with a maximum temperature over 700 °C after the preheat.

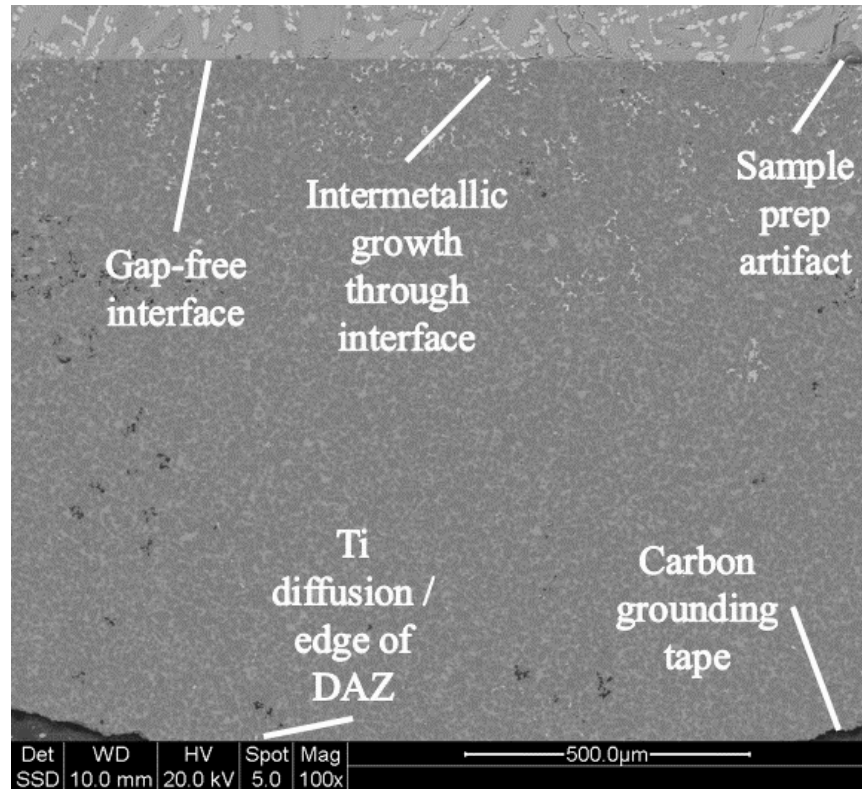


Figure 4.25 Electron backscattered electron image of sample given 650 °C preheat and 30 seconds of secondary raster time, with emphasis on the filler-RB-SiC interface

The hole in the top right corner is an artifact from grinding and polishing, and the features in the lower corners are carbon tape for grounding. The filler metal was fully melted and had a much deeper diffusion-affected zone (DAZ). No gaps were observed along the filler-substrate interface in Figure 4.25. Ti-Si intermetallic was observed to grow from the substrate into the filler metal, which is evidence of intimate contact and wetting between the substrate and filler. Such behavior is contradictory to the behavior observed on the surface where the lowest contact angle achieved was 90° within rounding. In the interior of a joint (Figure 4.25), where the joint interface is isolated from the atmosphere (in the absence of oxygen and oxidation products), wetting can occur, reaffirming the earlier statement that the issue is not wettability, but spreadability of filler metal with an oxidized skin.

Diffusion affected zone depth was deep and Ti was present in the very bottom of the micrograph, giving a DAZ depth of over one mm. Titanium is confirmed as being present in the spot labeled by EDS spot scanning. Probing greater depths beyond one mm did not detect any Ti. The large DAZ can be both good and bad. Diffusion into the substrate is needed to condition the

surface layer and allow for wetting and adhesion. Diffusion into the substrate is also deleterious to its mechanical properties because of the reaction products and elemental redistribution. In the ideal case, the active element would diffuse into just the top few layers of the substrate to allow wetting without forming a significant DAZ. Both diffusion depth and adhesion depend on time and temperature, so optimizing joint strength requires balancing these two factors.

Prolonged time at temperature appeared to have an effect on contact angle, but the effect of oxygen makes it unclear. The sample given a 300 second secondary raster had a higher contact angle than the sample at the same 1050 °C preheat given a 30 second secondary raster. This sample had unique behavior relative to the other samples as well, where some portions of the droplet showed signs of wetting and spreading outwards while other areas exhibited the same high contact angle behavior as other samples. An image of a region on the sample showing wetting behavior is shown in Figure 4.26.

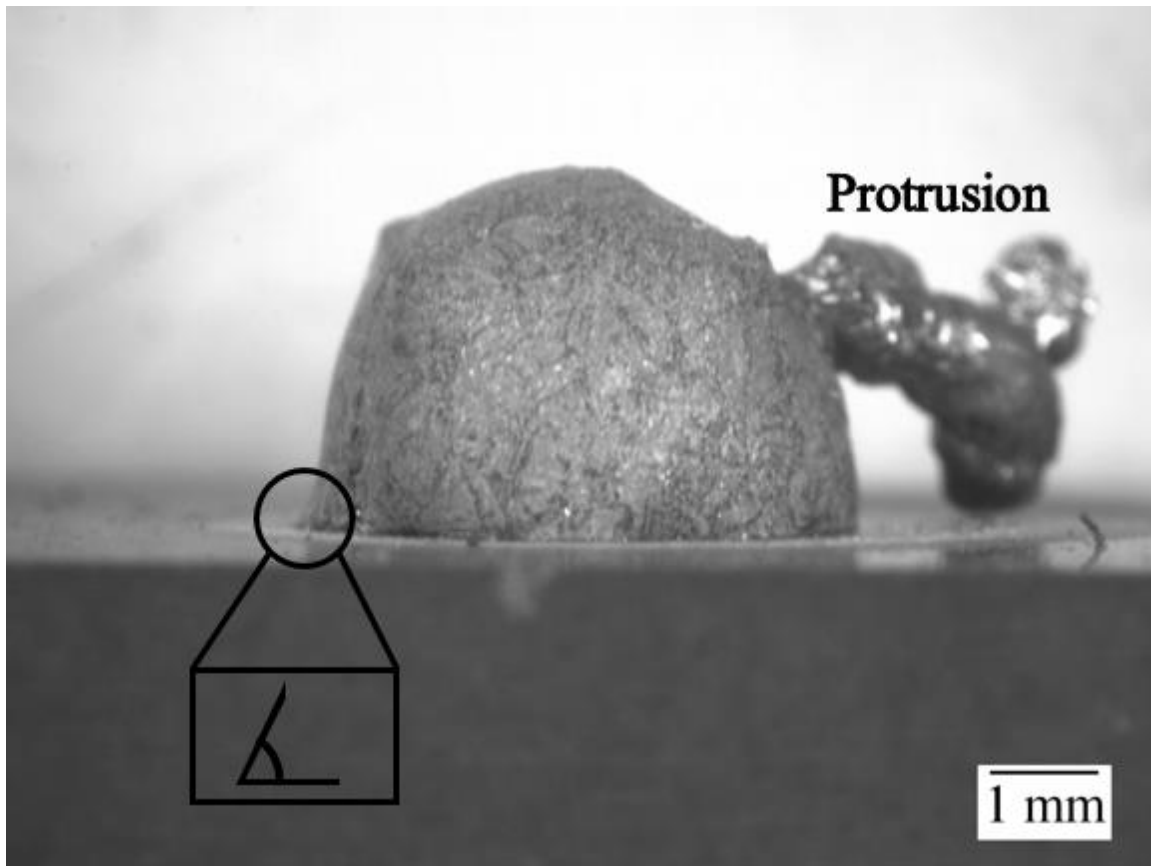


Figure 4.26 Inconsistent wetting behavior of sample given 1050 °C preheat and 300 second secondary raster, image in grayscale

The right side of the sample has a contact angle close to  $90^\circ$ , while the left side has approached a contact angle closer to  $60^\circ$ . The variation in contact angle along the contact line reflects a change in local composition or properties, or processing conditions. Variation in contact angle is common in wettability testing, so this is not unexpected.

Another indication of inconsistent properties throughout the sample is the massive protrusion seen on the right. The prolonged times also enable high diffusion depths. The 30 seconds of secondary rastering with a  $650^\circ\text{C}$  preheat resulted in a diffusion depth of over one mm. First approximation diffusion calculation as a function of the square root of time predicted diffusion depth over three mm. Since the samples are 3.175 mm thick, the expected DAZ depth is on the order of the sample thickness. Figure 4.27 shows filler metal, namely Ti and Al, diffusing through the thickness of the sample and appearing on the side opposite the laser. Silicon may be diffusing as well.

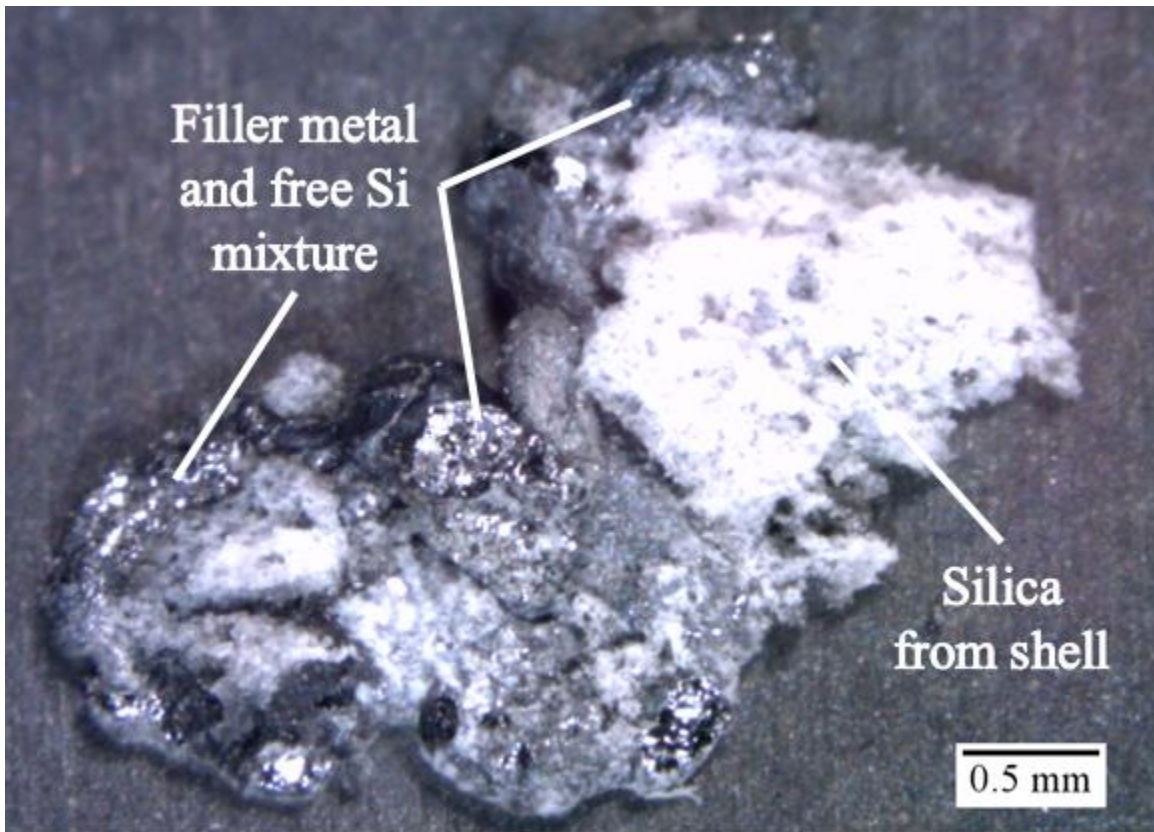


Figure 4.27 Filler metal diffusion through the thickness of the sample and free Si loss during wettability testing with a  $1050^\circ\text{C}$  preheat and 300 second secondary raster

Parts of the image in Figure 4.27 are not in focus because the sample is tilted by the filler metal drop on the side resting on the stereoscope stage. The white substance seen on the surface is firebrick bonded with the metal. Porosity in the firebrick restricted where the filler metal could flow, causing the irregular morphology. Force was required to remove this sample from the firebrick surface because there was adhesion, albeit the total area bonded was not great. Diffusion on a large scale is the cause of the sample's unusual behavior. If filler metal diffuses through the entire thickness of the sample, it is reasonable that extensive lateral diffusion also occurred. Figure 4.28 shows a top down view of the sample from a light optical stereoscope.

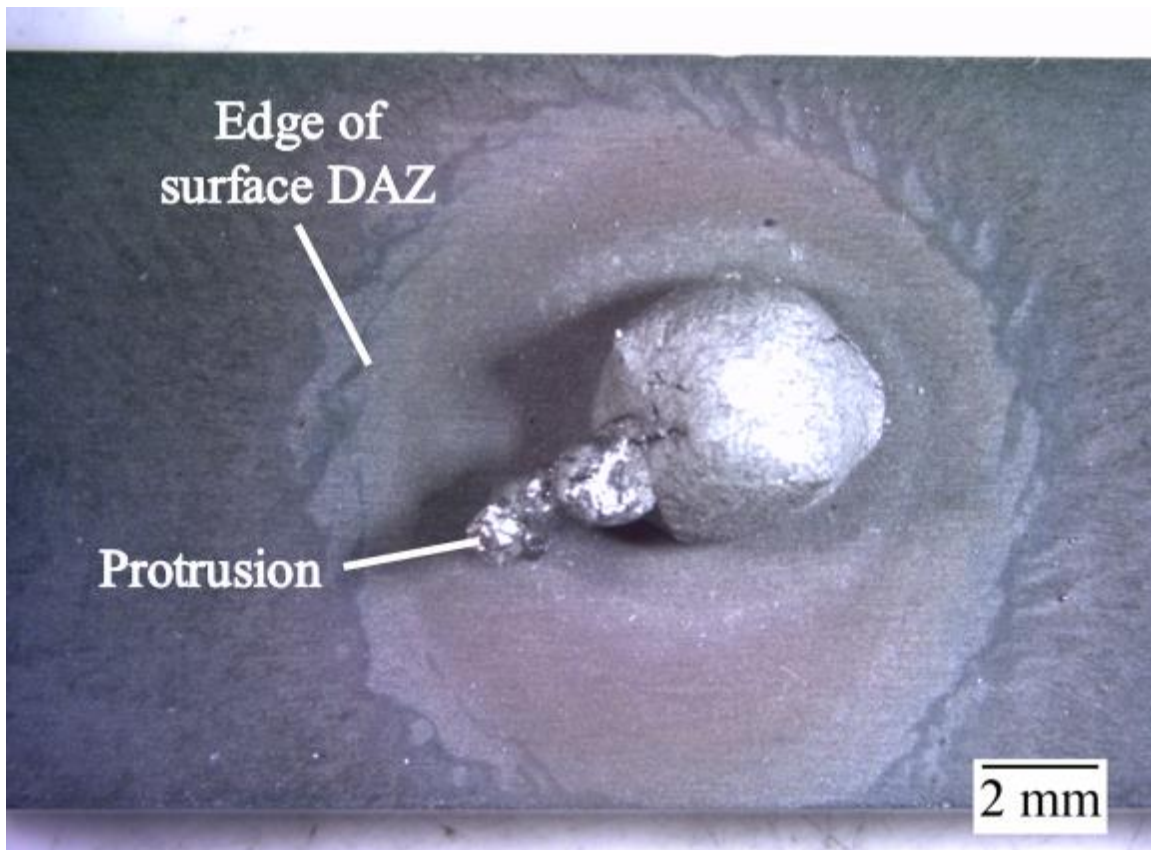


Figure 4.28 Top down view of sample given 1050 °C preheat and 300 s secondary raster

A zone of discoloration exists around the filler metal. The appearance resembles the zone of discoloration in Figure 4.18, which was created by limited diffusion in a partially melted sample. The discolored region is around three mm in width, with some variability. This observation agrees with the prediction of how deep the DAZ is, proving the metal seen on the other side of the sample comes from through-thickness diffusion and not contamination. Having this much diffusion occur significantly alters the composition of the metal left behind. All three

elements diffuse through the substrate, but diffusion is only measurable and meaningful for Ti and Al. Being the substrate and filler metal are both silicon rich, Si atoms that diffuse away will simply be replenished with other Si atoms from the surrounding. Losses of Ti and Al have deeper consequences, however. With Ti and Al diffusion into the substrate, the filler metal becomes increasingly richer regarding Si content. As Si expands by ten percent at solidification [62], the protrusion formed also got larger. Expansion of Si during protrusion also caused cracking through the oxide coating to expose the metal underneath. Figure 4.29 shows a higher magnification image of this region.

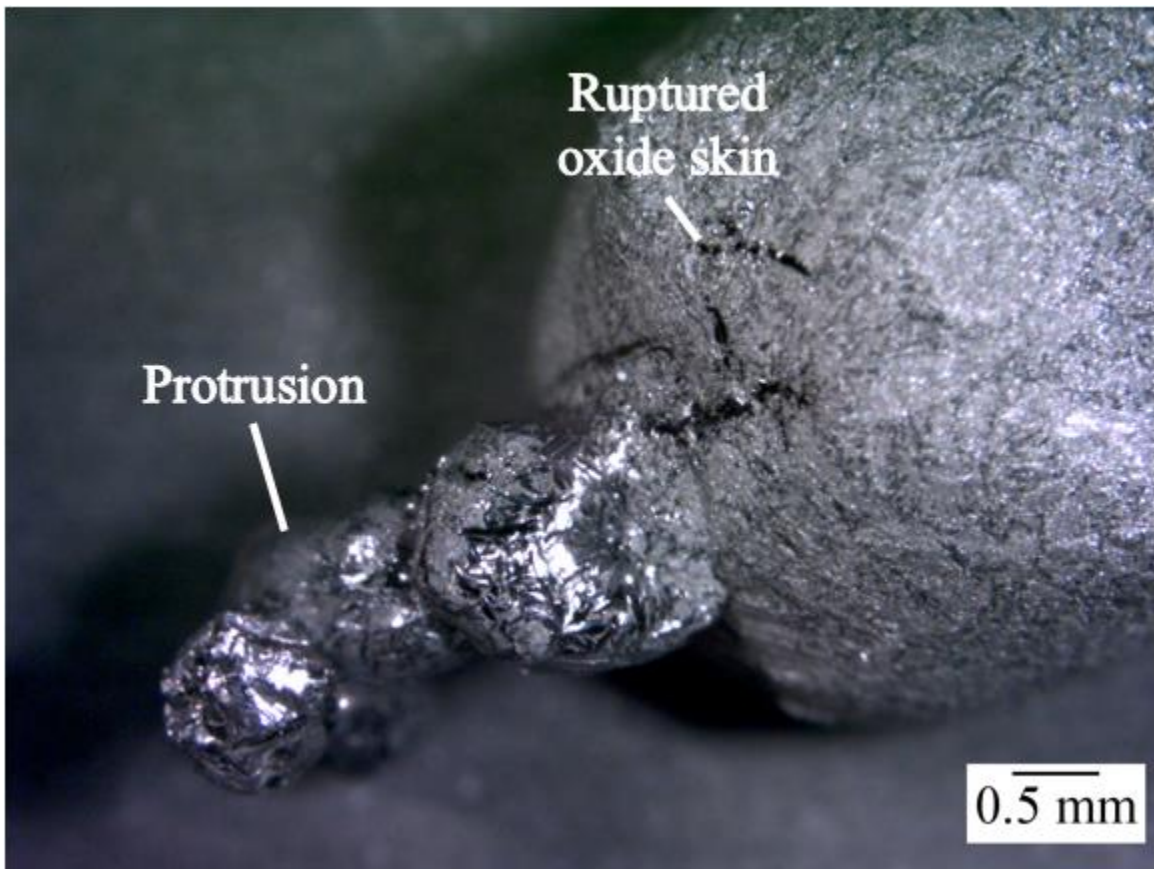


Figure 4.29 Higher magnification image of protrusion developed during solidification

Other cracks are visible in the oxide coating on the surface, caused by the decreasing concentration of Ti and Al and enrichment of Si leading to the increased expansion of Si during solidification. The metal underneath the cracks appears different in color than the aluminum and silicon oxide coating. The ruptured oxide coating exposed the silicon-rich metal underneath.

Figure 4.30 shows a backscattered electron image of this sample to conclusively prove the model presented.

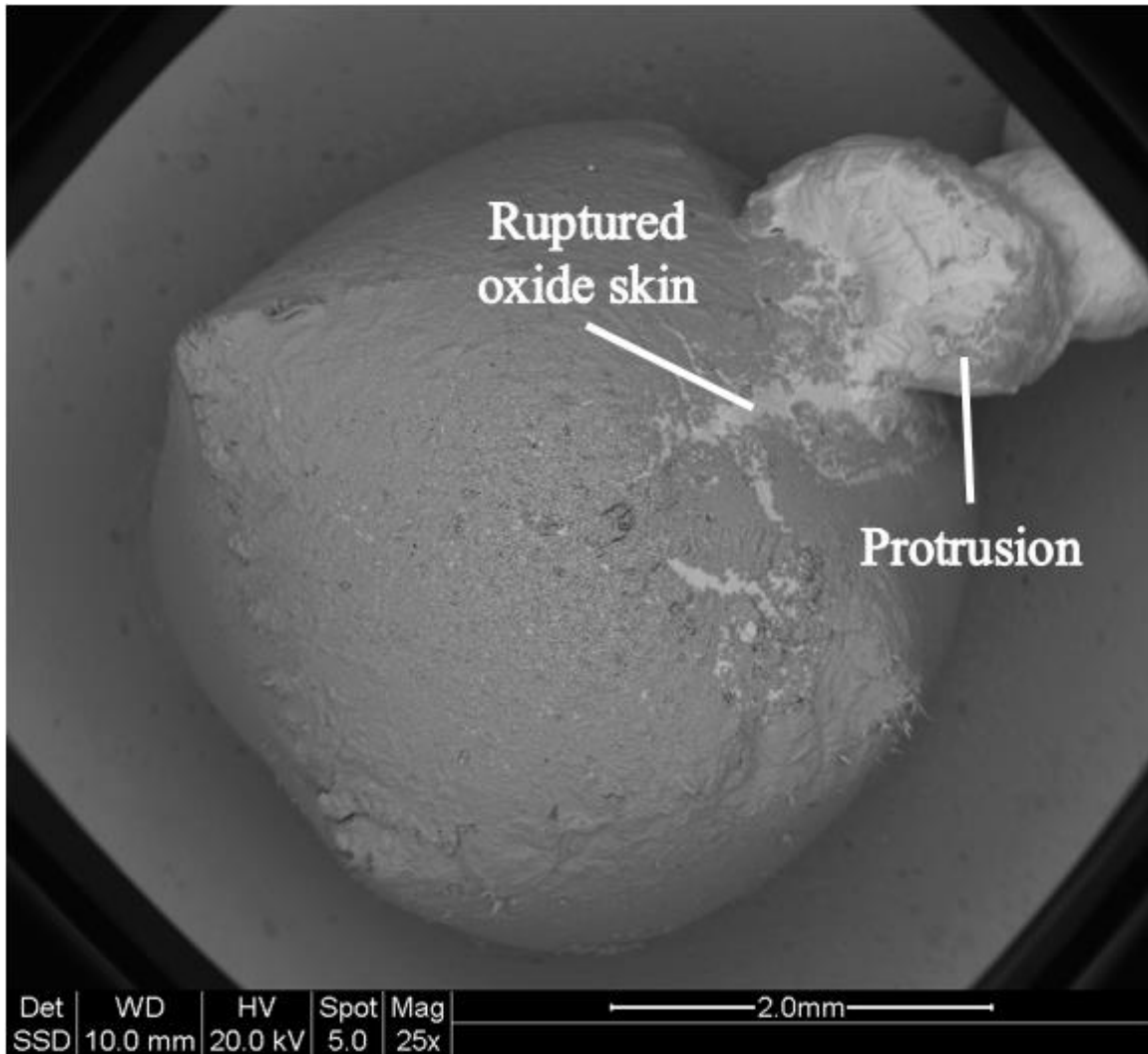


Figure 4.30 Backscattered electron image of sample given 1050 °C preheat and 300 seconds secondary raster

The region declared to be silicon is brighter in this image, indicating the area is higher in atomic number than the rest of the surface. Since only Si and Al are present in large quantities in this photomicrograph, those would be the two elements detected. Aluminum oxide covered most of the filler metal droplet and titanium segregated to the filler-substrate interface interior to the droplet.

Aluminum oxide existed as a solid coating floating on top of the liquid droplet because of its high melting temperature. A good visual comparison would be the crust of the Earth floating

on the mantle. Protrusions as the ones observed in this work is a strong reminder of the significant diffusional losses of Ti and Al.

The extensive diffusion was only possible because the sample was kept at elevated temperature for a long time. Reaction-bonded silicon carbide also facilitates diffusion with the continuous network of free Si acting as short-circuiting diffusion path; if sintered SiC had been used in this work, diffusion length would be much shorter.

The steady-state temperature was estimated to be approximately 1350 °C. Knowing the exact time at this temperature was not possible due to beam interference of pyrometer measurements, but estimations of time to steady-state temperature from extrapolation gave around 250 seconds. As such, free Si had generous time to melt and form beads during this time. Beads did not only appear on the surface of this sample in the form of exudation, they were absorbed into the filler metal as well. Based on the Gibbs-Thomson Effect, this method is the optimal way to reduce the free energy of the beads, so bead absorption will happen eventually if given enough time.

#### **4.4.5 Wettability Testing Summary**

The extent of diffusion also explains why portions of the triple line spread. Lateral Ti diffusion carried out the same reactions as those at the interface between the liquid filler and substrate, creating a wettable surface. Regions of local oxide breakthrough would then flow along this surface, spread outwards, and create the lower contact angle seen. Breaking through the oxide layer would be difficult because it was mostly made of solid aluminum oxides, which possessed strength and resilience. The weakening and breakage of the oxide layer actually depended on other factors as outlined below. Impurities such as Fe exuded from the RB-SiC substrate or mechanical forces such as solidification expansion could assist the breakage of the oxide skin letting the molten filler metal leak out.

Theoretically, adhesion correlates with contact angle, but the oxide layer on the external surface of the droplet interfered with this result. As a result of preferential oxidation as predicted by the Ellingham diagram, aluminum oxide formed on the droplet surface and hindered wetting and spreading. Interior interfaces, without the interference of oxygen, showed complete contact between the filler and the substrate.

Significant diffusion was also observed in selected samples where elements were seen to penetrate through the thickness of the sample. Varying amounts of protrusion growth were visible, depending on how Si rich the filler became after diffusional losses of Ti and Al. Regions of local oxide breakthrough showed wetting behavior that was reflective of the actual thermodynamic equilibrium contact angle between the filler and substrate. All of these factors aided in the design and analysis of lap joint testing.

#### **4.5 Lap Joint Testing**

Brazed joints in service are often designed to only experience shear stresses. Shear stress states are preferable in engineering applications because tensile stresses cause cracks to grow, though tensile stresses can still be present under pure applied shear. The low thickness of braze joints and difference in mechanical properties between the filler metal and substrate also tends to lead to a tri-axial stress state in the filler metal.

Lap or lap-butt joints are common ways of creating the shear stress state. The lap joint geometries can increase the area of the faying surfaces by simply moving the two pieces relative to one another. Butt joints require less substrate preparation but have less bonding area and tend to lead to tensile stress states. Strength is increased as a result, but the triaxial stress state can also lead to brittle fractures, making an applied shear stress state even more desirable. Testing single lap joints in shear is representative of how results of this joining technique will perform in service because shear stress and lap joints are both well adopted in industry.

Lap joints were made with the raster pattern described in Section 3.5 and a 2.3 mm beam diameter. Power was either 400, 500, or 600 W, so beam intensity varied in these experiments. Heating followed the same preheat-pause-secondary raster cycle as in wettability testing. All preheat times were 120 seconds, all pause times were five seconds, and secondary raster time was either 90, 120, or 180 seconds; one sample had a 60 second secondary raster. Filler metal was placed between the faying surfaces as a foil preform having a thickness between 200 and 250 or 250 and 300 microns. One foil had a thickness of 150 to 200 microns.

Every lap joint was made in the same controlled atmosphere chamber as wettability testing. Oxygen was controlled to a maximum of 13 ppm in every trial except for three. Two of these trials had Ar as the backfilling gas until an O<sub>2</sub> concentration of 15 ppm, then switched to a

5 vol% H<sub>2</sub> balance Ar mixture until an O<sub>2</sub> concentration of 10 ppm. One H<sub>2</sub>-bearing gas trial had a beam power of 600 W and 180 second secondary raster while the other had a 500 W beam and 120 s secondary raster. A third H<sub>2</sub>-bearing gas experiment was performed with the Ar-H<sub>2</sub> mixture being the sole gas fed through the chamber until 11 ppm of oxygen concentration. (Ten ppm was the target, but the cylinder was depleted mid-experiment.)

Samples made with the normal Ar gas conditions and the three special runs with hydrogen gas were shear tested to failure with the fixture in Section 3.5 at a crosshead speed of 0.5 mm/min. Strain rate inside of the joint was inconsistent in these runs because the filler metal thickness varied between samples. All samples experienced brittle failure and had a linear load-displacement curve after the inconsistencies from slack in the system. Fracture surfaces were analyzed with light optical stereoscopy, and SEM coupled with EDS gave higher magnification fractographs and elemental distributions for select samples.

#### **4.5.1 Lap Joint Microstructure**

One sample was made exclusively for microstructural analysis purposes and was not mechanically tested. Features of interest on the outside surfaces were imaged with optical stereography, SEM, and EDS. The sample was then sectioned transverse to the long axis, polished, and imaged with SEM and EDS again. The separate sample was created to elucidate diffusion behavior. The foil to make this sample was in the 200 to 250 micron thickness range. After the foil was ground to thickness using 180 grit sandpaper, it was polished down to a 1200 grit sandpaper surface finish. Once smooth enough, elemental distribution was measured with SEM and EDS. Having the direct comparison between brightness of phases in backscattered electron imaging and composition of the said phases from EDS allowed for identification of phases without EDS mapping. The imaged foil served as a brazing filler metal as the other foils. Parameters for this braze were 500 W beam power and 120 seconds of secondary raster time. Backscattered electron images and EDS maps of the foil analyzed are provided in Figure 4.31.

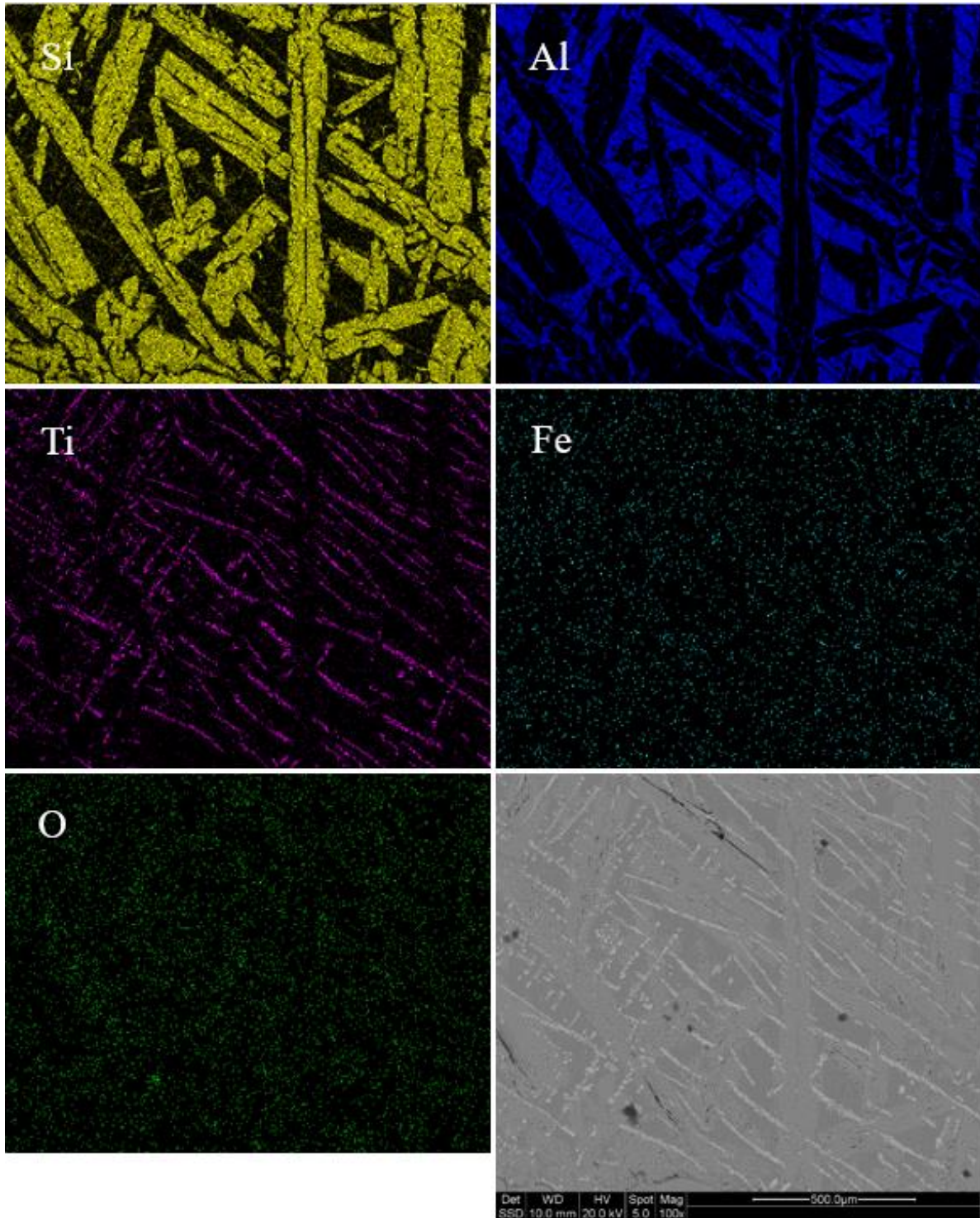


Figure 4.31 Labelled EDS maps of foil before brazing with backscattered electron image in bottom right corner

The EDS maps indicate that there was no iron present in the filler metal before brazing, proving iron must have come from the substrate. Slight oxidation existed but the oxide layer was not as developed in the filler as during and after brazing. Another image with the EDS maps overlaid on the backscatter electron image is included in Figure 4.32 to facilitate comparison of the EDS maps with backscattered electron imaging.

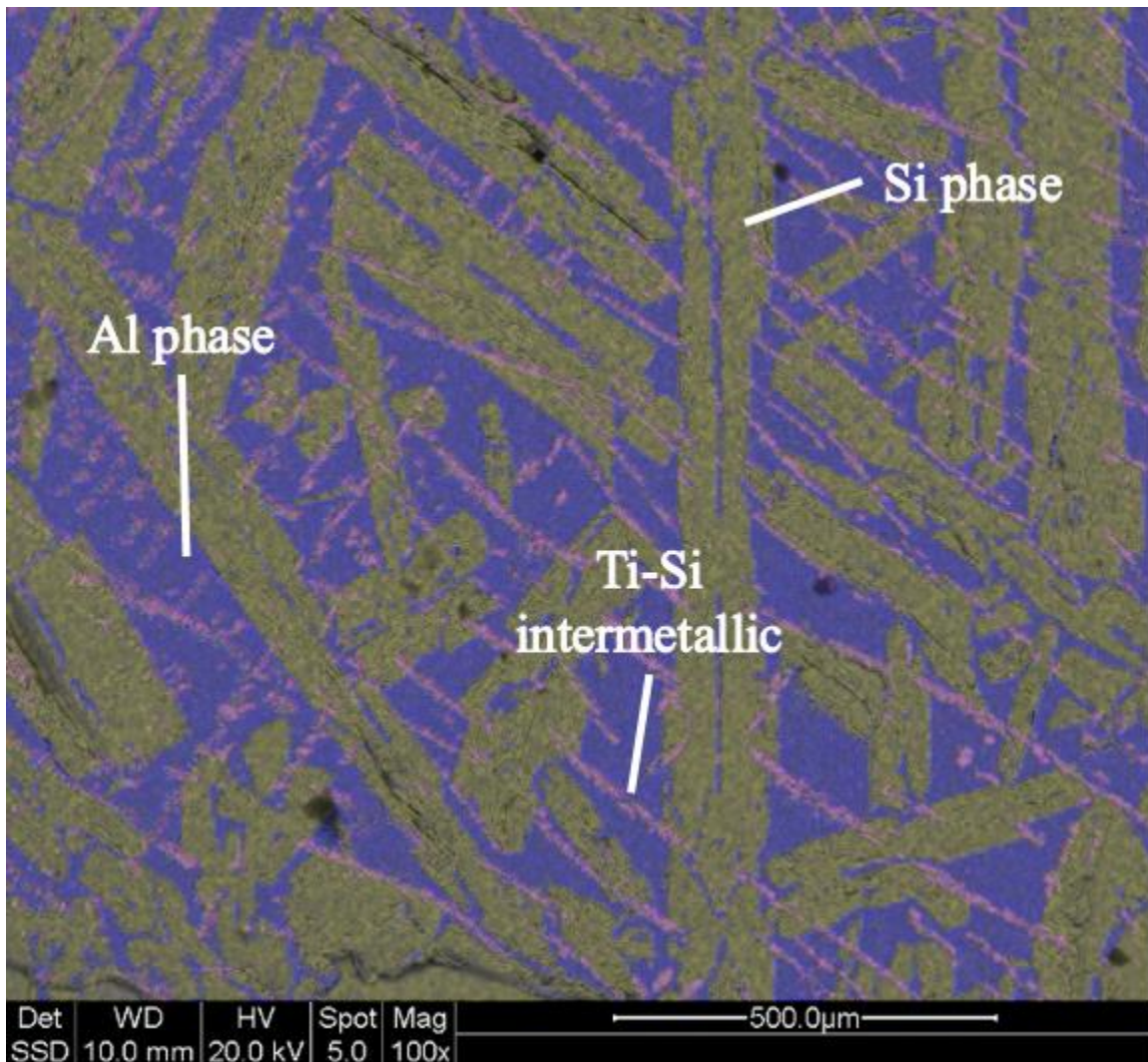


Figure 4.32 Comparison of overlaid EDS maps with electron backscattered electron image, with Si yellow, Al blue, and Ti magenta in the EDS maps

There is a clear overlap between the EDS maps and the backscattered electron image. Aluminum appears exclusively atop the darkest phase in the backscattered electron maps and titanium only appears atop the brightest phase. Therefore, aluminum is the dark phase in electron backscattered electron imaging. Silicon appears both in the phase of intermediate brightness and

in the brightest phase but with less intensity, indicating silicon appears both in a single phase and as part of the titanium phase. Based on the Scheil solidification sequence in Figure 4.20 the phase containing Ti and Si is  $TiSi_2$ . The  $TiSi_2$  phase may not be the actual phase formed, as  $TiSi_2$  is an equilibrium phase that may not have had time to form. The Ti-Si phase is almost certainly still an intermetallic compound either way, as the Ti-Si binary phase diagram contains many intermetallic compounds. A binary phase diagram having several intermetallic compounds indicates a large enthalpy of mixing between the two elements and high enthalpy of formation for intermetallic compounds.

These same phases with the same relative intensities in backscattered electron imaging are seen in the filler metal throughout wettability and lap joint testing. Filler metal in the lap joints is depleted in Ti and Al relative to the filler metal before joining, creating a higher concentration of silicon. More images were taken of the foil and analyzed with color thresholding in ImageJ to give area fractions for each of the three phases. Silicon is the dominant phase with 51 area %, Al has 36 area %, and Ti-Si intermetallic occupies 11% of the area. A backscattered electron image of the filler metal foil analyzed after being joined and sectioned is shown in Figure 4.33 to show the change in elemental distribution during brazing.

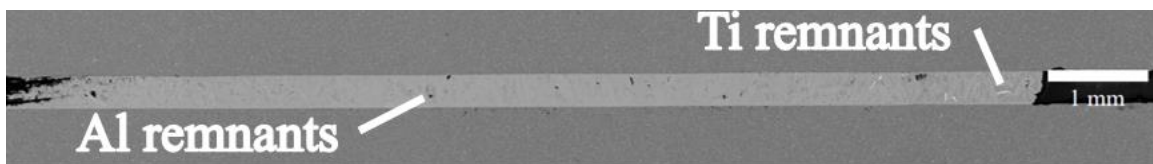


Figure 4.33 Filler metal foil analyzed by SEM and EDS after brazing

The filler metal preform initially covered the entire joint area, but diffusion has removed metal from gap leading to incomplete coverage. The out-diffusion also prevented fillet formation. Few light gray spots corresponding to Ti appeared in the filler metal after brazing – most of the Ti has disappeared. The dark gray spots corresponding to Al also almost disappeared. Diffusion into the substrate caused the Ti and Al depletion. Si increased to 86 area % after joining, and Ti dropped to below 1%. Al decreased to 20 area %, which is only a 44% loss compared to the over 90% loss of Ti in the joint. The solidification sequence and melting point are expected to be affected by Ti and Al depletion. Assuming changes in area fractions can estimate changes in atomic fractions, a new Scheil solidification simulation was performed with the estimated composition of the Ti and Al-lean filler and is represented in Figure 4.34.

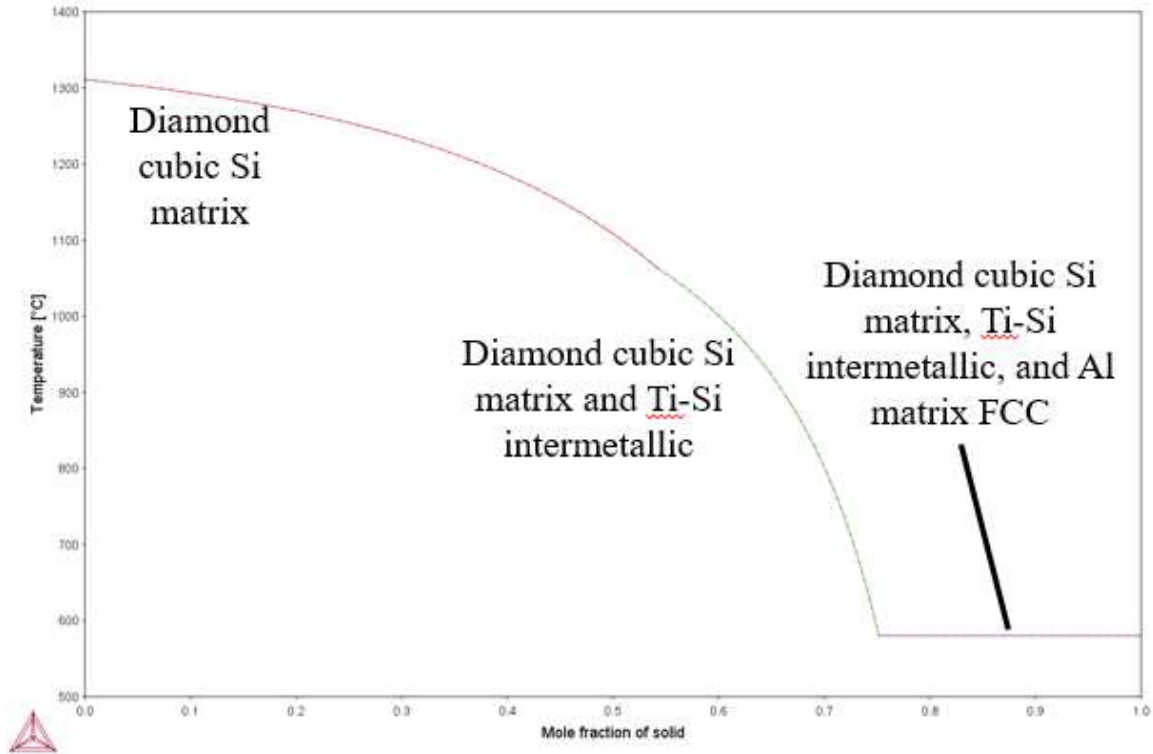


Figure 4.34 Scheil solidification simulation for Ti and Al lean alloy after diffusional losses

Equilibrium temperature for the onset of solidification would rise with the loss of alloy content. In this case the equilibrium liquidus temperature increased to approximately 1320 °C, which is 150 °C higher than the liquidus of the alloy before compositional changes. Increased holding times and temperatures resulting in more diffusional losses will eventually increase the melting point of the filler in the gap to 1414 °C, the melting point of pure Si. Increasing the liquidus during joining by diffusing elements into the substrate is a technique fundamental to transient liquid phase processing. This concept somewhat applies for this scenario, except the introduction of Ti and Al impurities into the RB-SiC is deleterious to mechanical properties.

#### 4.5.2 The Diffusion Affected Zone (DAZ)

Like the wettability testing results, the depth of the diffusion affected zone was on a similar scale to the thickness of the RB-SiC coupons. Diffusion through the joint was visible, including in the joint sectioned for microstructural analysis. Again, this depth of diffusion was only possible because of the melting of the free Si in the RB-SiC during processing. The diffusion coefficient for Al in Si at the melting point of Si is approximately  $3E-10 \text{ cm}^2/\text{s}$  and the diffusion coefficient for Ti at the same temperature is around  $9E-8 \text{ cm}^2/\text{s}$  [64]. Pipe diffusion is

faster than bulk diffusion in Al, with a diffusion coefficient of  $1E-7 \text{ cm}^2/\text{s}$ . Using Einstein's approximation equation for diffusion and a length of an eighth of an inch gives a required time of almost six days for pipe diffusion of Al. The actual time would be even longer, as there is tortuosity in the free Si path. Liquation in the free Si is therefore the only explanation for how diffusion depths exceeding three millimeters are found. There is also some measure of convection in the free Si due to the thermal gradients intrinsically created by laser heating which increase the mass transport rate. Figure 4.35 shows the elemental maps for Al and Ti on either side of a backscattered electron image through the thickness of the substrate to explicitly show the diffusion.

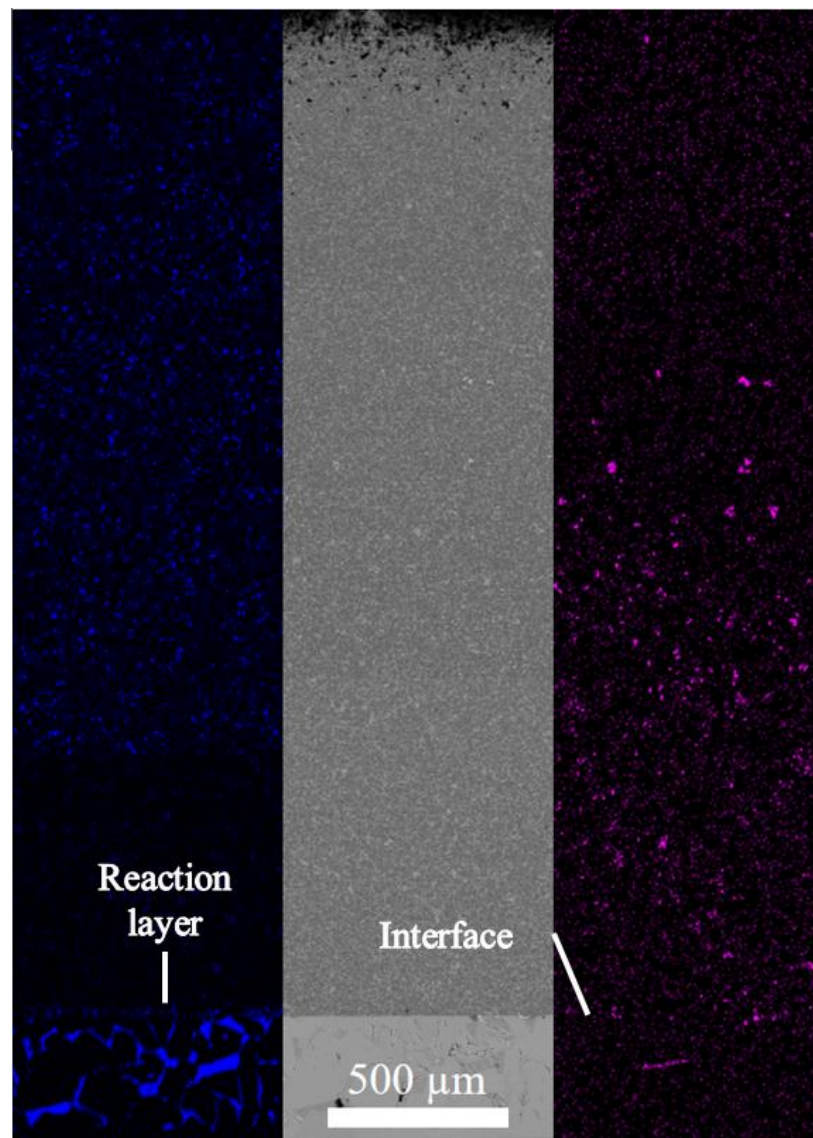


Figure 4.35 Backscattered map (middle) with Al (blue) and Ti (magenta) EDS maps of diffusion

The Al map shows a region of decreased intensity because EDS mapping is not truly quantitative and instead normalizes the signal by the most intense region. There is enough Al in the gap to overwhelm the signal from the Al diffused into the substrate and make the substrate appear as if there is a lower concentration of Al due to normalization. Contrarily, Ti does not experience this behavior because so much Ti has diffused into the substrate that the concentration difference between the substrate and filler is small. Both elements can be seen diffusing all the way to the substrate surface. Ti can be seen in the backscattered electron images as well as in the brighter spots dispersed throughout. Al is more difficult to distinguish because it does not have as great of an atomic number difference with Si. Another difference between Ti and Al diffusion behavior is the appearance of the filler-substrate interface. The EDS map for Al shows a reaction layer formed at the interface. The presence of this layer agrees with thermodynamic predictions, as Al has a higher affinity for carbon than Si. Titanium at the filler-substrate interface has formed islands of interaction zones but is not continuous like the aluminum-substrate interaction layer. The large amount of Ti diffusion into the substrate causes too little Ti to remain near the interface to develop a continuous reaction layer.

Solidification behavior and adhesive strength are both changed by the distribution of Ti in the reaction layer. Wettability between the remainder of the Si-rich filler and each interaction layer differs. Since nucleation in solidification almost always occurs heterogeneously, having an aluminum carbide layer instead of a mixed titanium carbide and Ti-Si intermetallic layer could change the amount of undercooling needed for solidification to begin by modifying the interfacial energy requirement for nucleation. Changes in interfacial energy will also alter strength because adhesive strength is directly related to interfacial energy. Fortunately, Si wets and nucleates on the substrate surface as altered by Al, as represented by the lack of voids on the interface. Al which has not diffused out of the filler metal also reflects this phenomenon by the presence of Al in the middle of the filler instead of the substrate-filler interface. If Si was not able to wet to the altered substrate surface then Al would appear on the surface instead, but Al appears in the last region to solidify indicating Si nucleated and solidified first as predicted by Scheil simulation.

Filler metal diffusion through the thickness of the substrate coupons also creates features external to the surface similar to those seen in the wettability sample given a prolonged

secondary raster. As in the wettability tests, penetrating diffusing filler metal adhered to the silica fixture. Figure 4.36 shows a feature developed on the outside surface of the lap joint made for microstructural investigation after transverse sectioning.

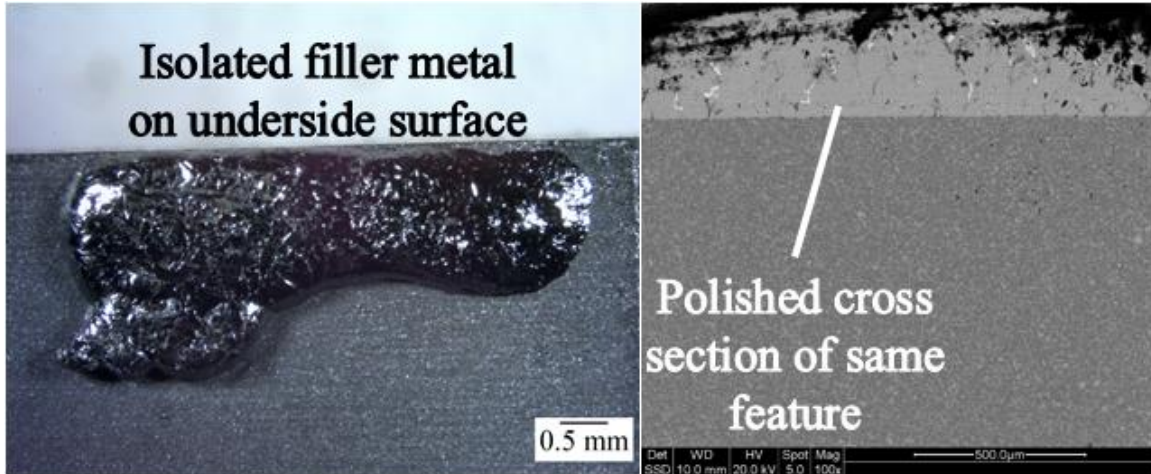


Figure 4.36 Light optical stereoscope image of through diffusion of filler metal on surface and backscattered electron image of transverse section through the external feature

External features such as those in Figure 4.36 can come from one of two sources. Filler metal may have overflowed the gap and stopped here, on the underside. However, there is no trail leading from the gap to this feature on the underside. It is possible that there was a trail but it diffused into the substrate, but no other samples with filler metal on the underside have such a trail.

Another potential cause for features like those in Figure 4.36 is filler metal diffusion through the thickness of the substrate. This possibility is the preferred explanation, as a feature such as those present in Figure 4.36 was seen in wettability testing where the metal had no chance to flow down the outside of the substrate. Support for this theory is also provided by the EDS maps and backscattered electron images shown in Figure 4.35. In both theories, some of the mass of the external feature is provided by free Si and the impurities originating from the sample. Proof lies in the iron found in some of these features. The EDS maps in Figure 4.31 show no measurable amount of iron in the filler metal before brazing, indicating the iron in the surface features must have come from the substrate. Free Si merging with the surface features created by the filler metal is sensible, as the alternative for free Si exuded by the substrate is to create surface beads. Surface beads have a higher surface area to volume ratio than a larger

globule, and thus have surface energy and total free energy. Joining the larger features reduces their surface energy and consequentially lowers the free energy of the system; this is known as the Gibbs-Thomson Effect.

### 4.5.3 Overflows

Surface features comprised of filler metal might not have been created exclusively by diffusion. Filler metal also flows out of the gap during joining and solidifies on exterior surfaces. If enough metal flows out to contact the surface of the silica fixture, then it will bond with it. Though not within the scope of the project, this phenomenon indicates the filler metal may also see success in joining silica. This is unsurprising, as Ti and Al both have a higher affinity for oxygen than Si. Thus, wetting and joining would be possible as defined by the principles of active metal brazing. Figure 4.37 shows an overflow feature that unintentionally brazed to the silica fixture.

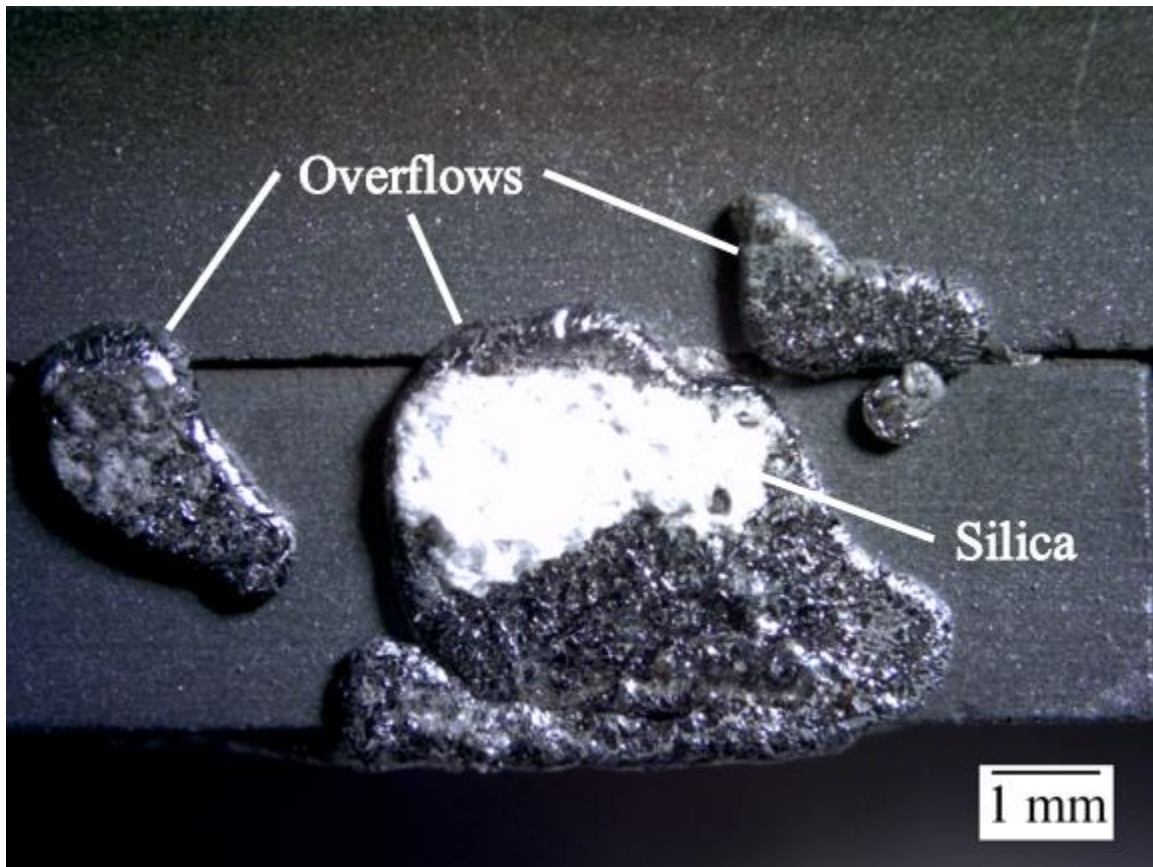


Figure 4.37 Overflow feature which unintentionally brazed the silica fixture, 400 W, 120 s secondary raster, and 200 to 250  $\mu\text{m}$  foil

Overflow did not correlate with any of the controlled variables, namely beam power, secondary raster time, and foil thickness. They were examined to determine why they would form. Filler metal may be pushed out of the gap by the weight of the substrate, and once outside of the gap, it is prompted to flow by capillary action between the substrate and silica fixture as well as gravity. The surface tension of the liquid filler metal will act to hold it within the gap. Comparable to wettability testing, even the low partial pressures of oxygen during joining are enough for oxidation. The outer surface of the filler metal once again consists of a mixture of oxides. Oxide composition is disproportionately aluminum oxide due to the high affinity of aluminum for oxygen. The largely solid oxide layer has greater mechanical strength than the liquid and acts as a sort of dam preventing outward flow from the gap. For the liquid metal to flow, the oxide dam requires either a large enough force to break through or something to weaken the dam.

The oxide layer containing the liquid filler also explains the general morphology of the overflows. Rather than overflowing the gap everywhere, filler metal locally begins to overflow locations where the dam breaks and creates an overflow feature. If surface tension was the force preventing overflow and not the oxide dam described filler metal would not be constricted to overflowing in specific points. To determine if the force of gravity and the weight of the filler had an influence in causing the breakthrough of the oxide dam, a sample was brazed with filler metal introduced as a cuboid of equal mass to the foils. Beam power was 500 W and secondary raster time was 180 seconds. Introducing filler metal as a cuboid increases the effect of gravitational forces by having a greater height of liquid metal to create greater metallostatic pressure and increasing the distance that the RB-SiC coupon (on top of the filler) can move downwards. Increased movement distance would allow the coupon to fall and push the filler outwards. Figure 4.38 shows the overflow behavior for the sample with a cuboid of filler metal.

Filler has overflowed the gap in a general region instead of the localized points seen when the filler is introduced as a foil. The increased effect of gravitational forces was enough to break through the oxide dam over a larger region and allow for overflow. Gravity, when deliberately amplified using a cuboid filler, was able to cause widespread rupture of the oxide dam. Under normal brazing conditions, gravity was not observed to cause similar amounts of breakthrough, which means the oxide dam is likely weaker at the breakthrough points.

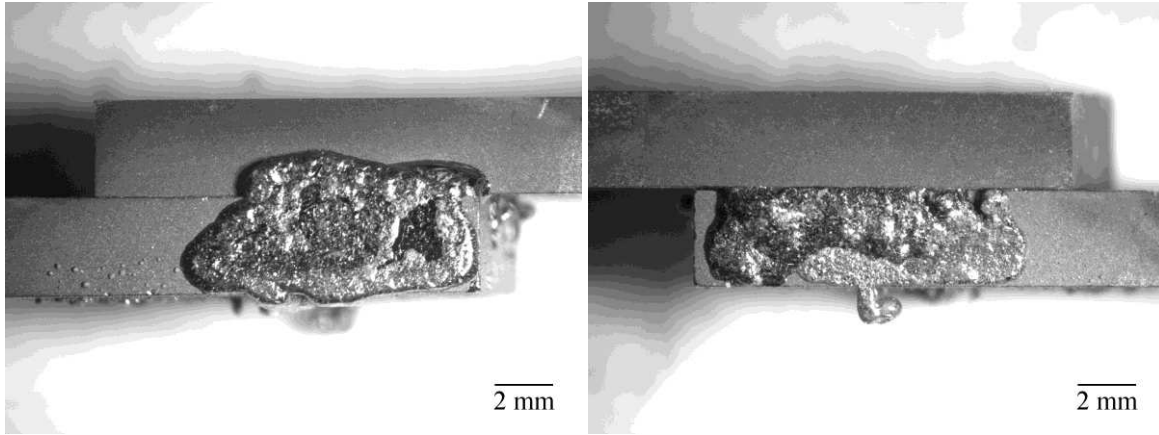


Figure 4.38 Overflow behavior in sample with filler introduced as cuboid instead of foil

Weak points on the oxide skins may be caused by chemical differences. Iron is known to infiltrate the molten filler metal, and Fe may also be incorporated into the oxide layer. To facilitate the development of how Fe may weaken the oxide layer, one can consider the oxide layer as a flux layer in welding or steel processing. When discussing fluxes, the basicity index is one of the primary parameters of interest. Tuliani's equation, a common formula describing the basicity index as a function of flux composition [65], is expressed in Equation 4.4.

$$BI = \frac{CaO + CaF_2 + MgO + K_2O + Na_2O + Li_2O + \frac{1}{2}(MnO + FeO)}{SiO_2 + \frac{1}{2}(Al_2O_2 + TiO_2 + ZrO_2)} \quad (4.4)$$

The oxides in the denominator are described as acidic and those in the numerator are basic. A higher basicity index signifies a more basic flux. Acid fluxes generally exhibit high viscosity while basic fluxes will see increased fluidity. Since the filler metal is made of Si, Al, and Ti, the reaction of these elements with oxygen will form oxides that go into the denominator. Consequently, the basicity index of the resulting oxide layer formed during brazing of RB-SiC with the Si-Al-Ti filler will be close to zero. That is, the oxide will only flow very sluggishly, giving the protrusion and overflow appearance. Oxidation of pure SiC will not change the basicity value. Nevertheless, iron additions to the oxide layer from the RB-SiC substrate are expected to weaken the oxide dam because they raise the basicity index. With increasing basicity, the liquid oxide tends to be more fluid, creating opportunities for breakthroughs. There may also be a melting point effect as the melting point of iron oxides ranges from 1377-1565 °C depending on the degree of oxidation. Even in the coldest samples, the steady-state temperature

was above 1500 °C. Figure 4.39 shows a backscattered electron image and EDS map where two overflows only conjoined where iron was present.

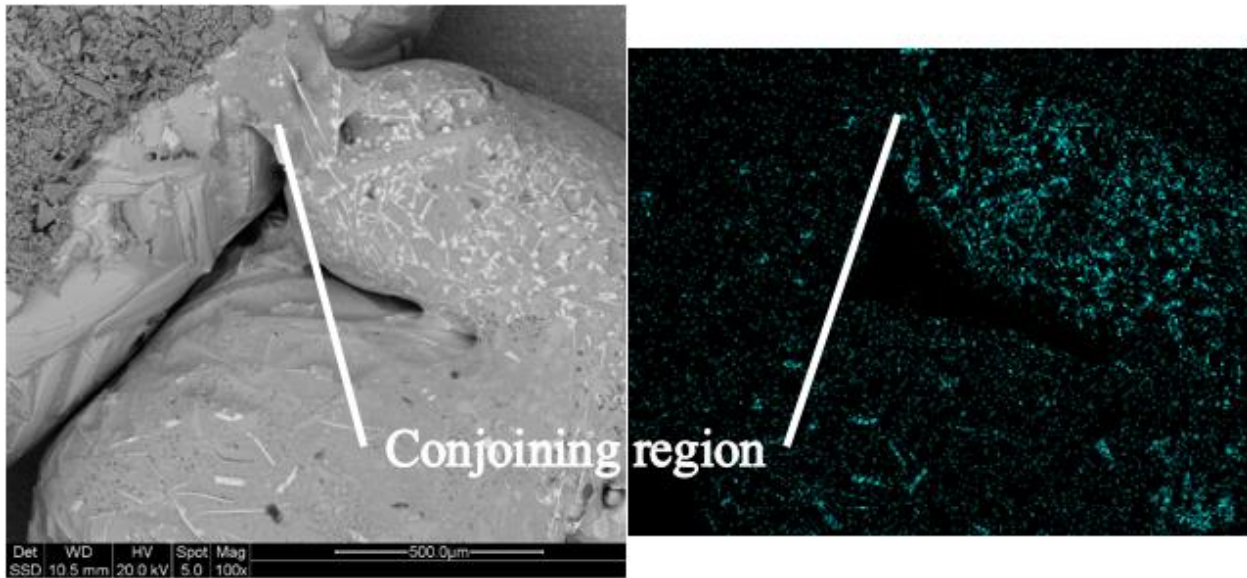


Figure 4.39 Electron backscattered electron image of overflow with EDS map showing conjoining of overflows only where iron is present

Iron is rarely found in the gap itself because it is carried away with the overflows when they occur or never incorporated with the filler. No iron was detected in the gap in the sample prepared specifically for microstructural analysis. Minor amounts were detected in the gap in a sample made as part of a preliminary study to determine what laser powers were needed. The iron found in the gap in that experiment is likely only there because it did not have adequate time to migrate towards the edges and remain there. This explanation is supported by the higher amounts of iron towards the surface as compared to the middle of the gap. Iron impurity concentration in the RB-SiC substrate was not controlled. The effect of iron on overflow behavior was not discovered until many joints had already been made, and there remains no good way to detect it before joining regardless.

Per discussion presented, iron may be the main cause of the oxide dam weakening, but forces from gravity are not the only forces capable of breaking through the oxide dam. Unlike wettability testing, temperatures achieved during preheating are enough to melt both the RB-SiC substrate and the filler metal. Temperatures in the joining region are higher during the secondary raster than the preheat raster because the secondary raster is more localized. Preheat raster temperatures still exceed the melting point of the free Si, which is above the melting point of the

filler metal. Preheat raster temperatures being lower allows for solidification to occur during the five second pause to lessen thermal gradients between the two rasters. Figure 4.40 shows the thermal data for a sample given a 400 W beam with a 200 to 250  $\mu\text{m}$  foil thickness.

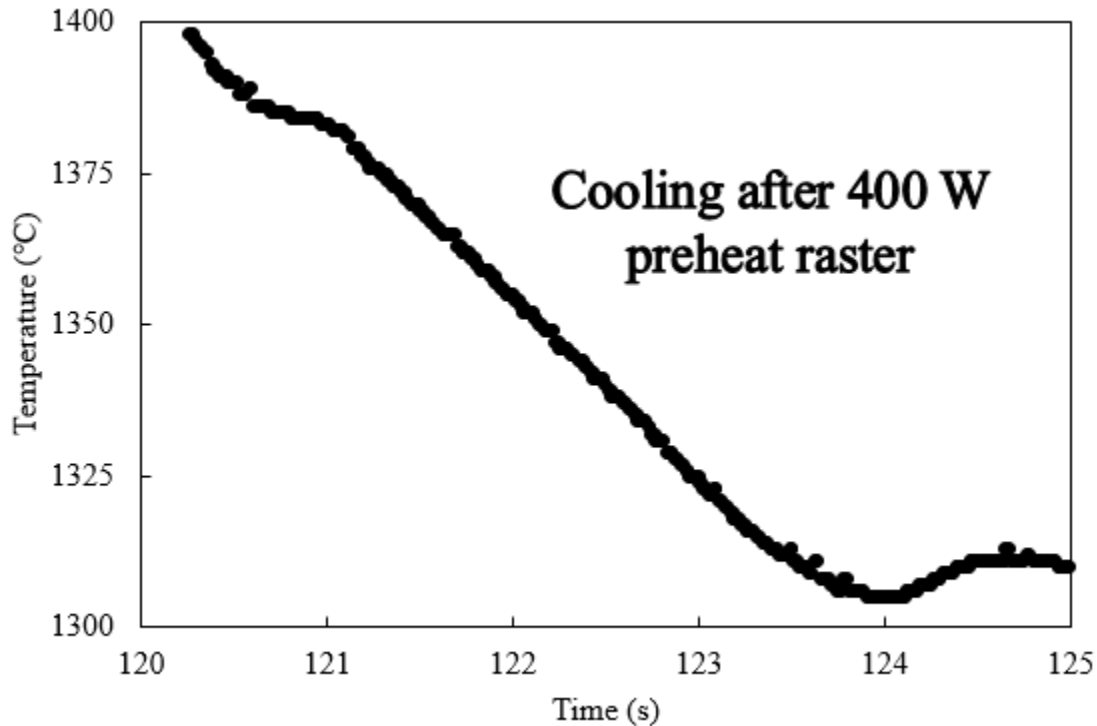


Figure 4.40 Thermal response of sample given 400 W during five second pause between rasters

In this figure, the laser beam was not operating at any point along this graph, so the increase in temperature at the end, around 1305 °C, must be due to solidification. Samples brazed with a 600 W beam, the highest power, also show an inflection point from solidification. As silicon solidifies and expands, the pressure exerted by Si solidifying can break through the oxide dam. Temperatures do not reach a low enough value for complete solidification, so liquid can either begin flowing through the break in the oxide layer during the five second pause or begin flowing when the beam resumes supplying heat during secondary rastering.

Despite the existence of overflows and the DAZ having a similar depth to the sample thickness, filler metal does not appear on any surface experiencing direct laser radiation in large amounts. This observation includes the fillet region, especially on the side opposite that receiving laser radiation. Even though the laser beam does not completely prevent any filler metal from existing on the surface, it does appear to severely limit the quantity. Small amounts

of filler metal on the surface may also appear due to Si expansion during solidification squeezing metal droplets out; the same mechanism is responsible for some of the beads exuded that do not join the filler metal. Solidification expansion was enough to create a “false fillet” in some samples, where metal appeared to be a fillet at first glance but was not contacting either surface. Figure 4.41 shows an example of this phenomena.

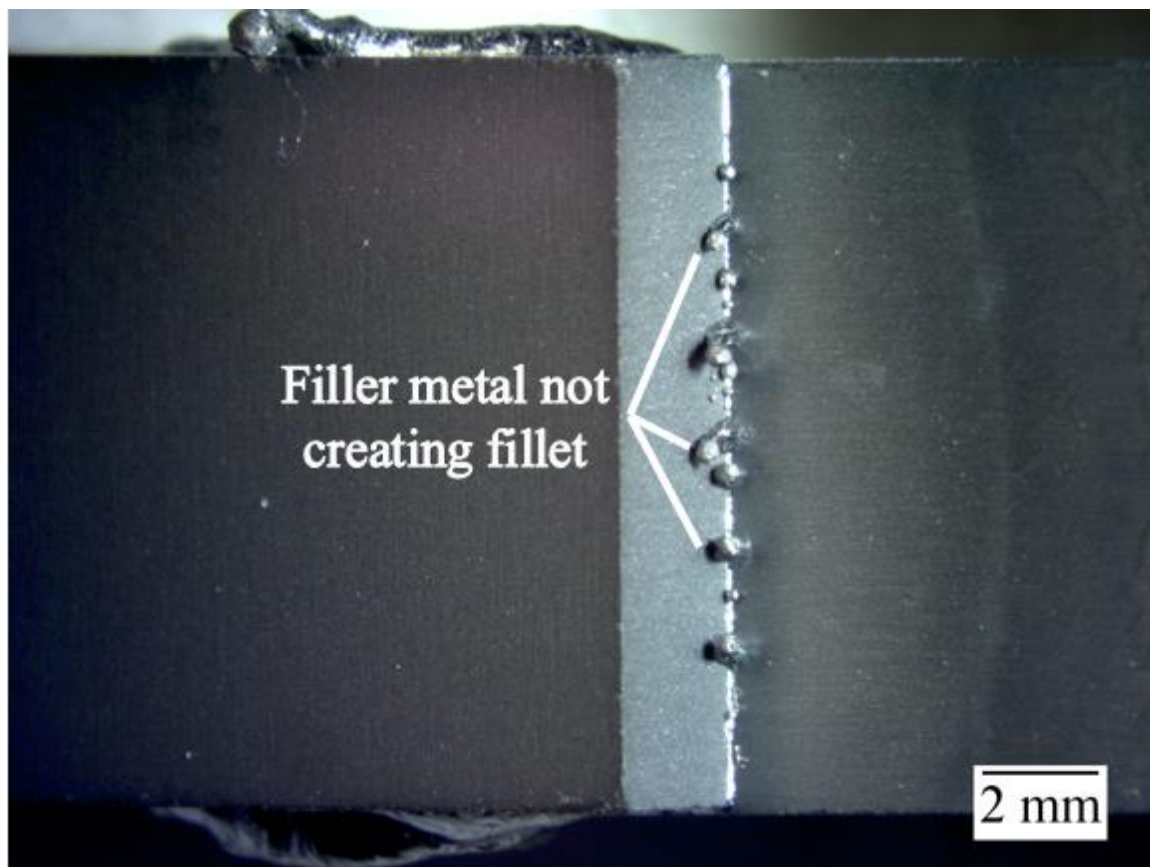


Figure 4.41 Filler metal that expanded during solidification and occupied the area where a fillet would be without forming a true fillet

These false fillets do not reinforce the joint in the way a true fillet does. They form during solidification because there are cases where the filler metal begins to form a fillet but is then heavily oxidized by extreme heating from the beam. Vaporization may also occur when the beam impinges directly upon the filler. Deposition of the vaporized species was never detected within the chamber because the quantities are expected to be low. Conversely, observing heavily oxidized filler metal with the beam impingement is much simpler. Samples were tilted to seven degrees to view the fillets. Figure 4.42 shows a backscattered electron image and EDS map for oxygen of a sample which failed to form a fillet.

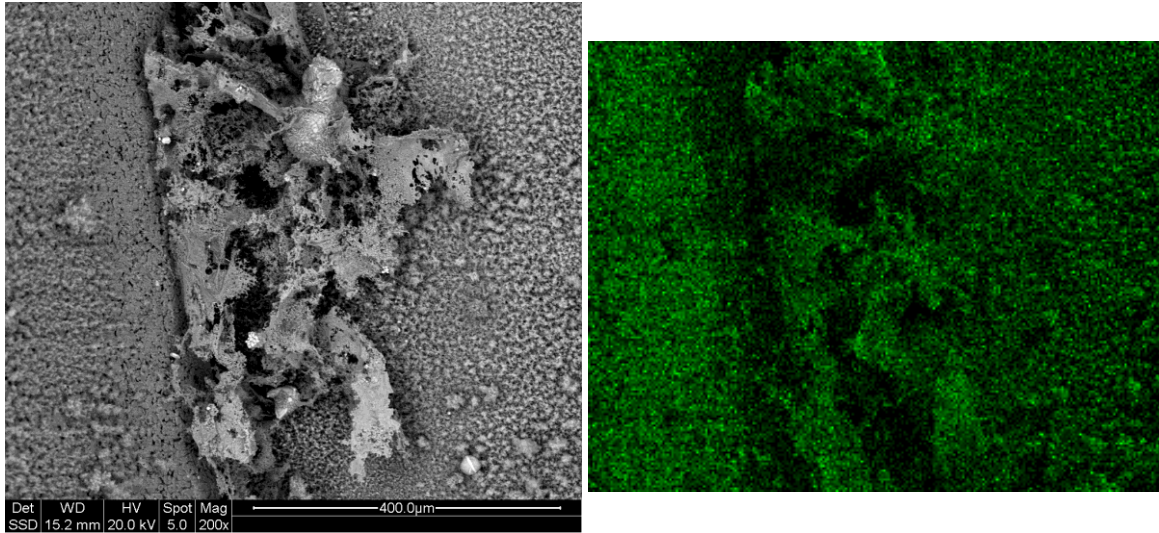


Figure 4.42 Fillet formation prevented by oxidation

A fillet as in Figure 4.42 is inadequate for bearing load. The EDS map also shows the substrate surface is oxidized, a combined result of Al diffused to the substrate surface oxidizing and oxidation of the RB-SiC itself. Some Ti is present as oxide on the substrate surface but not in as great an amount due to its lower concentration in the filler metal.

#### 4.5.4 Oxidation in Lap Joints

Clearly, oxidation still poses a concern despite the low concentration in the atmosphere. Additionally, oxidation prevents fillet formation and oxidized species will create high angle triple points/lines. Oxidation directly affects fillet formation and deteriorates mechanical performance. Oxidation also influences overflow behavior. Three viable methods to resolve the oxidation issue include: further decreasing  $O_2$  concentration, implementing some form of detachable flux to protect the filler metal, or adding a reducing gas to the atmosphere. Besides a vacuum system, the only way to reduce  $O_2$  concentration is with Ar gas with even greater purity. The Ar gas used in this work was 99.999% pure. A six nines Ar gas will bring the oxygen level to one ppm. However, oxidation is still thermodynamically favorable in this environment. It appears that designing a flux system or adding reducing gases are the only remaining options in enhancing the wettability of RB-SiC with Si-Al-Ti filler. Reducing gas serves as a better solution because of simpler implementation. Developing a flux system is near the boundaries of the project scope.

As described earlier in this chapter, there were three trials with an Ar-H mixture atmosphere. Oxidation was slightly mitigated, but the same oxidation effects as in pure Ar atmosphere experiments were still present. The largest difference seen was in fillet development. A fillet of significant volume developed in the sample given only an Ar-H atmosphere. The sample still showed signs of oxidation, but some of the surfaces appear to be metallic or covered in a thin transparent layer of oxide. Figure 4.43 shows the fillet.

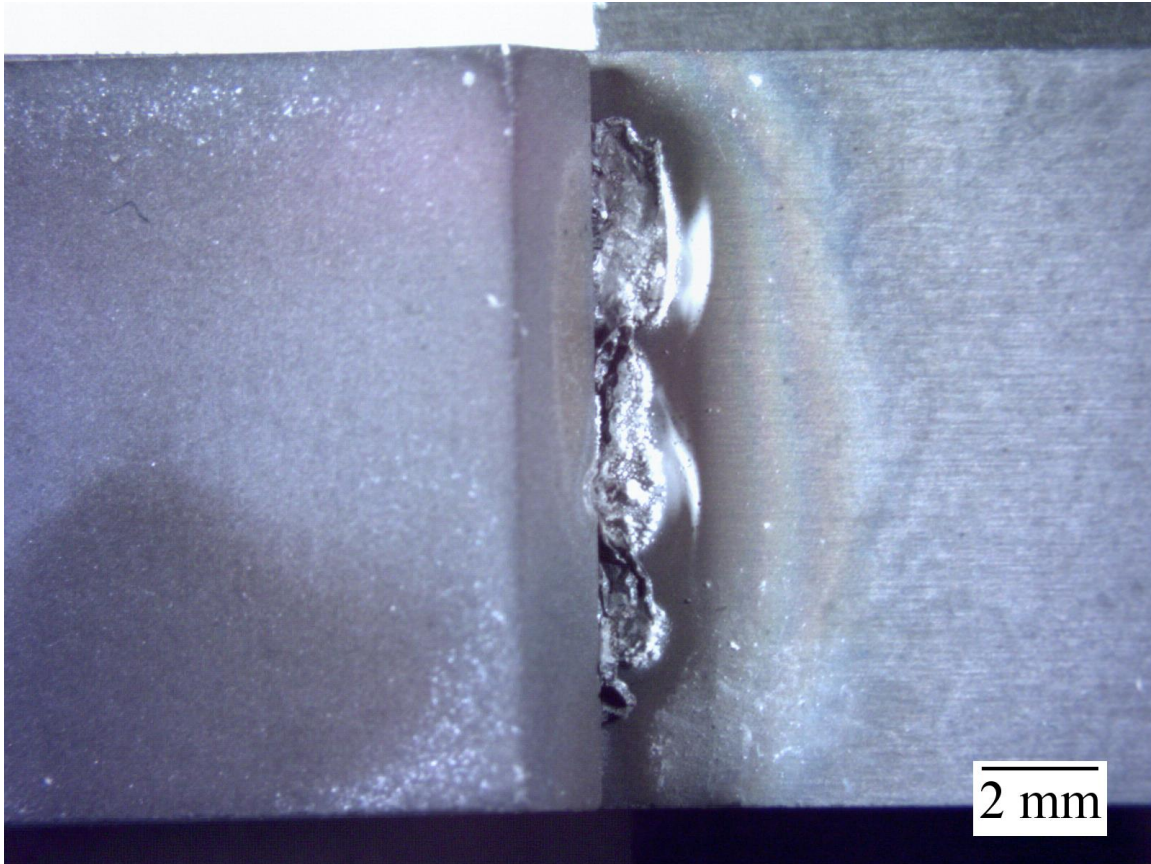


Figure 4.43 Fillet developed in sample made exclusively with Ar-H gas

While the volume of metal flowing out of the gap is sufficient to cover the entire surface, the filler metal did not cover all the empty space. The filler metal also failed to flow upwards along the vertical surface. Though limited compared to other samples, the oxidation was enough to prevent proper spreading of the filler metal. This indicates the amount of hydrogen gas in the mixture was insufficient. Increasing hydrogen gas would be the obvious solution, but flammability begins to be a concern. Carbon monoxide could function as a reducing gas as well but has well known health concerns.

#### 4.5.5 Fractography

Fracture surfaces for failures in the joint do not have filler metal covering the entire faying surface. The filler metal preforms placed ensured the entire surface is covered, so filler metal must have been lost somehow. Diffusion as the cause of filler metal loss was confirmed in a sample made with a 600 W beam, 180 second secondary raster, and a 200 to 250  $\mu\text{m}$  foil. This sample was optimal to show the diffusional loss mechanism for gaps in the filler, as these parameters create the highest temperatures for the longest times out of any raster parameters with the thinnest foil. Figure 4.44 shows the fracture surface of the sample just introduced.

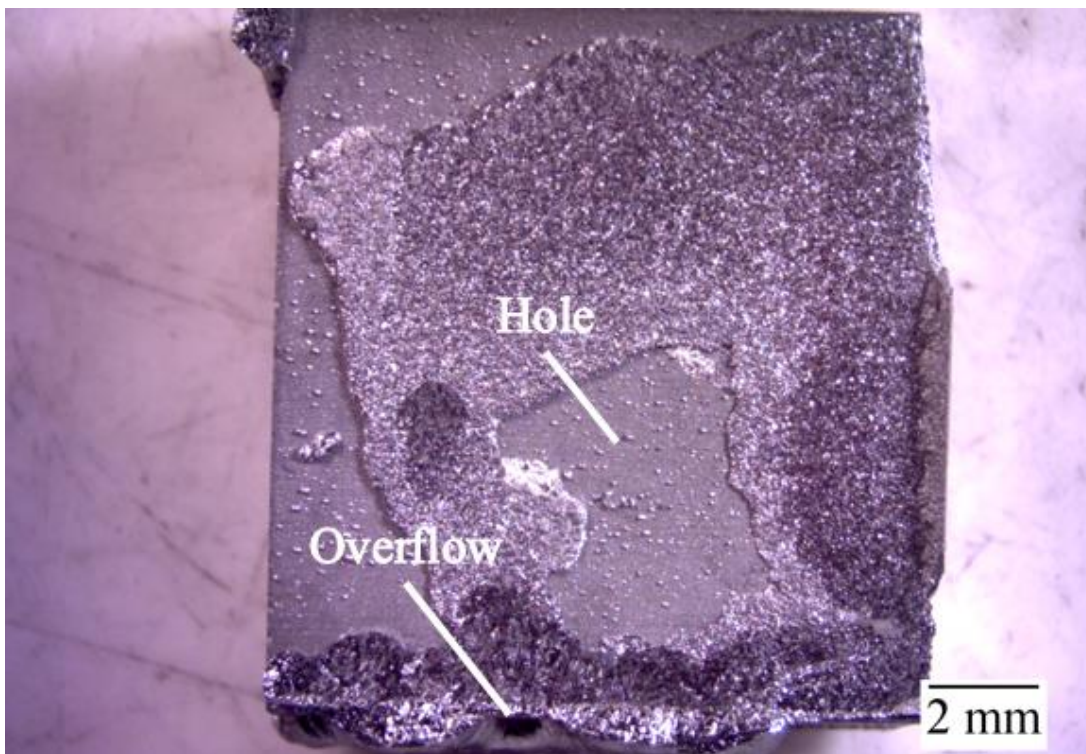


Figure 4.44 Fracture surface with filler metal coverage gap in the middle of the foil preform

Gaps along the edges of the filler metal could be caused solely by the actions of overflows, but a gap in the middle of the filler metal is not so easily explained by overflows. Creating a hole in the middle of the molten filler requires creating more surface, which requires more surface energy. This process is a lower free energy path for overflows to cause the filler metal to retreat from the initial faying surfaces in an edges-to-middle path than creating a hole. Generating a hole in the middle is more easily explained by diffusional losses. To confirm diffusion as the mechanism for creating this hole, EDS scans were taken of the substrate region

in the middle of the hole. If diffusion is the cause of the metal lost here, filler metal elements should still be detectable. Figure 4.45 shows the EDS scans and electron backscattered electron image of the middle of the hole.

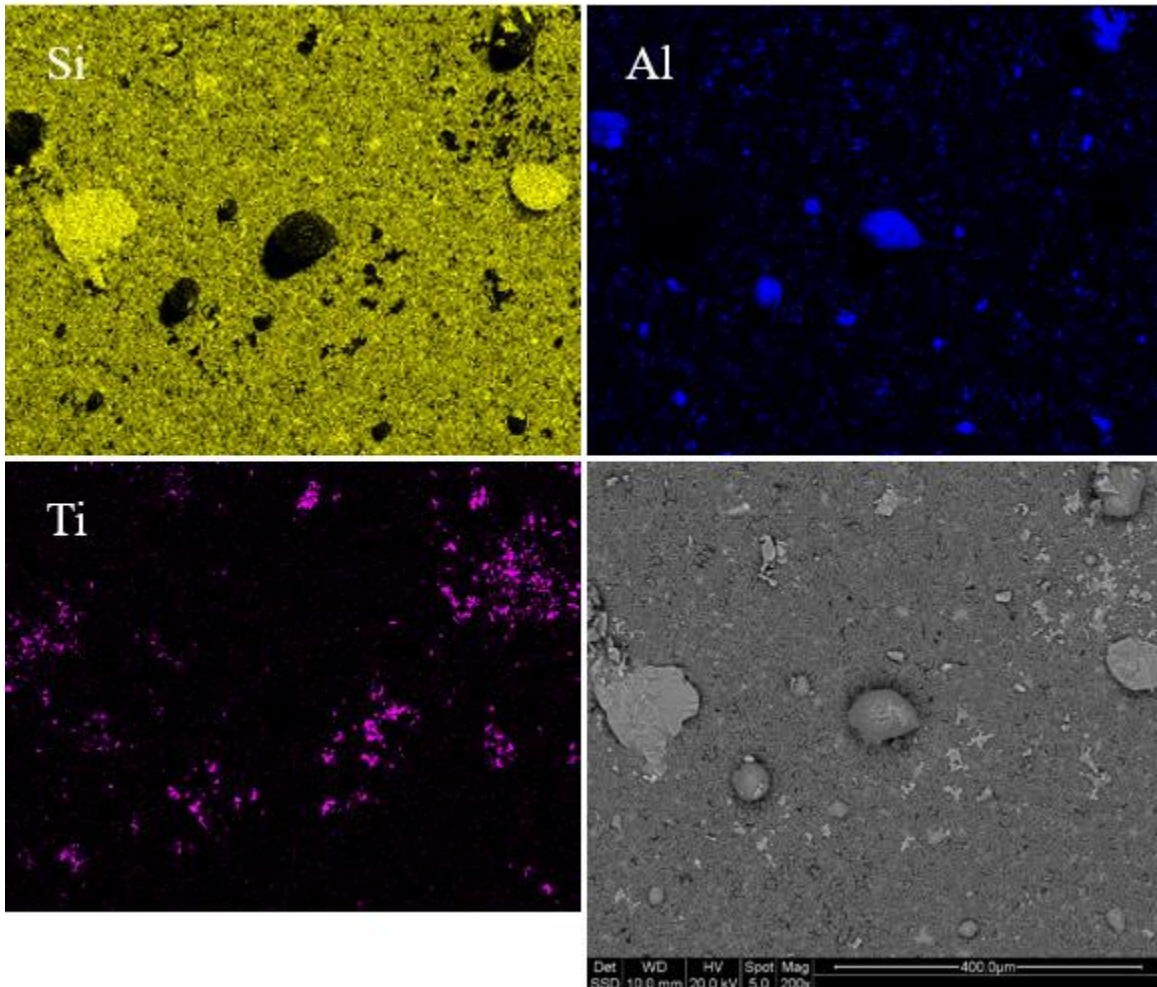


Figure 4.45 EDS maps and backscattered electron image of holes left behind by filler metal diffusion

These images prove filler metal diffused into the substrate which is not readily seen in the optical images. The optical images do show beads in the hole, and those are shown here as well. Bead chemistry in the hole differs from beads exuded by the substrate because the former is the result of filler metal not yet completely diffused into the substrate rather than free Si from the substrate. Surface beads from areas within the DAZ can contain filler metal elements. Titanium is an exception to the bead formation seen. Rather than forming a surface feature like Si and Al do, titanium will diffuse through the free Si or exist within another bead, but never as the

dominant component in a bead. Titanium is a highly reactive metal and existing on its own is a higher energy state than bonding with the other elements present. Thus, Ti will exist exclusively as compounds with other elements, the only exception being when it is a liquid.

Oxidation was another issue within the gap itself. Oxidized metal loses strength and can also create geometries increasing stress concentration by restricting the flow of filler metal. Three different states of oxidation were seen inside of the gap. In the least oxidized state, the metal remains shiny and metallic in nature but covered with a thin transparent oxide layer. The layer may be formed during brazing or after opening the atmospheric control chamber when the samples are cool enough to touch. All three elements in the filler metal form passivation layers, so the thin oxide layer is both unavoidable and desirable. The next most oxidized state begins to produce a color change on the filler metal surface, but the surface remains reflective. This layer was rarely seen. More common was the third state of oxidation, wherein the filler turns a dark gray color. Oxide such as this is responsible for most of the effects discussed earlier in this paragraph and is not desirable. Figure 4.46 shows a light optical fractograph of a sample showing all three levels of oxidation with labels.

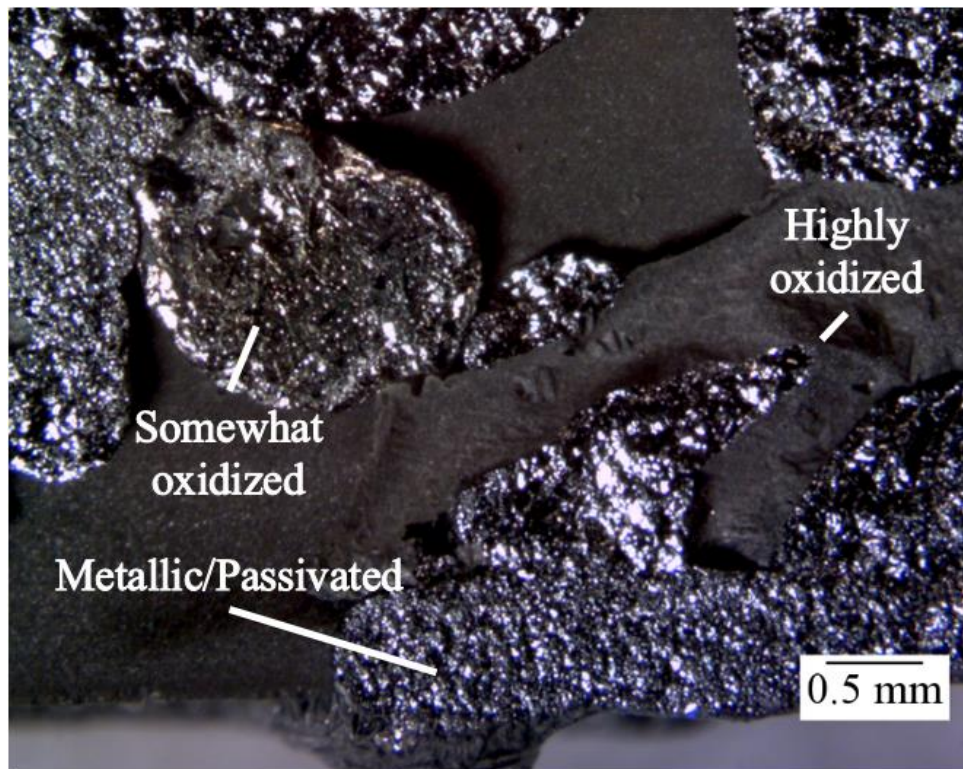


Figure 4.46 All three states of oxidation found within fractures surface, labelled

There is another level of oxidation above the region labeled as highly oxidized. However, this level is only found in the regions where a fillet would otherwise have formed and not within the gap itself. Having already been discussed, this level is not mentioned again.

Not every sample experienced failure within the joint. Some samples only experienced fracture in the substrate, and some experienced fracture in both the substrate and the joint. Samples which experience fracture in the substrate but remained in the fixture under increasing load until another fracture ending the test. Out of all the joint mechanically tested, 28% failed in only the joint, 28% failed through the joint and substrate, and the rest failed in only the substrate. Samples failing in the substrate were the strongest, and samples failing in the joint were the weakest. Table 4.3 shows the shear strength and standard deviation in the shear strength for the three failure modes.

Table 4.3: Shear strength and standard deviation for all the failure modes

|                           | <b>Joint</b> | <b>Both</b> | <b>Substrate</b> |
|---------------------------|--------------|-------------|------------------|
| <b>Strength (MPa)</b>     | 6.1          | 8.0         | 10.9             |
| <b>Standard Deviation</b> | 2.0          | 2.4         | 3.6              |

Experimental results for substrate failures in brazed joints experiencing the highest strength is reflective of what is reported in the literature. It is typically accepted that a good joint is as strong or stronger than what is being joined. The numbers in Table 4.3 were calculated against the nominal half-inch square faying surface area. However, the actual area of filler metal is less than the nominal value due to the previously discussed losses. Therefore, the calculated strengths included uncertainties caused by different faying surface areas.

Failure in ceramics and brittle materials is defect-controlled, and laser processing introduces multiple defects. These include contamination from filler metal elements and porosity from loss of free silicon, especially on the surface. Some amount of bending moment is always present in shear testing due to the thickness of the part being tested. Bending moments create the maximum tension on the outside edge of the material, where surface porosity created by the extreme temperatures promote free Si loss. Failures caused by bending lead to cantilever curl in

the broken part, wherein the fracture surface curves. Figure 4.47 shows some examples of cantilever curl for the substrate and both type failures.

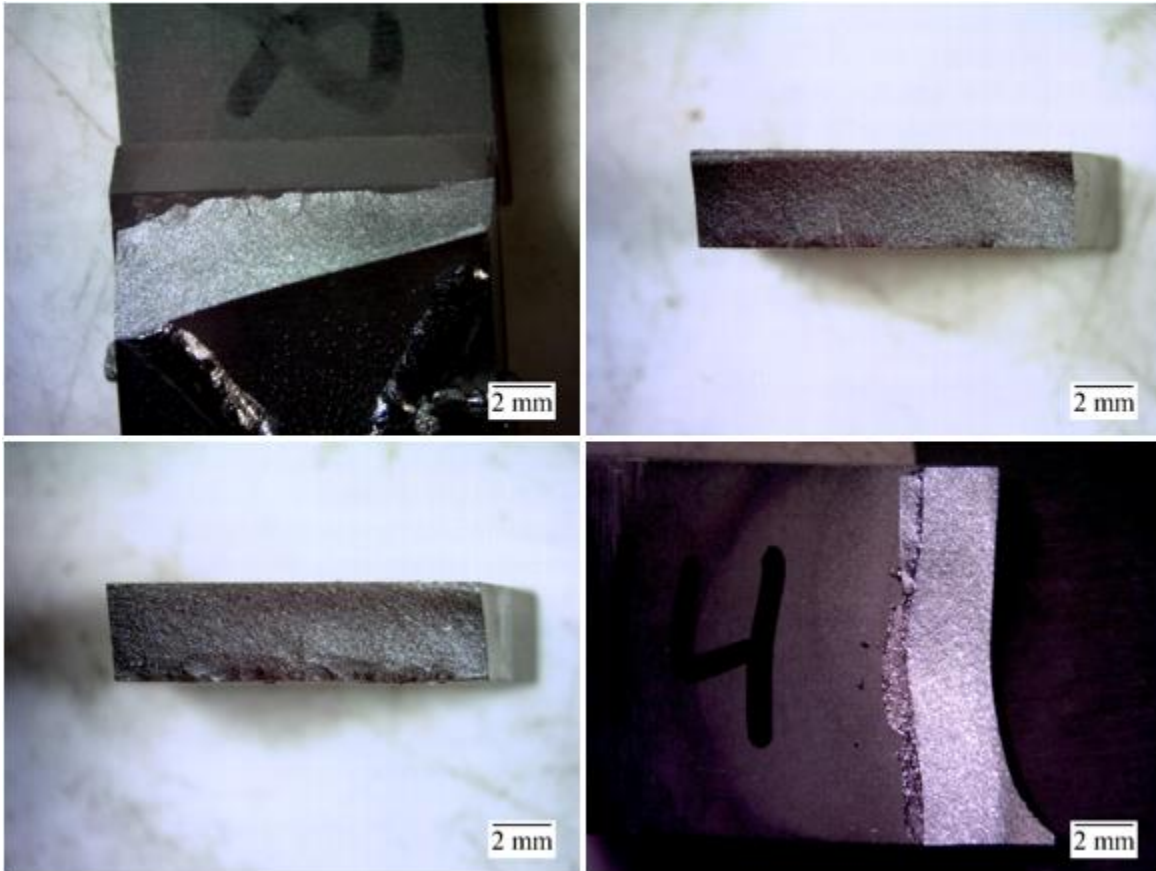


Figure 4.47 Cantilever curl in fractured samples

High variability is reflected in the samples which fractured through the joint. As the filler metal is brittle and brittle fracture is controlled by crack initiation, variability in measured strength is expected. Increased magnitude of variability was caused by the inconsistent behavior of the filler metal within the gap, namely inconsistent oxidation and the morphology of the metal left behind after diffusion and overflow losses leading to sharp corners. Additionally, filler metal flow behavior is influenced by impurity content of the RB-SiC substrate which is an uncontrolled variable, further scatter in strength data is expected.

#### 4.5.6 Shear Strength

Scatter in the strength results was high enough that there is no apparent statistically significant correlation with any of the three controlled variables. Overall, strength increases

mildly with foil preform thickness, decreases weakly with beam power, and changes negligibly with secondary raster time. Figure 4.48 shows the relation between strength and foil thickness.

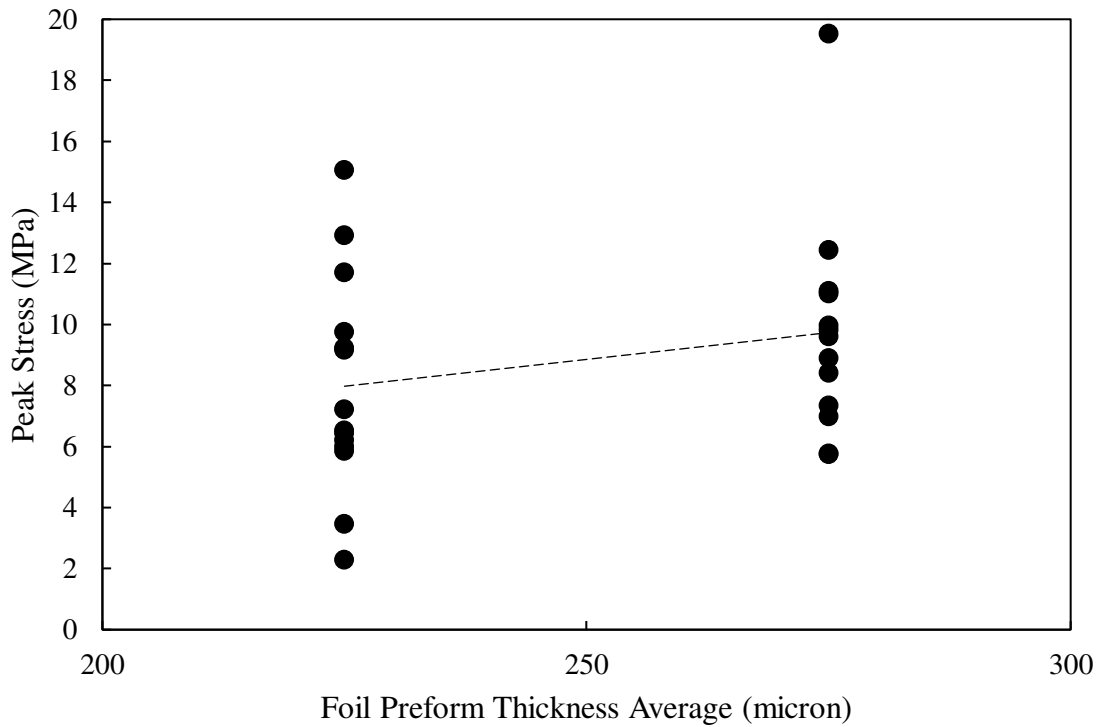


Figure 4.48 Strength as a function of foil preform thickness

The statistical p value for the correlation in Figure 4.48 is 0.23, indicating there is some statistical validity to the correlation despite the large data scatter. (However, it is customary to consider p values  $\leq 0.05$  as the cut-off value to invalidate a null hypothesis.) Conventionally, strength in a brazed joint increases as the gap width decreases, but this is not the case in Figure 4.48. Conventional brazements rely on gap sizes of the order of microns to tens of microns, where triaxiality predominates in the determination of final joint strength. Thinner gaps would result in higher strengths. In this research, the foils were about an order of magnitude thicker, with more filler metal. Even with the element losses to diffusion and overflow, more filler metal would remain in the joint. A high fraction filled within the gap leads to higher strength because more joint coverage is expected to support a greater load.

Strength will likely saturate and then begin to decrease with foil thickness. Once the foil is thick enough for the entire gap to remain filled after brazing, more filler metal will only lead to

a greater gap width and decrease the degree of triaxiality. The relation between strength and beam power is shown in Figure 4.49 and will be further discussed next.

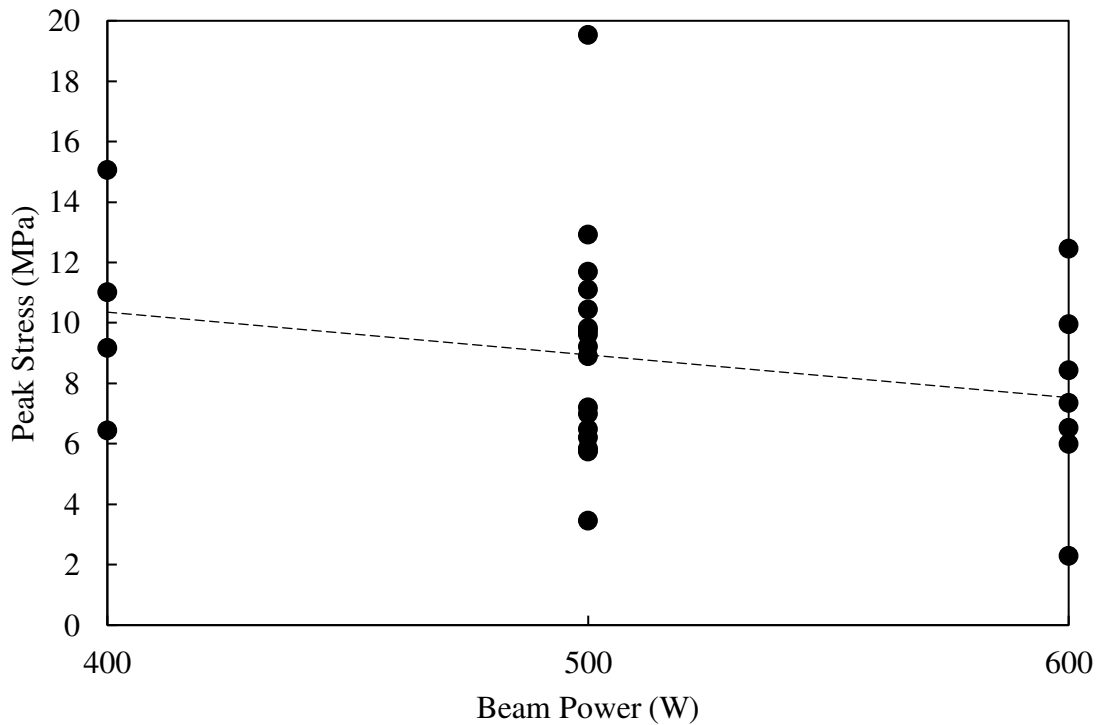


Figure 4.49 Strength as a function of beam power

The statistical p value for the correlation in Figure 4.49 is 0.29, indicating this correlation is weaker than the correlation between strength and foil thickness. For statistical purposes alone, the correlation shown in Figure 4.49 can be considered random. Nevertheless, the following speculation on strength and beam power can be made. Strength decreases with beam power for multiple reasons. A higher beam power leads to increased steady-state temperatures. Diffusivity increases with temperature, so higher temperatures would lead to greater loss of filler metal and strength decreases for the same reason as with the application of thinner foil preforms. Higher temperatures also lead to more surface damage. Increased surface damage introduces larger stress concentrators, decreasing the applied stress needed to reach the critical stress intensity for crack growth and failure. Further, higher temperatures lead to a weaker oxide dam, making it easier for overflows to occur. Even at 600 W laser power, temperatures were not high enough to exceed the melting point of any oxide compounds created except for iron-based oxide compounds. However, higher temperatures still weaken the oxide dam because of creep-like

effects. Figure 4.50 shows the graph of strength versus secondary raster time to facilitate concluding the discussion of strength dependency on controlled variables.

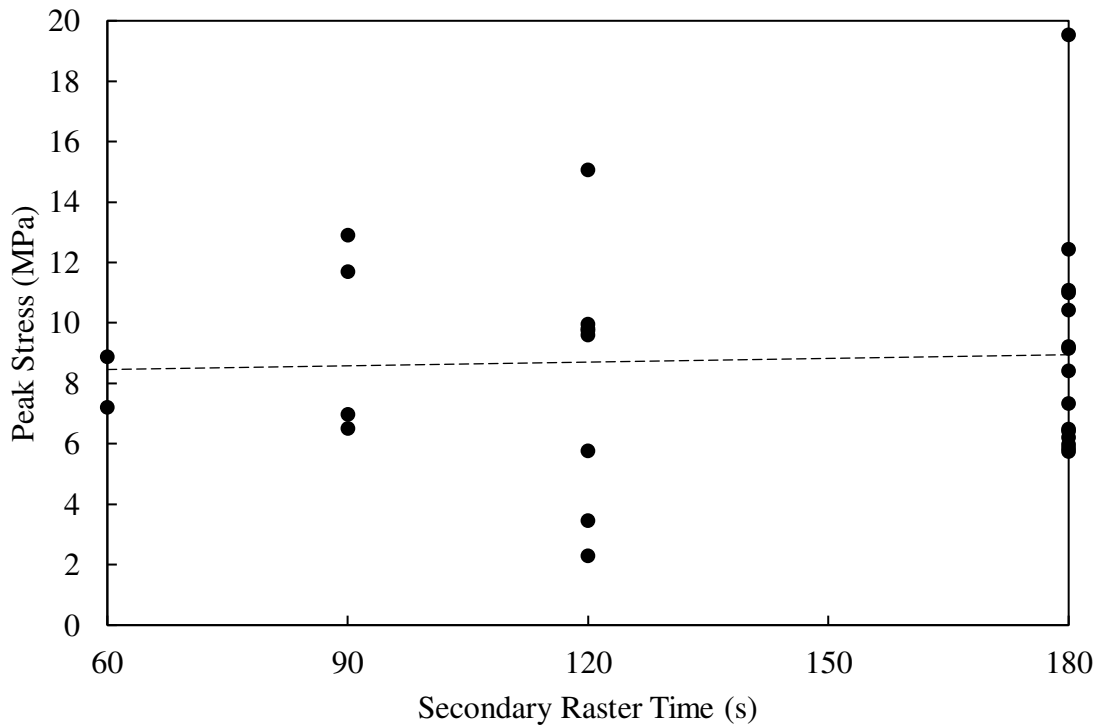


Figure 4.50 Strength as a function of secondary raster time

The statistical p value for the relation in Figure 4.50 is 0.79; there is not a statistically significant correlation between strength and secondary raster time. Secondary raster time has little to no effect on the strength of the resultant joint because the scatter in the system was too high. Additionally, the magnitude of effects such as foil preform thickness and beam power are both greater than secondary raster time. Diffusivity scales as a polynomial function with temperature for liquids, diffusion losses scale linearly with foil thickness, but diffusion rate scales sub-linearly with time. The percentile difference in total time at temperature is also reduced by the preheat raster, though temperatures reached in the joint are lower during the first raster.

Experimental data suggests strength improves by increasing foil thickness or the amount of filler metal added or decreasing beam power. The primary issue involves loss of filler metal to diffusion. The next greatest factor limiting the strength of the joints after filler metal loss is surface damage in the substrate. Both factors are affected by beam power, so this parameter

would be the first variable to optimize. Optimizing beam power is more of a challenge. There is a range between not melting the filler and reaching temperatures deleterious to strength.

Attempts to create lap joints with 200 W of power were performed but were unable to melt the filler metal completely. Higher laser power should be examined to identify the optimal processing window within which the filler melts but the free Si does not. If the free Si were to remain solid then diffusivity would be orders of magnitude lower, greatly reducing the amount of filler metal lost. Overflow losses could be reduced as well. The lowest melting point variant of iron oxide, FeO melts at 1377 °C when pure. Temperatures below this are still enough to melt the filler metal but could mitigate the weakening effect Fe from the free Si has on the oxide dam.

#### **4.6 Summary of Results**

The results discussed thus far provide four main conclusions about the behavior of the ternary Si-Al-Ti filler metal with the RB-SiC substrate.

- 1) Low to no damage laser processing of RB-SiC is feasible with the laser system at the CSM laboratory. Prior to this research, the laser system had only been used to welding and processing metals. Laser systems optimized for ceramic processing typically have mirrors to deflect the beam rather than moving the system mechanically, allowing much higher raster speeds. The methodology to heat and surface condition ceramics by establishing an operating ceiling for intensity and controlling the beam diameter created in this work facilitates processing many more ceramic materials besides RB-SiC.
- 2) Oxidation behavior strongly affects the behavior of the filler metal. The filler metal in this study was developed in vacuum furnace experimentation, so its behavior when exposed to atmosphere was unknown. Oxide development was expected but the effects on spreading were not.
- 3) Breakthrough in the oxide layer is possible. It is sensible that mechanical means such as Si solidification expansion could pierce the oxide layer. The influence of Fe on the integrity of the oxide layer was a serendipitous find.
- 4) Extensive diffusion takes place due to the continuous free Si network melting. Conventional brazing has most of the substrate remain solid, with the filler-substrate interface locally dissolving and/or melting in some cases. Completely melting one of the two phases comprising the substrate is unusual and led to a massive DAZ.

CHAPTER 5: SUMMARY AND CONCLUSIONS

The objective of this project was to determine if RB-SiC can be joined with a laser heat source given the Si-Al-Ti filler metal composition provided. Work was divided into four main steps: laser metrology, preheating and surface damage evaluation, wettability testing, and lap joint testing.

Laser metrology serves as the first step because all subsequent experimentation required knowing exact beam characteristics. Kapton™ film ablation results were consistent and had little scatter. Because the laser has low coupling efficiency with Kapton™, larger focal lengths did not form complete, well-defined holes. Data analysis thus required rejecting data not following a linear trend and extrapolating to find larger beam diameters.

The ability to preheat the substrate and process it without filler is the precursor to being able to heat the substrate with filler metal present. The key is to heat the substrate without creating cracks. Defocusing the beam to avoid sharp thermal gradients and rastering the beam are both effective methods. Insulating materials for fixturing to hold the substrate aids in temperature control and maximum achievable temperature since the highest possible temperature is controlled by the balance of beam power and heat loss rate. Higher beam powers lead to increased risk of cracking, so the target temperature must be carefully chosen with respect to the risk of cracking. Even when cracking is avoided, substrate damage still occurs through loss of free Si and oxidation over time.

Wettability testing is a first step in evaluating the viability of a brazing method. If a braze cannot wet to the substrate, then it will not join effectively. Wettability results initially seemed disappointing, as no combination of parameters led to contact angles below ninety degrees. Cross sectioning and chemical analysis through EDS revealed the actual problem. Despite implementing an atmosphere with low concentrations of oxygen, the elements in the filler metal have such a high affinity for oxygen that a surface oxide layer develops. The oxide layer is solid at all temperatures encountered and prevents the filler metal from spreading on the substrate. Contact angles are artificially high as a result.

High contact angles did not prove no wetting because the material on the surface is different than the actual filler metal. Cross sectioning revealed the interface between the filler metal and substrate is well wetted. Furthermore, the filler metal diffused into the substrate. In the case of a sample held at temperature for a prolonged time, the depth of diffusion was comparable to the thickness of the sample. There is wetting between the filler and substrate; contact angles are only high because atmospheric influence affects spreading.

Lap joints represent how a joint might perform in the field. Shear strength for the joints made is not particularly high. The main cause is loss of filler metal in the gap reducing load bearing area while creating stress concentrators. A lack of fillet formation due to severe oxidation when the beam impinges on filler metal affects strength as well. Filler metal is lost through diffusion and the creation of overflow features. High diffusion flux results from the free Si in the substrate melting. Overflows are normally contained by the creation of the same oxide layer seen in wettability testing, but the layer may be broken through. Breakthrough mechanisms are Si expansion during solidification after preheating and weakening of the layer by Fe exuded from the free Si. Even though the gap is not entirely filled, failure is still seen outside the joint. Surface damage from loss of free Si is partially responsible for failure in the substrate. Samples failing within the joint reveal oxidation is also occurring within the gap. Attempts were made to reduce oxidation by adding hydrogen gas to the atmosphere but efforts were not successful.

Joining of RB-SiC with a laser heat source is possible but does not produce excellent joints. The filler metal performs the action required of an active metal braze, namely creating a reaction layer. Laser heating of RB-SiC works well, and temperature may even be controlled to different values by region through the design of raster patterns. Surface damage still occurs from laser heating but is a result of the temperatures reached globally across the sample rather than thermal gradients formed as a direct result of the beam.

Strength may be improved via several methods. The simplest would be to control temperature so the free Si does not melt. Preventing overflows through stop offs along the sides of the joint would be the next step in increasing strength. Increasing the amount of filler metal added could also serve to prevent voids in the gap but does nothing to prevent filler metal contamination of the substrate by diffusion.

Chapter 6  
CHAPTER 6: FUTURE WORK

Joining ceramics inside a furnace is difficult. Adding a laser as a heat source further complicates the joining process. Unique challenges arise from the moment the beam impinges on the substrate surface. Brazing in an atmosphere instead of a vacuum chamber also creates difficulties. Research routes to improve the laser brazing process are discussed in this section.

- 1) Lower laser powers, potentially for longer times may generate successful results. Lower laser powers directly lead to lower temperatures, which will prevent the free Si from melting and reduce diffusion rates, allowing more filler metal to remain in the gap. Free Si remaining solid also lowers the diffusion rate of Fe into the filler metal, which could reduce the amount of overflow losses. Experimental programs with lower laser powers should be developed and conducted to verify the premises stated earlier.
- 2) Make joints with a sintered SiC substrate instead of RB-SiC. Sintered SiC has a lower diffusivity than RB-SiC and superior high temperature performance. If sintered SiC were the substrate material instead of RB-SiC, brazes could be made faster through higher temperatures. Surface damage would also be lessened since surface damage in RB-SiC is almost entirely from loss of the free Si. Experimental joining with sintered SiC should be performed to verify the feasibility of sintered SiC for engineering components.
- 3) Surface texturing to increase wettability was attempted but did not decrease contact angles. The cause is likely increased oxidation of the RB-SiC surface since the ablation to create surface texture was performed in open air. Ablating under an Ar atmosphere to prevent excessive oxidation would resolve this issue and isolate the effect of texture itself. This enables the creation of an experimental matrix varying the depth of texturing and texture patterning. Texture depth is a direct result of the number and energy of pulses during ablation. Example parameters of interest within texture patterning include the distance between ablation spots and whether the spots are arranged in a square, rectangular, hexagonal, or random grid.
- 4) Deliberately melt the free Si to create joints with narrow gaps. Liquation of free Si could be advantageous by creating an extremely thin foil of filler materials and brazing above the melting point of silicon for a short time. Brazing with only the secondary raster

pattern directly over the faying surfaces for a short time could allow the free Si and filler metal to melt for a short period of time and form a joint. Diffusion lengths needed for joining on the scale of tens of microns should be targeted. The greatest potential issue is by abandoning the preheat raster, thermal gradients through the thickness of the sample would be created so the side facing the laser is hotter than the underside. Diffusion lengths would be greater in the upper side as a result, resulting in asymmetrical joint properties.

- 5) Braze with a laser heat source in vacuum to examine the difference in overflow behavior. A joint made in vacuum should see increased overflow volume. This experiment does not require the use of a laser heat source. However, it is important to note that heating and cooling rates in vacuum systems are very different from those representative of laser processing.
- 6) Oxide formation prevented the wettability tests from showing the true contact angle of the system. An apparatus with an induction coil and active cooling system in a vacuum chamber could replicate the heating and cooling rates seen during laser processing. Alternatively, a laser could heat the substrate instead of an induction coil; an induction coil is chosen because closed-loop temperature control is easier with induction. Active cooling is needed because cooling in a vacuum is largely restricted to radiative heat transfer. Heat loss at the steady-state temperature is mostly radiative, but active cooling is needed to replicate heat loss rates below these temperatures.
- 7) A hydrogen bearing atmosphere was used in three trials, but the concentration of hydrogen was too low to prevent oxidation. Conduct a series of experiments with varying hydrogen concentrations in the atmosphere with the goal of finding an operating window where oxidation is prevented but hydride compounds are not formed. Further experimentation with varying beam powers as well could determine the effect of temperature on the processing window of hydrogen concentration.
- 8) Experiments with only secondary rasters should be conducted. Avoiding the preheat raster leads to thermal gradients causing the laser-facing side of the sample to be warmer. However, no preheat raster also means the beam never impinges on large regions of the sample. Additional insulation could be placed to reduce the heat loss rate. In turn, less beam power is needed to reach the same powers which reduces surface damage. Overall

efficiency could also be improved with this methodology because less volume of material is heated. The unanswered question is if the brazed joint itself is affected by not preheating.

- 9) Preheat with lower beam power to prevent the filler melting to minimize protrusions and overflow, and oxide skin breakthrough.
- 10) Stop-offs are used in conventional brazing to control the spreading of molten filler metal on a brazed joint. Identify an adequate material as stop-off for RB-SiC. The ideal stop-off material would not interact with the filler metal. Examine the feasibility of placing stop-offs to guide molten filler to form fillets only but prevent overflow formation.

## REFERENCES

- [1] “A Global Leader in Technical Ceramics,” CoorsTek. [Online]. Available: <https://www.coorstek.com/>. [Accessed: 06-May-2019].
- [2] N. S. Jacobson, “Corrosion of Silicon-Based Ceramics in Combustion Environments,” *Journal of the American Ceramic Society*, vol. 76, no. 1, pp. 3–28, 1993.
- [3] Zhang, Z. and Modest, M. (1998). Temperature-Dependent Absorptances of Ceramics for Nd:YAG and CO<sub>2</sub> Laser Processing Applications. *Journal of Heat Transfer*, 120(2), p.322.
- [4] Ness, J. and Page, T. (1986). Microstructural evolution in reaction-bonded silicon carbide. *Journal of Material Science*, 21(4), pp.1377-1397.
- [5] G. Brezeanu, “Silicon carbide (SiC): a short history. an analytical approach for SiC power device design,” *CAS 2005 Proceedings. 2005 International Semiconductor Conference, 2005*.
- [6] J. Casady and R. Johnson, “Status of silicon carbide (SiC) as a wide-bandgap semiconductor for high-temperature applications: A review,” *Solid-State Electronics*, vol. 39, no. 10, pp. 1409–1422, 1996.
- [7] M. Flinders, D. Ray, A. Anderson, and R. A. Cutler, “High-Toughness Silicon Carbide as Armor,” *Journal of the American Ceramic Society*, vol. 88, no. 8, pp. 2217–2226, 2005.
- [8] R. Verrall, M. Vljajic, and V. Krstic, “Silicon carbide as an inert-matrix for a thermal reactor fuel,” *Journal of Nuclear Materials*, vol. 274, no. 1-2, pp. 54–60, 1999.
- [9] H. Du, C. Song, and S. Li, “Study on Surface Roughness of Modified Silicon Carbide Mirrors polished by Magnetorheological Finishing,” *IOP Conference Series: Materials Science and Engineering*, vol. 301, p. 012164, 2018.
- [10] S. M. Wiederhorn, D. E. Roberts, T.-J. Chuang, and L. Chuck, “Damage-Enhanced Creep in a Siliconized Silicon Carbide: Phenomenology,” *Journal of the American Ceramic Society*, vol. 71, no. 7, pp. 602–608, 1988.
- [11] C. Carter, R. Davis, and J. Bentley, “Kinetics and Mechanisms of High-Temperature Creep in Silicon Carbide: I, Reaction-Bonded,” *Journal of the American Ceramic Society*, vol. 67, no. 6, pp. 409–417, 1984.
- [12] T. M. Pollock and S. Tin, “Nickel-Based Superalloys for Advanced Turbine Engines: Chemistry, Microstructure and Properties,” *Journal of Propulsion and Power*, vol. 22, no. 2, pp. 361–374, 2006.

- [13] S. M. Wiederhorn, L. Chuck, E. R. Fuller, and N. J. Tighe, "Creep Rupture of Siliconized Silicon Carbide," *Tailoring Multiphase and Composite Ceramics*, pp. 755–773, 1986.
- [14] B. Fields and S. Wiederhorn, "Variation of creep damage with depth below the surface in a siliconized silicon carbide," *Scripta Metallurgica et Materialia*, vol. 29, no. 6, pp. 777–782, 1993.
- [15] "Progress in silicon based non-oxide structural ceramics," *Metal Powder Report*, vol. 52, no. 10, p. 38, 1997.
- [16] H.-W. Kim, H.-E. Kim, H. Song, and J. Ha, "Effect of Oxidation on the Room-Temperature Flexural Strength of Reaction-Bonded Silicon Carbides," *Journal of the American Ceramic Society*, vol. 82, no. 6, pp. 1601–1604, 2004.
- [17] T. J. Moore, "Feasibility Study of the Welding of SiC," *Journal of the American Ceramic Society*, vol. 68, no. 6, 1985.
- [18] M.M. Schwartz, Introduction to Brazing and Soldering, *Welding, Brazing, and Soldering*, Vol 6, *ASM Handbook*, ASM International, 1993, p 109–113
- [19] W.-K. Rhim, K. Ohsaka, P.-F. Paradis, and R. E. Spjut, "Noncontact technique for measuring surface tension and viscosity of molten materials using high temperature electrostatic levitation," *Review of Scientific Instruments*, vol. 70, no. 6, pp. 2796–2801, 1999.
- [20] R. O'Hayre, *Materials Kinetics Fundamentals*. New York: John Wiley & Sons Inc, 2015.
- [21] V. K. Kumikov and K. B. Khokonov, "On the measurement of surface free energy and surface tension of solid metals," *Journal of Applied Physics*, vol. 54, no. 3, pp. 1346–1350, 1983.
- [22] W.-K. Rhim, K. Ohsaka, P.-F. Paradis, and R. E. Spjut, "Noncontact technique for measuring surface tension and viscosity of molten materials using high temperature electrostatic levitation," *Review of Scientific Instruments*, vol. 70, no. 6, pp. 2796–2801, 1999.
- [23] T. W. Richards and E. K. Carver, "A Critical Study Of The Capillary Rise Method Of Determining Surface Tension, With Data For Water, Benzene, Toluene, Chloroform, Carbon Tetrachloride, Ether And Dimethyl Aniline. [Second Paper.]1," *Journal of the American Chemical Society*, vol. 43, no. 4, pp. 827–847, 1921.
- [24] D. Briggs, D. Rance, C. Kendall, and A. Blythe, "Surface modification of poly(ethylene terephthalate) by electrical discharge treatment," *Polymer*, vol. 21, no. 8, pp. 895–900, 1980.
- [25] W. L. Vaughn and H. G. Maahs, "ChemInform Abstract: Active-to-Passive Transition in the Oxidation of Silicon Carbide and Silicon Nitride in Air," *ChemInform*, vol. 21, no. 36, 1990.

- [26] J. H. G. Mattheij, "Role of brazing in repair of superalloy components – advantages and limitations," *Materials Science and Technology*, vol. 1, no. 8, pp. 608–612, 1985.
- [27] J. H. G. Mattheij, "Role of brazing in repair of superalloy components – advantages and limitations," *Materials Science and Technology*, vol. 1, no. 8, pp. 608–612, 1985.
- [28] R. Coltters, "Thermodynamics of binary metallic carbides: A review," *Materials Science and Engineering*, vol. 76, pp. 1–50, 1985.
- [29] T. Yamazaki and A. Suzumura, "Reaction products at brazed interface between Ag–Cu–V filler metal and diamond (111)," *Journal of Materials Science*, vol. 41, no. 19, pp. 6409–6416, 2006.
- [30] Relationship between X-ray diffraction and unidirectional solidification at interface between diamond and brazing filler metal, T. Yamazaki, A. Suzumura, 2000
- [31] P. Prakash, T. Mohandas, and P. D. Raju, "Microstructural characterization of SiC ceramic and SiC–metal active metal brazed joints," *Scripta Materialia*, vol. 52, no. 11, pp. 1169–1173, 2005.
- [32] H.-P. Xiong, W. Mao, Y.-H. Xie, W.-L. Guo, X.-H. Li, and Y.-Y. Cheng, "Brazing of SiC to a wrought nickel-based superalloy using CoFeNi(Si, B)CrTi filler metal," *Materials Letters*, vol. 61, no. 25, pp. 4662–4665, 2007.
- [33] O. M. Akselsen, "Advances in brazing of ceramics," *Journal of Materials Science*, vol. 27, no. 8, pp. 1989–2000, 1992.
- [34] P. Nikolopoulos, S. A. P. Los, G. N. Angelopoulos, A. Naoumidis, and H. Grübmeier, "Wettability and interfacial energies in SiC-liquid metal systems," *Journal of Materials Science*, vol. 27, no. 1, pp. 139–145, 1992.
- [35] G. Liu, M. Muolo, F. Valenza, and A. Passerone, "Survey on wetting of SiC by molten metals," *Ceramics International*, vol. 36, no. 4, pp. 1177–1188, 2010.
- [36] Y. Li, L. Zhang, and Z. Benouahmane, "Effect of Oxidation on Wetting Behavior between Silicon and Silicon Carbide," *7th International Symposium on High-Temperature Metallurgical Processing*, pp. 237–242, 2016.
- [37] E. Saiz, R. M. Cannon, and A. P. Tomsia, "High-Temperature Wetting and the Work of Adhesion in Metal/Oxide Systems," *Annual Review of Materials Research*, vol. 38, no. 1, pp. 197–226, 2008.
- [38] K. Nogi, "The role of wettability in metal–ceramic joining," *Scripta Materialia*, vol. 62, no. 12, pp. 945–948, 2010.
- [39] W. Lippmann, J. Knorr, R. Wolf, R. Rasper, H. Exner, A.-M. Reinecke, M. Nieher, and R. Schreiber, "Laser joining of silicon carbide—a new technology for ultra-high

- temperature resistant joints,” *Nuclear Engineering and Design*, vol. 231, no. 2, pp. 151–161, 2004.
- [40] C. Hille, W. Lippmann, and A. Hurtado, “Electrically conductive ceramics and new joining technology for applications in HTR engineering,” *Nuclear Engineering and Design*, vol. 251, pp. 222–229, 2012.
- [41] M. Herrmann, W. Lippmann, and A. Hurtado, “High-temperature stability of laser-joined silicon carbide components,” *Journal of Nuclear Materials*, vol. 443, no. 1-3, pp. 458–466, 2013.
- [41] P. Meisel, M. Jobst, W. Lippmann, and A. Hurtado, “Design and manufacture of ceramic heat pipes for high temperature applications,” *Applied Thermal Engineering*, vol. 75, pp. 692–699, 2015.
- [42] M. Herrmann, P. Meisel, W. Lippmann, and A. Hurtado, “Joining technology—A challenge for the use of SiC components in HTRs,” *Nuclear Engineering and Design*, vol. 306, pp. 170–176, 2016.
- [43] C. Rado, S. Kalogeropoulou, and N. Eustathopoulos, “Wetting and bonding of Ni–Si alloys on silicon carbide,” *Acta Materialia*, vol. 47, no. 2, pp. 461–473, 1999.
- [44] K. Nagatsuka, Y. Sechi, N. Ma, and K. Nakata, “Simulation of cracking phenomena during laser brazing of ceramics and cemented carbide,” *Science and Technology of Welding and Joining*, vol. 19, no. 8, pp. 682–688, 2014.
- [45] J. Zheng, Ö. Ünal, and M. Akinc, “Green State Joining of Silicon Carbide Using Polycarbosilane,” *Journal of the American Ceramic Society*, vol. 83, no. 7, pp. 1687–1692, 2004.
- [46] J. Zheng and M. Akinc, “Green State Joining of SiC without Applied Pressure,” *Journal of the American Ceramic Society*, vol. 84, no. 11, pp. 2479–2483, 2001.
- [47] C. A. Lewinsohn, R. H. Jones, P. Colombo, and B. Riccardi, “Silicon carbide-based materials for joining silicon carbide composites for fusion energy applications,” *Journal of Nuclear Materials*, vol. 307-311, pp. 1232–1236, 2002.
- [48] P. Colombo, V. Sglavo, E. Pippel, and P. Colombo, “Joining of reaction-bonded silicon carbide using a preceramic polymer,” *Journal of Materials Science*, vol. 33, no. 9, pp. 2405–2412, 1998.
- [49] T. Iseki, K. Arakawa, and H. Suzuki, “Joining of dense silicon carbide by hot-pressing,” *Journal of Materials Science*, vol. 15, no. 4, pp. 1049–1050, 1980.
- [50] O. M. Akselsen, “Diffusion bonding of ceramics,” *Journal of Materials Science*, vol. 27, no. 3, pp. 569–579, 1992.
- [51] W. M. Steen and J. Mazumder, *Laser material processing*. London: Springer, 2010.

- [52] W. W. Duley, *Laser welding*. New York: Wiley, 1999.
- [53] J. M. Khosrofian and B. A. Garetz, "Measurement of a Gaussian laser beam diameter through the direct inversion of knife-edge data," *Applied Optics*, vol. 22, no. 21, p. 3406, 1983.
- [54] Fuerschbach, P., Norris, J., Dykhuizen, R. and Mahoney, A. (2004). Development and Evaluation of an In-Site Beam Measurement for Spot Welding Lasers. *Welding Journal*, pp.154-159.
- [55] M. Kafkalidis and M. Thouless, "The effects of geometry and material properties on the fracture of single lap-shear joints," *International Journal of Solids and Structures*, vol. 39, no. 17, pp. 4367–4383, 2002.
- [56] A. N. Samant and N. B. Dahotre, "Laser machining of structural ceramics—A review," *Journal of the European Ceramic Society*, vol. 29, no. 6, pp. 969–993, 2009.
- [57] I. Südmeyer, T. Hettesheimer, and M. Rohde, "On the shear strength of laser brazed SiC–steel joints: Effects of braze metal fillers and surface patterning," *Ceramics International*, vol. 36, no. 3, pp. 1083–1090, 2010.
- [58] B. N. Chichkov, C. Momma, S. Nolte, F. Alvensleben, and A. Tünnermann, "Femtosecond, picosecond and nanosecond laser ablation of solids," *Applied Physics A Materials Science & Processing*, vol. 63, no. 2, pp. 109–115, 1996.
- [59] T. J. Perham, L. C. Jonghe, and W. J. Moberlychan, "Joining of Silicon Carbide with a Cordierite Glass-Ceramic," *Journal of the American Ceramic Society*, vol. 82, no. 2, pp. 297–305, 2004.
- [60] A. Sadek, E. D. Herderick, K. E. Cooper, and N. D. Ames, "Method for joining silicon carbide components to one another."s
- [61] "Ellingham Diagrams," *MIT*. [Online]. Available: [http://web.mit.edu/2.813/www/readings/Ellingham\\_diagrams.pdf](http://web.mit.edu/2.813/www/readings/Ellingham_diagrams.pdf)
- [62] Y. Sato, T. Nishizuka, K. Hara, T. Yamamura, and Y. Waseda, "Density Measurement of Molten Silicon by a Pycnometric Method," *International Journal of Thermophysics*, vol. 21, no. 6, pp. 1463–1471, 2000.
- [63] C. Hawk, Kottilingam, "Effect of Processing Parameters on the Microstructure and Mechanical Properties of Wide-Gap Braze Repairs on Nickel Superalloy René 108," *Welding in the World*, Vol.61, Iss. 2, pp. 391-404, 2017.
- [64] D. J. Fisher, *Diffusion in silicon: 10 years of research*. Zuerich-Uetikon: Scitec, 1998.
- [65] C. Natalie, D. L. Olson, and M. Blander, "Physical and Chemical Behavior of Welding Fluxes," *Annual Review of Materials Research*, vol. 16, no. 1, pp. 389–413, 1986.